H. BALL

RECOVERY TUBE TRADE-OFF STUDY FOR

REENTRY GROUND TEST FACILITY

ACUREX CORPORATION/AEROTHERM DIVISION
485 CLYDE AVENUE
MOUNTAIN VIEW, CALIFORNIA 94042

September 1976

Final Report for Period 30 June 1975 - 1 May 1976

TECHNICAL REPORTS
FILE COPY

Approved for public release; distribution unlimited

Prepared for

DIRECTORATE OF TECHNOLOGY (DYX)
ARNOLD ENGINEERING DEVELOPMENT CENTER
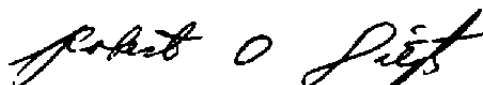ARNOLD AIR FORCE STATION, TENNESSEE 37389

APPROVAL STATEMENT

This technical report has been reviewed and is approved for publication.

FOR THE COMMANDER

ALBERT E. DIETZ
Requirements Planning
    Division
Directorate of Technology

ROBERT O. DIETZ
Director of Technology

REPORT DOCUMENTATION PAGE		READ INSTRUCTIONS BEFORE COMPLETING FORM
1 REPORT NUMBER AEDC-TR-76-115	2 GOVT ACCESSION NO.	3 RECIPIENT'S CATALOG NUMBER
4 TITLE (and Subtitle) RECOVERY TUBE TRADE-OFF STUDY FOR REENTRY GOUND TEST FACILITY		5 TYPE OF REPORT & PERIOD COVERED Final Report - 30 June 1975 - 1 May 1976
		6 PERFORMING ORG. REPORT NUMBER Aerotherm TR-76-196
7 AUTHOR(s) T. C. Derbidge and T. J. Dahm		8 CONTRACT OR GRANT NUMBER(s) F40600-76-C-0001
9 PERFORMING ORGANIZATION NAME AND ADDRESS Acurex Corporation/Aerotherm Division 485 Clyde Avenue Mountain View, California 94042		10 PROGRAM ELEMENT, PROJECT, TASK AREA & WORK UNIT NUMBERS Program Element 65807F
11 CONTROLLING OFFICE NAME AND ADDRESS Arnold Engineering Development Center(DYFS) Air Force Systems Command Arnold Air Force Station, Tennessee 37389		12 REPORT DATE September 1976
		13 NUMBER OF PAGES 155
14 MONITORING AGENCY NAME & ADDRESS(if different from Controlling Office)		15 SECURITY CLASS. (of this report) UNCLASSIFIED
		15a DECLASSIFICATION·DOWNGRADING SCHEDULE N/A

16 DISTRIBUTION STATEMENT (of this Report)

Approved for public release; distribution unlimited.

17 DISTRIBUTION STATEMENT (of the abstract entered in Block 20, if different from Report)

18 SUPPLEMENTARY NOTES

Available in DDC

19 KEY WORDS (Continue on reverse side if necessary and identify by block number)

recovery	reentry vehicles
tubes	tracks (aerodynamics)
test facilities	mathematical analysis
simulation	costs

20 ABSTRACT (Continue on reverse side if necessary and identify by block number)

An analytical study was performed to optimize the design of a projectile recovery tube for a large scale track guided projectile range for testing reentry vehicles. The projectile is recovered in this device by guiding it with a track into a compartmented tube where it compresses gas and is thus decelerated by pressure forces. The recovery tube design was optimized to produce minimum projectile damage and system cost.

DD FORM 1473 EDITION OF 1 NOV 65 IS OBSOLETE
1 JAN 73

20.   ABSTRACT (Continued)

Projectile damage due to ablation, structural loading, and material
property changes where analytically predicted for a matrix of
recovery tube design options.   Model damage was found to be small
in all cases.

Recovery tube costs were also estimated for a matrix of design
options.   The design option which gave the minimum cost, consistent
with a large scale range, had three helium filled compartments
with a bore of about 8 inches, and a length of about 1000 feet.
The estimated cost for this system was about $900,000.

AFSC
Arnold AFS Tenn

PREFACE

This document is the final report for AEDC Contract F40600-76-C-0001. This work was performed by the Aerotherm Division of Acurex Corporation, Mountain View, California for the Arnold Engineering Development Center, Directorate of Technology. Mr. Al Dietz, Requirements Planning Division, Directorate of Technology, was the AEDC Technical Representative. The Aerotherm Project Manager was Mr. Charles Powars. This report covers work conducted during the period July 1975 through March 1976. The Program Element number was 65807F, and the manuscript was submitted for publication on August 27, 1976.

Considerable technical information and guidance was provided to this study by ARO, Inc. personnel at AEDC including Mssrs. Glen Norfleet, John Cable, Jack DeWitt, and Jim Hicks. Mr. Robert McCormack of NASA-Ames supported this study by efforts to implement numerical analyses of the projectile near flow field. At Aerotherm, numerous individuals contributed to this study including Dr. Larry Cooper, Mr. Kelly Lee, and Dr. Lynn Cohen in the area of tube gas dynamics, Dr. A. Balakrishnan in the area of gas radiation, Dr. Larry Waterland and Mr. Michael Abbett in the area of model near field flows and convective heat transfer, Dr. Donald Brink in the area of model heat conduction and ablation, Dr. Yuen Lee in the area of model thermal stress, and Mr. Ron McClellan and Mr. Tom Wong in the area of system preliminary design and cost analysis.

The reproducibles used in the reproduction of this report were supplied by the authors, T. C. Derbidge and T. J. Dahm.

TABLE OF CONTENTS

TABLE OF CONTENTS (Concluded)

LIST OF ILLUSTRATIONS

LIST OF ILLUSTRATIONS (Continued)

LIST OF ILLUSTRATIONS (Concluded)

LIST OF TABLES

SECTION 1

INTRODUCTION

The difficulties associated with conducting effective ground tests of strategic reentry vehicles are well recognized by the reentry community. Current ground test techniques involve significant compromises in either simulation quality (of the flight environment, model size, or test time) or data quality or both. One promising concept which has recently been advanced for reentry vehicle (RV) ground testing is the guided track projectile range (References 1, 2, and 3). The principal elements of a conceptual guided track range are sketched in Figure 1-1.

The guided track projectile range differs from a conventional ballistics range in that the projectile or model is guided by a track. Studies have shown (References 1 and 2) that the frictional drag associated with model guidance along the track is small relative to the aerodynamic drag acting on the model at range pressures of interest for RV testing. Other elements of a guided track range which are sketched in Figure 1-1 are the launcher, a model preheater and perhaps preconditioning section for reducing the model temperature transient during flight, the test range which includes the tracks and perhaps partitions to divide the range into regions of different static conditions, and a deceleration section to enable recovery of the model.

The potential advantages of a large scale guided track range for RV testing can best be illustrated through comparison with testing in a conventional ballistics range. The conventional ballistics range has proven to be moderately successful for testing the ablation performance of RV thermal protection materials (cf., Reference 4). The principal disadvantages of the conventional ballistics range for this type of testing are:

a. The model cannot be recovered for post-test examination

b. It is often difficult to obtain high quality photographs of the model in flight near the end of the range (even with the very sophisticated equipment currently being used) due to model dispersion relative to the focal plane
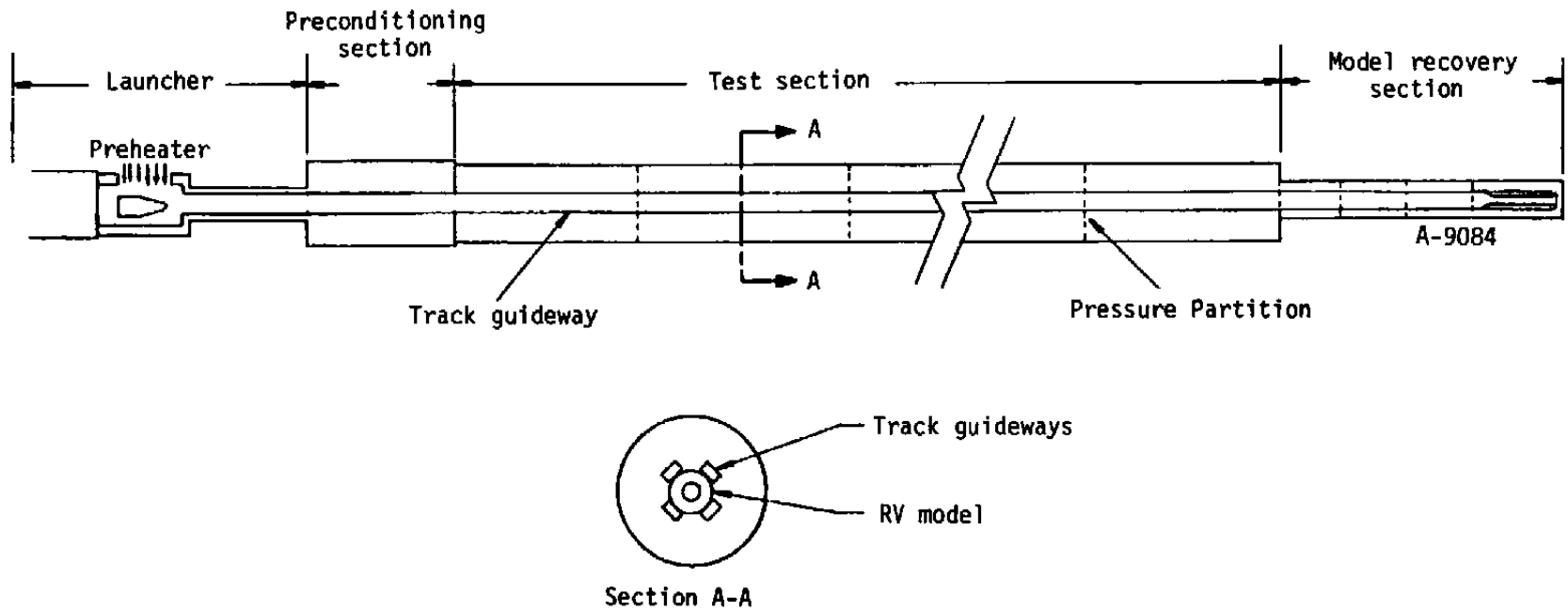
Figure 1-1. Sketch of conceptual guided track projectile range for reentry vehicle testing.

c. Test times are so short (about 0.07 seconds) that it is difficult to precisely measure material ablation rates and it is impossible to obtain data relative to overall nosetip shape-change

d. Test models are typically much smaller than the RV components of interest.

A large scale guided track range has the potential for overcoming all of the above problems. The "track" would serve to guide the model precisely along a straight trajectory, and this would enable accurate photographic data to be obtained at all locations along the range. The track could also serve to guide the model into a compression tube which would decelerate the model and enable model recovery. Model recovery capability has already been demonstrated in a subscale guided track range (Reference 2). The operation principle of the recovery tube is discussed in more detail subsequently.

Test times in a ballistics range are of course limited by the range length. However, the lengths of the two ballistic ranges currently used for RV testing (AEDC Range G and the NSWC Hyperballistics Range) are 1000 ft, and lengths much longer than this are impractical due to model dispersion and deceleration. A large guided track range would not be limited in length by these factors since the track would eliminate model dispersion and model deceleration rates would be lower (because the model deceleration depends on the ballistic coefficient, β, and β scales with the model size). Additionally, the "effective" test time in a guided track range could be increased substantially by recovering and relaunching the model. Analytical studies documented in Reference 3 showed that, in principle, an entire reentry trajectory could be simulated by repetitive model recovery and relaunch at velocity and range conditions adjusted to correspond to the next increment of the reentry trajectory.

While the guided track projectile range concept is entirely feasible in principle and successful operation has been demonstrated in a small scale range, AEDC studies have identified certain technology issues which should be addressed relative to a very large scale guided track RV test range. These technology issues include:

1. The launcher

2. The preheater

3. Model/track interactions

4. Model recovery

This study was directed toward the model recovery issue.

Model recovery is to be accomplished by guiding the model into a recovery tube where it compresses the gas in front of it, and this serves to decelerate the model. The model deceleration rate (and hence recovery tube length) may be controlled by the static pressure of the gas in the tube, and the gas type. In order to tailor the model deceleration rate, the gas static pressure in the tube may be varied through the use of fast acting valves. These valves would serve to compartmentalize the tube into regions of various pressures, but would open to allow passage of the model and shock compressed gas. As the model velocity decreases to low values, it becomes less practical to continue deceleration through gas compression and more practical to stop the model by friction. Thus, terminal model deceleration would be accomplished in a friction section.

The objective of this study was to analytically optimize the appropriate parameters of the recovery tube design based on:

1. Minimum model damage

2. Minimum recovery system cost

There are many options relative to the configuration and operation of the recovery tube. The principal factors affecting the recovery tube design are model damage and system cost. Indeed, there existed uncertainties regarding the basic feasibility of recovering a heavy (i.e., 10's of pounds) model from a high velocity (i.e.,15 – 20 kfps) without subjecting it to unacceptably severe damage. Model damage during recovery was expected to be due to three principal causes:

Ablation —

Due to the high pressures, gas enthalpies, and convective heating rates acting on the model during recovery

Structural Loading —

Due to deceleration forces, pressure forces, and thermal stresses acting on the model during recovery

Material Property Changes —

Due to the high temperature soak experienced by the model during recovery and during the "cool-down" period following recovery

Recovery system costs are obviously dependent on things like the tube length and wall thickness required which in turn depend on the model deceleration rate and pressure.

There are certain practical constraints placed on the recovery system configuration by model launch requirements, ballistic coefficient scaling, and recovery dynamics. These are established in Section 2, System Sizing Considerations. There are also some basic alternatives relative to the recovery tube operating principles, and these are reviewed in Section 3, General Features of Recovery Tubes. A major part of this study was directed at predicting the level of model damage during recovery. The analytical techniques used to compute the model damage are discussed in Section 4 and the damage calculation results for a matrix of relevent recovery conditions are presented in Section 5. The recovery system cost analysis and cost optimization results are presented in Section 6. Based on the results of this study, conclusions and recommendations are summarized in Section 7.

SECTION 2
SYSTEM SIZING CONSIDERATIONS

The objective of this study is to optimize recovery tube design parameters. Before any such optimization can proceed, the first step is to determine practical constraints imposed on recovery tube parameters by projectile launch, range, and recovery considerations. These considerations will serve as a guide in determining key parameters and in selecting a reasonable range of each. Projectile launch, range, flight and recovery considerations are covered in the following subsections.

2.1 LAUNCH CONSIDERATIONS

The description of launch considerations which follow assumes a gun launcher. While it is not certain that a large scale projectile range would use a gun launcher (a rocket launcher is also under consideration), it does represent a fairly well proven and conservative approach.

The relations governing the operation of such a device are primarily dynamics, kinematics, and launcher design constraints. The dynamic relation which follows from a Newtonian force balance on the projectile is:

$$P_L = \frac{F}{A_b} = \left(\frac{M_p}{A_b}\right) a_L \qquad (2\text{-}1)$$

where

P_L = launch pressure

A_b = projectile base area

M_p = projectile mass

a_L = launch acceleration rate

Similarly, the kinematic relation assuming approximately constant acceleration in the launcher is:

$$L = \frac{V_L^2}{2a_L} \qquad (2\text{-}2)$$

where

L = length of launcher

V_L = launch velocity

The final launch relation is imposed by the requirement that optimal launcher design requires that the ratio of length to diameter be held approximately constant

$$\frac{L}{D} = \text{constant} = C \qquad (2\text{-}3)$$

This relation comes from both empirical observation of operating gun systems and approximate theoretical considerations.

Combining Equations (2-1) through (2-3) and solving for the projectile mass per unit base area (M_p/A_b) yields

$$\left(\frac{M_p}{A_b}\right) = \left(\frac{2P_L C}{V_L^2}\right) D \qquad (2\text{-}4)$$

Observing the quantities in the parentheses on the right side of Equation (2-4), the following can be noted:

- Maximum launch pressure (P_L) is dictated by launcher and projectile material strength limits

- Maximum launch velocity (V_L) is given by the requirement to simulate reentry flight

Applying these observations to Equation (2-4) it is apparent that projectile mass per unit area is proportional to the launcher diameter

$$\left(\frac{M_p}{A_b}\right) \sim D \qquad (2\text{-}5)$$

The proportionality constant for Relation (2-5) was estimated using the current AEDC Range G nominal operation condition. A plot of the resultant variation of M_p/A_b with D is shown in Figure 2-1.

2.2 RANGE FLIGHT CONSIDERATIONS

The most important consideration for range flight is the ballistic coefficient. If the ballistic coefficient is significantly less than the desired value, the projectile velocity in the range will quickly drop below flight values.
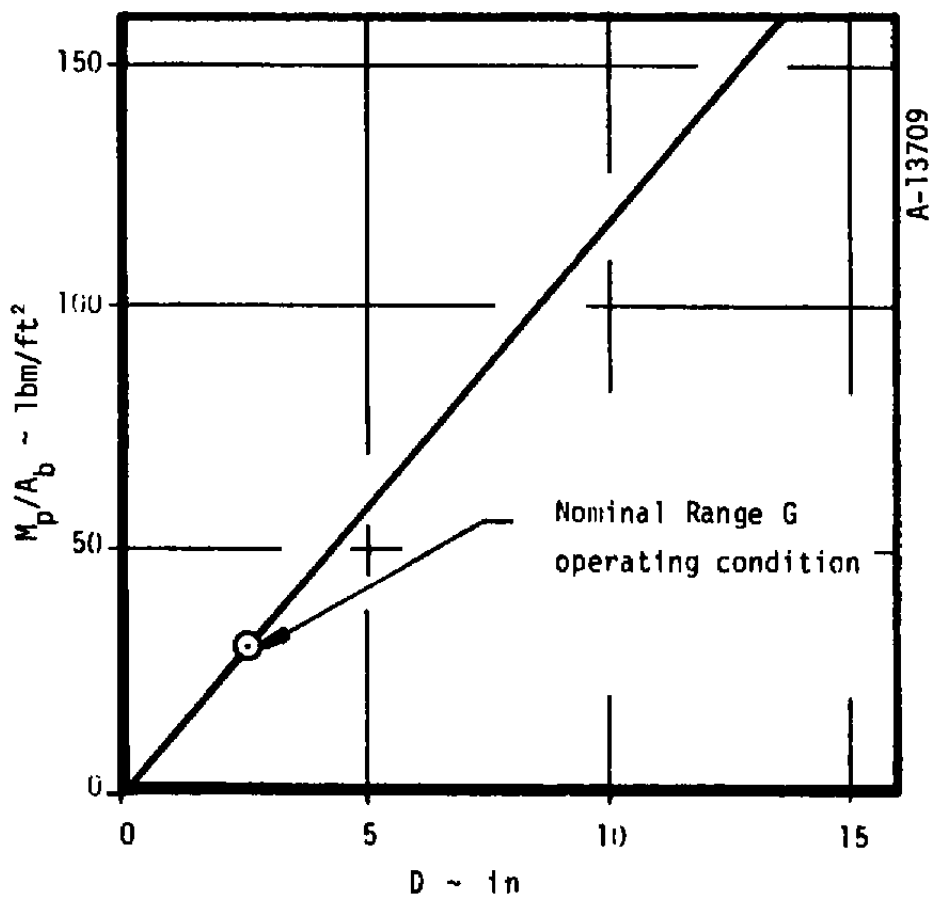
Figure 2-1. Projectile mass per unit base
area relation dictated by
launch considerations.

The ballistic coefficient is defined as

$$\beta \equiv \frac{1}{C_D}\left(\frac{M_p}{A_b}\right) \qquad (2\text{-}6)$$

where

C_D = drag coefficient

Assuming a sphere-cone projectile configuration, the drag coefficient for hypersonic conditions is a function of

$$C_D = f(D, R_N, \theta_c) \qquad (2\text{-}7)$$

where

R_N = projectile nose radius

θ_c = cone half angle

Combining Relations (2-6) and (2-7) and Relation (2-5) from launch considerations results in the functional relation

$$\beta = f(D, R_N, \theta_c) \qquad (2\text{-}8)$$

A plot of nominal ballistic coefficient versus projectile diameter (D) is shown in Figure 2-2. For this plot (and in the remainder of this study) a nose radius (R_N) of 1.0 inch and cone half-angle (θ_c) of 8° was assumed. These values are quite typical of ballistic reentry vehicles.

2.3 RECOVERY CONSTRAINTS

The relations governing projectile recovery are quite similar to those for launch; namely dynamics, kinematics, and design constraints. The dynamic relation is again

$$P_R = \left(\frac{M_p}{A_b}\right) a_R \qquad (2\text{-}9)$$

where

P_R = recovery pressure

a_R = recovery deceleration rate
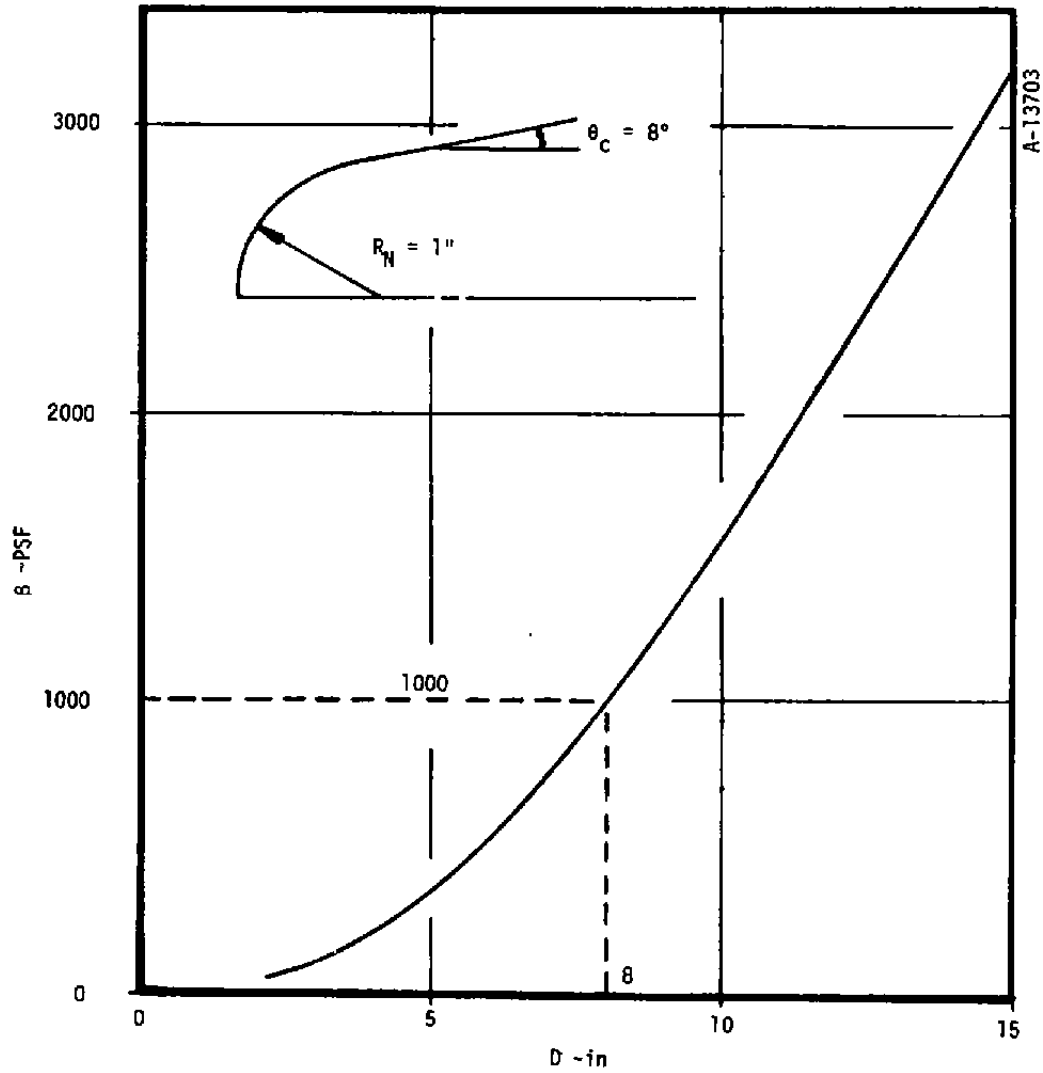
Figure 2-2. Nominal ballistic coefficient versus
projectile diameter.

Combining Equation (2-9) with Relation (2-5) from launch considerations gives

$$P_R \sim Da_R \tag{2-10}$$

Values of recovery pressure (P_R) versus projectile diameter (D) for various deceleration rates (a_R) are shown plotted in Figure 2-3.

The constant deceleration kinematic relation is again similar to launch

$$\text{Tube length} \approx \frac{V_{entry}^2}{2a_R} \tag{2-11}$$

Equation (2-11) is only approximate because an actual recovery tube will have to be longer than the distance required to bring the projectile to rest at constant deceleration. This is because additional length will have to be added to allow for the shock wave which proceeds the projectile in the tube. Nevertheless, Equation (2-11) does show that the required tube length will increase inversely with deceleration rate. Nominal deceleration distances calculated using Equation (2-11) are indicated on Figure 2-3.

The final consideration for recovery is imposed by tube mechanical strength limits. A conservatively approximate relation for the required tube thickness to support a given pressure is given by the thick wall tube equation (Reference 5).

$$\text{Tube O.D.} \approx \frac{S_s D^2}{2(S_s - P_R)} \tag{2-12}$$

where

$$S_s = \frac{\text{Maximum shear stress}}{\text{Factor of safety}}$$

For a nominal carbon steel and a factor of safety of 2.0, Equation (2-12) indicates a maximum allowable recovery pressure of about 750 atm. Greater pressures would require higher strength alloy steels.

2.4 SYSTEM SIZING CONCLUSIONS

From Figures 2-2 and 2-3 it is readily apparent that the key recovery tube design parameters are projectile diameter and recovery deceleration rate. The range of diameters of interest is limited on the low end by the requirement for a moderately high ballistic coefficent (Figure 2-2). Diameter is limited on the high side by both recovery tube pressure (Figure 2-3) and probably also costs.
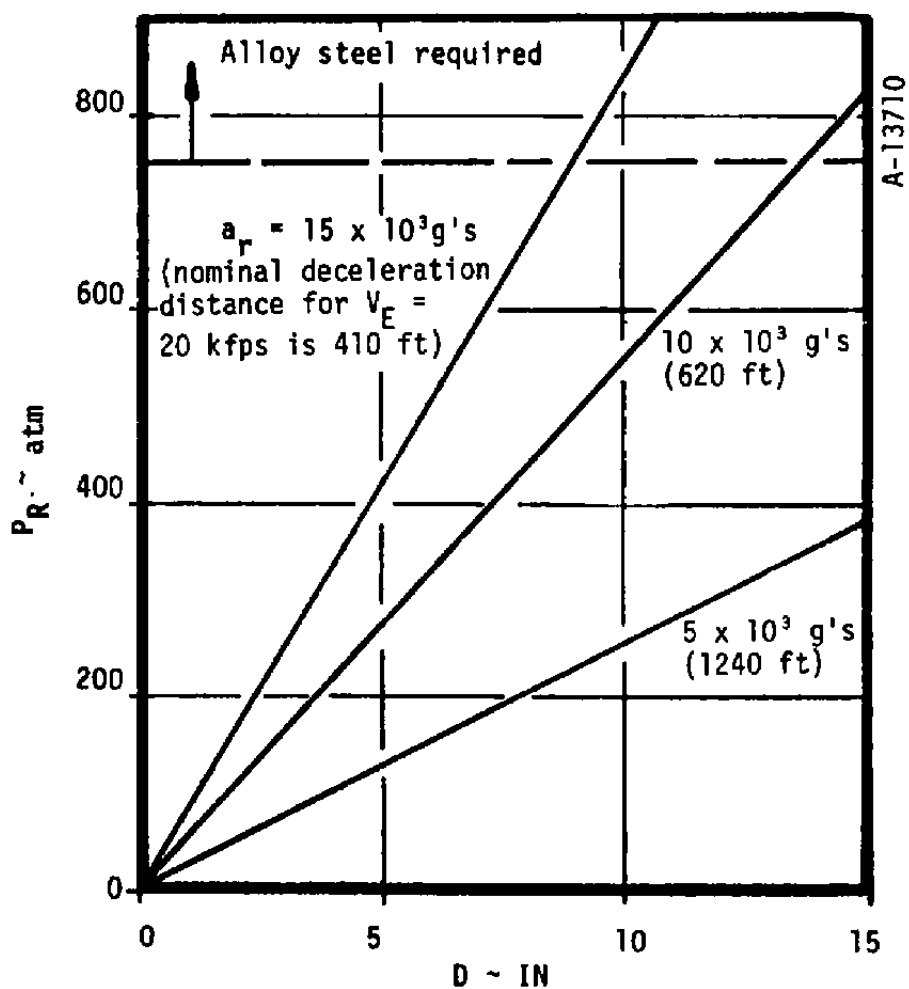
Figure 2-3.   Recovery tube pressure versus projectile
diameter for various deceleration rates.

The upper value for recovery tube deceleration rates of interest is similarly dictated by recovery tube pressure (Figure 2-3). The lower value of deceleration is constrained by the longer tube lengths required as deceleration rate is reduced.

Based on the above considerations and discussions with AEDC technical people, the following baseline conditions were established:

D = 8 inches

B = 1000 psf

a_R = 8 x 10^3 g's

P_R = 356 atm

In latter sections optimum recovery tube conditions will be determined by considering the effects of design variations from the baseline.

For all calculations of model damage which follow the nosetip model was assumed to be reconstructed of ATJ-S graphite. This is a reasonable baseline material since it is likely that in the foreseeable future new nosetip materials will continue to be graphitic because of the extremely favorable thermochemical properties of graphite.

SECTION 3
GENERAL FEATURES OF RECOVERY TUBES

In the introduction of this report the recovery tube concept was discussed. Namely, model recovery is designed to occur in a tube containing a gas at elevated pressure. In this section several alternate means of achieving model slowdown by use of pressure forces are discussed. The methods presented vary in complexity and practicality. The ultimate choice of the optimum method must necessarily relate to other considerations such as material strength limitations. In the sections which follow the alternate methods for achieving model slowdown are discussed and compared on a qualitative and quantitative basis. The analytical techniques used to perform the quantitative comparison are discussed briefly. Finally, the candidate recovery tube concepts are compared on the basis of preliminary calculation techniques.

3.1   RECOVERY TUBE CONCEPTS

In this study, four different types of recovery tube concepts were considered. They were:

1.   The "open" tube

2.   "Closed" tube

3.   Combined "open/closed" tube

4.   Compartmented closed tube.

In each of the concepts, 1 through 4, the recovery tube is used to decelerate the model from high velocities (~20000 fps) to low velocity (~1000 fps). This deceleration process is accomplished primarily by pressure forces generated by compression of a gas. The tube gas is contained at a pressurized state (generally greater than 1 atm) before the model enters the tube. Hence, a common feature is that each concept contains at least two valves to create a prepressurized state prior to model entrance.

As stated above, after the model enters the tube, pressure forces decelerate the model to some low velocity, taken to be 1000 fps in this study. Slowdown from 1000 fps to rest would be accomplished by frictional means such as converging rails.

3.1.1 "Open" Tube Concept

The open tube concept is depicted in Figure 3-1. Here the recovery tube consists of a single pressurized compartment with valves at either end. As the model departs the range $(t = t_1)$, it enters the prepressurized tube $(t = t_2)$ at high velocity and a shock wave is formed ahead of the model. This shock wave will continue to move away from the projectile with time. Meanwhile, the projectile begins to decelerate owing to high pressure forces on the face produced by shock wave compression.

As the porjectile decelerates, expansion waves emanate which eventually overtake the shock wave and weaken it. This causes the projectile deceleration to decrease. Thus, the efficiency of the deceleration process is degraded owing to a weakening of the primary shock wave. Therefore, the required tube length may be excessively great for this method.

The method offers simplicity which leads to less concern of valve timing and associated hardware and operating costs. By opening the downstream valve at the proper time the tube can be easily vented, eliminating model rebound. The obvious disadvantage of this approach is the long tube length required and associated costs.

3.1.2 Closed Tube Concept

The closed tube concept is presented in Figure 3-2. Here, the principal of operation is very similar to the open tube concept. Again, a single prepressurized compartment is used.

However, the primary shock wave ahead of the projectile eventually strikes the closed end of the tube, it is reflected, thereby reprocessing the gas behind this shock to higher pressure levels. Eventually, the reflected shock strikes the projectile and reflects from it, thereby, recompressing the gas a second time. This process may be repeated several times.

The disadvantage of this method is that both the projectile and the tube are subjected to very high impulse loads. These loads can lead to either model or tube damage. In addition, the large impulse loads may eventually cause the model to reverse direction in the tube. This latter condition could be alleviated by venting the downstream end of the tube at the proper time.

The closed tube concept has the potential for a shorter tube than the open tube concept.

3.1.3 Combined Open/Closed Tube Concept

Each of the two methods discussed above have inherent advantages. It seems reasonable to attempt to combine the two approaches. Figure 3-3 shows the combined open/closed tube arrangement.

23
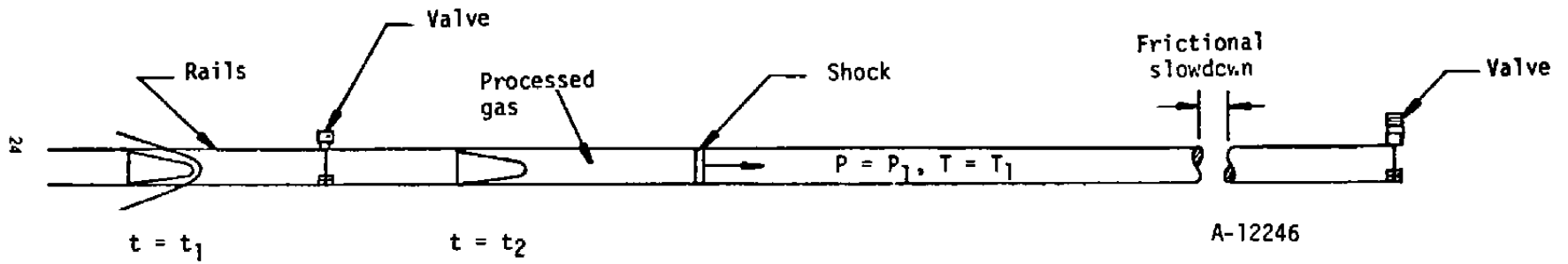
Figure 3-1. "Open" tube concept.

A-12244

P_2 → P_1 t_1

P_2 → P_3 t_2

P_4 → P_3 t_3
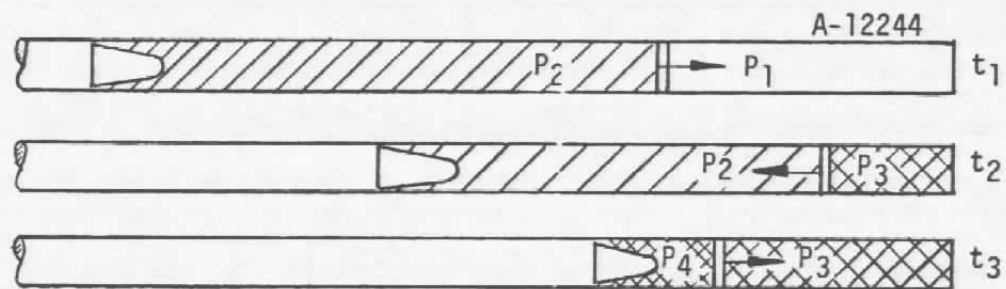
Figure 3-2.   Closed tube concept.
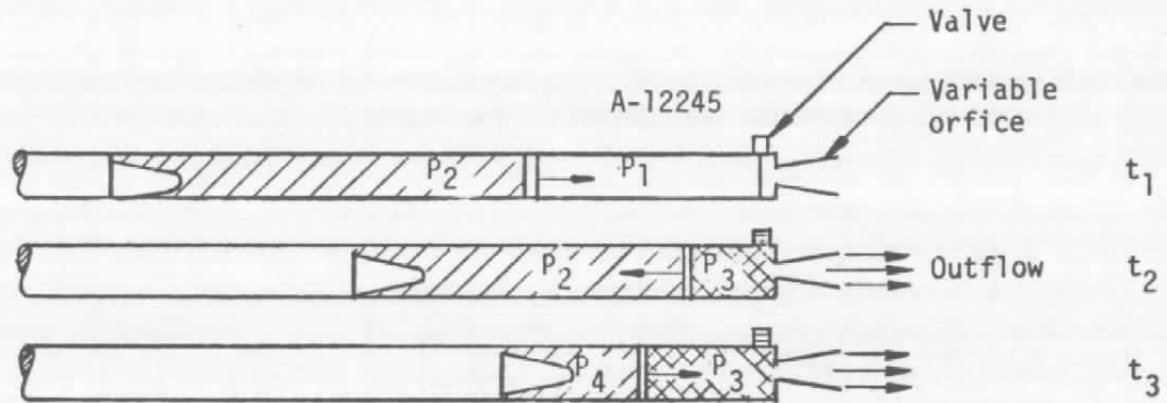
Figure 3-3.   Combined open/closed tube concept.

Again, a single prepressurized tube is used. However, at the downstream end a variable orifice/ valve is used to modulate the outflow and thus control the strength of the reflected shock.

By controlling the strength of the reflected shock it appears that model and tube damage can be avoided. At the same time, it is probable that the tube length can be reduced compared to the open tube concept because a reflected shock is utilized to assist in model slowdown. Also, by modulating the outflow a variety of operational modes can be achieved and deceleration rates preprogrammed.

The disadvantage of this method is the added complexity of operation as compared to the open and closed tube concepts.

3.1.4 Compartmented Tube Concept

An alternate method of achieving a tailored projectile deceleration is by means of the compartmented tube concept. Here the recovery tube is divided into several pressurized compartments as shown in Figure 3-4. Each compartment is separated from its neighbors by quick action valves. The principal of operation is the same as for the other concepts until the main shock approaches the end of the first compartment. At this time, a valve would be opened to expose the main shock to a higher pressure gas. Subsequent to a development period associated with valve opening timing and finite opening time, an incident shock is formed which eventually intercepts the model. The pressure rise associated with this interception serves to offset the rarefactions due to model deceleration. The main shock will continue down the tube and new incident shocks will be established at the location of each valve.

In this manner the pressure variation on the projectile face can be held within reasonable limits. This will insure a nearly constant deceleration rate, thereby, minimizing required tube length. This will also reduce the time of exposure, ostensibly limiting model damage as compared to other tube concepts discussed.

The obvious disadvantages of this approach are: the complexity of the system with regard to number of valves which require exact timing; complex pretest procedures to pressurize compartments, check valves, etc.; and the inherent danger of model damage due to a malfunction of one or more of the valves.

3.2 RELATIVE EVALUATION OF RECOVERY TUBE CONCEPTS

In order to determine the merits of the various recovery tube concepts discussed in Section 3.1 an analytical evaluation was performed. The tools developed for this comparison contain some simplifications which should not disturb the basic validity of the results.

Compartments

Valves

Incident
shock

Transmitted
shock

t_1

t_2

A-12252
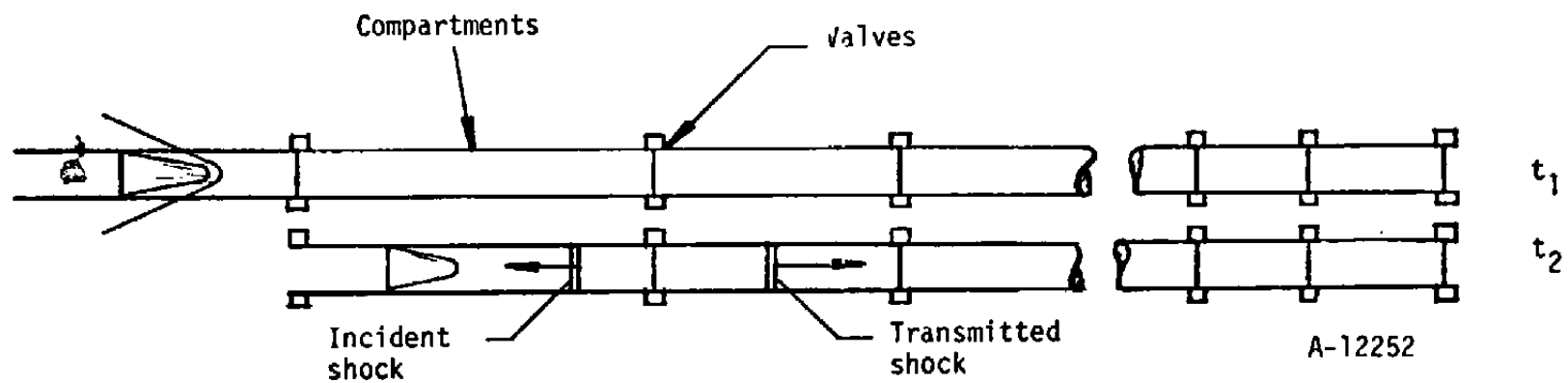
Figure 3-4.   Compartmentalized tube concept.

The approach taken was to utilize a simplified method of characteristics approach in the space-time (x,t) computational plane. This approach is physically appealing since characteristics represent weak wave trajectories in the x,t plane. A detailed discussion of the fundamentals of these methods may be found in References 21 and 30.

In addition, the gas was assumed to be ideal. For the comparative evaluation the test gas was assumed to be helium. The method of characteristics procedure was taken to be of a "shock-expansion" type. This assumes that when a weak wave (expansion or compression) intercepts a shock the reflected wave is extremely weak and can be ignored. Shock-expansion assumptions such as those mentioned above are not overly restrictive and generally lead to good results (see References 21 and 30).

Projectile dynamics are treated by a simple Newtonian force balance, $F = PA = ma$. Projectile motion is thereby controlled by the pressure felt on the face.

Two basic computer codes were used. The first deals with the open tube problem and the second treats the compartmented problem. The output of these analysis methods gives shock trajectory, projectile trajectory and inviscid flow properties between the projectile and the shock.

The following paragraphs describe some of the results of the evaluations. In the results to be discussed certain variables were held fixed. These include the initial velocity (18.3K fps), projectile mass per unit cross-sectional area (94.3 lbm/ft^2), and initial projectile pressure (445 atm). The last two conditions are consistent with an initial deceleration of 10^4/g's. As noted previously the test gas was assumed to be helium.

3.2.1 Open Tube Analysis

The results of the open tube analysis are presented in Figures 3-5 and 3-6. The method of characteristics code was used to generate the wave diagram shown in Figure 3-5. Here, the projectile path forms the left boundary of the wave diagram.

Expansion waves are shown emanating from the projectile face and eventually overtaking the primary shock, thereby slowing its velocity. Once the projectile is slowed to 1000 fps a left running expansion wave is traced through the expansion wave system back to the shock. The intersection of this left running wave and the shock actually determines the required tube length of about 2100 feet, as shown. That is, if venting occurs at this location and time, the first expansion wave would reach the projectile just as it slowed to 1000 fps.

The face pressure and velocity history of the projectile are shown in Figure 3-6. Note that the rate of pressure drop is rapid initially, and then begins to level off. Also, the deceleration (the slope of the u_p-t curve) decreases steadily with time.
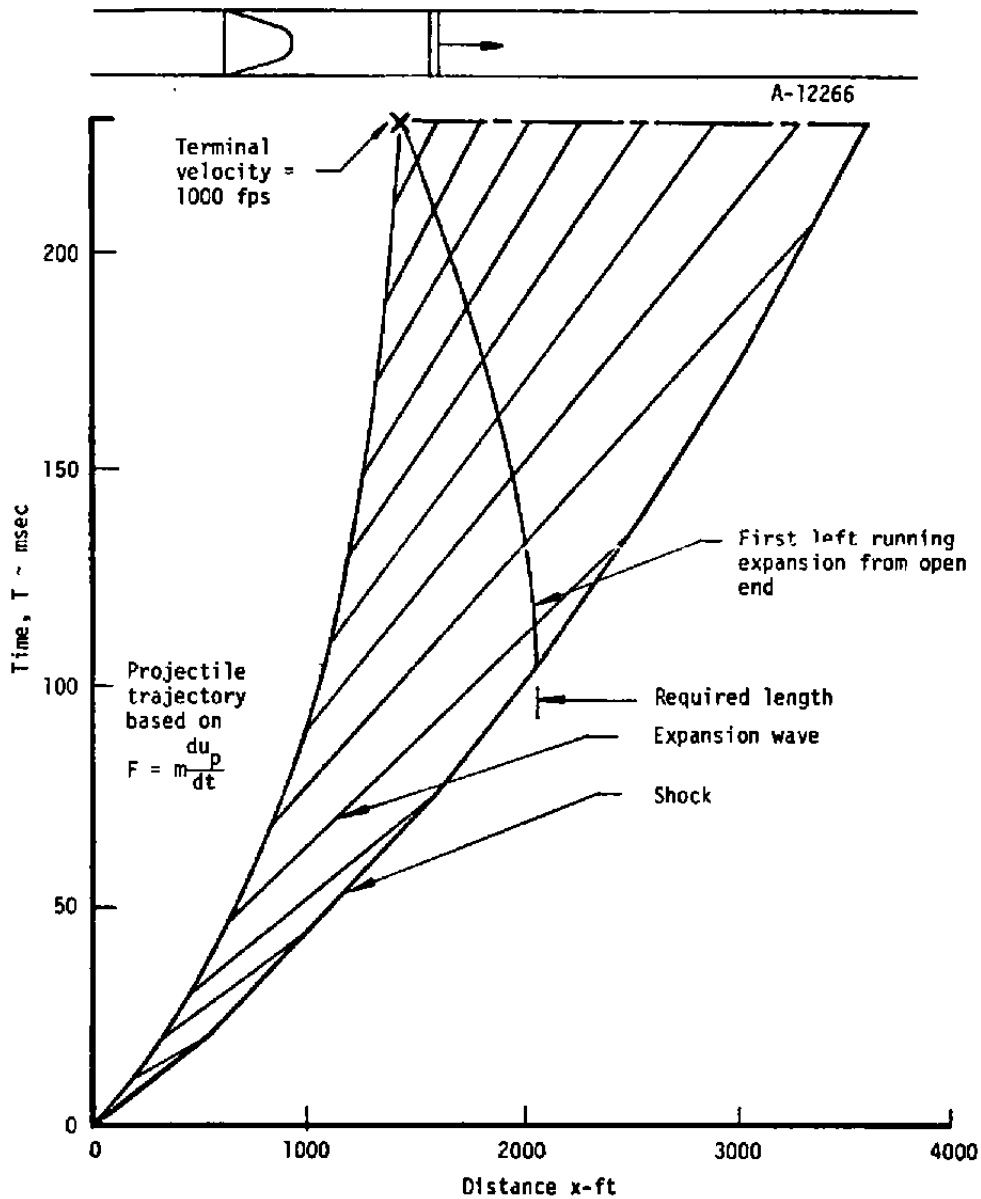
Figure 3-5. Open tube analysis wave diagram.
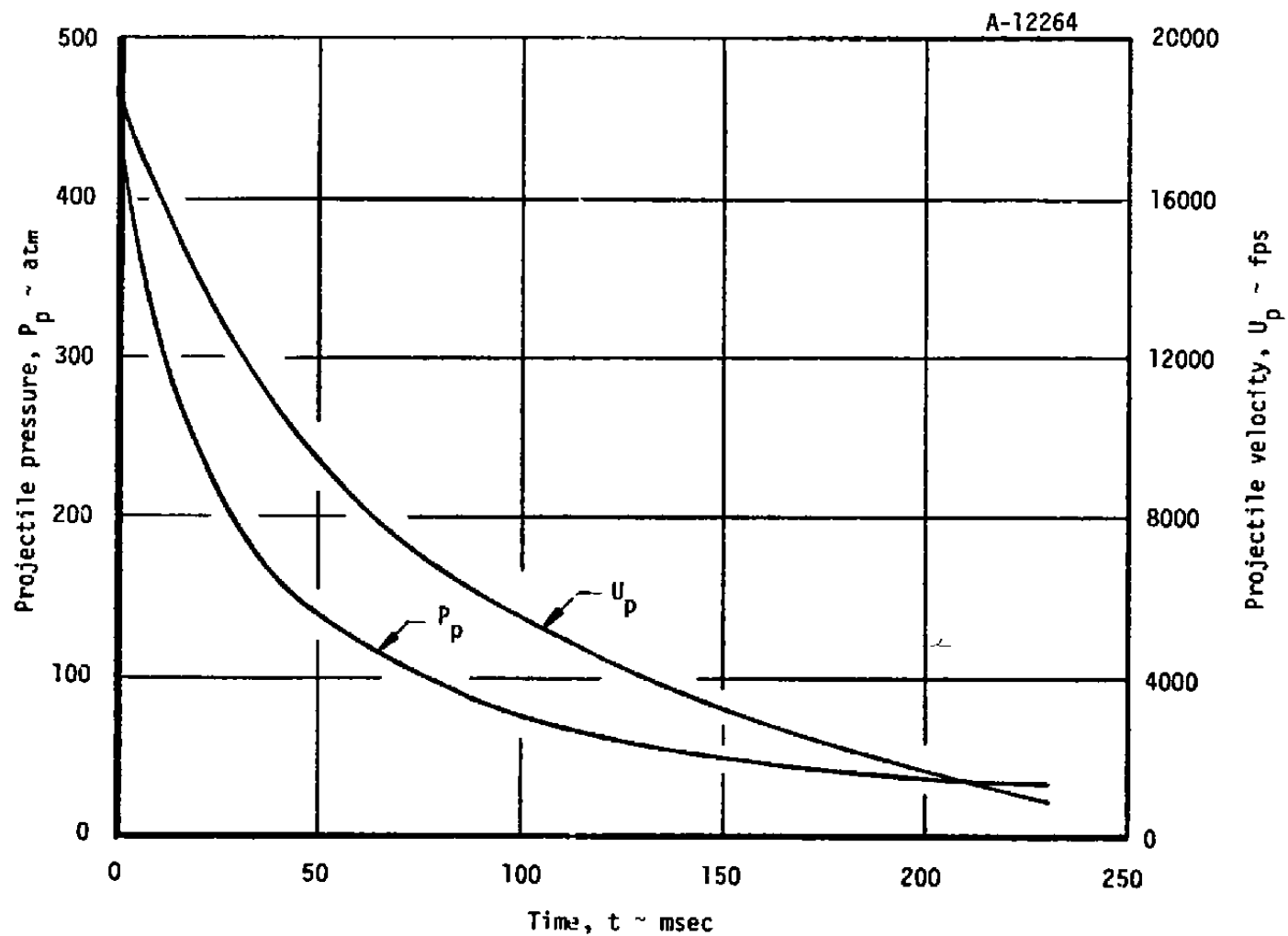
Figure 3-6. Projectile face pressure and velocity for open tube analysis.

3.2.2 Closed Tube Analysis

An evaluation of the closed tube concept was performed. The analysis was initiated by using the results from the open tube analysis. Then a closed end location was selected, and the remainder of the analysis was carried out by hand calculation.

The wave diagram for the closed tube analysis is shown in Figure 3-7. The reflected shock off the closed end was followed back to the projectile where it reflects again. Here the boundary condition is somewhat different since the boundary (i.e., projectile) is in motion.

The peak pressures following shock reflection from the projectile depend upon the choice of tube length, as shown in Figure 3-8. It is clear that minimum tube length for this scheme would be approximately 1000 feet, based on tube material strength limitations. Based on considerations of cost increase with pressure that must be contained, the shorter closed tube requirement probably represents no economy over the open tube, particularly since they must both be approximately 2000 feet long to be compatible with low cost steels.

3.2.3 Combined Open/Closed Tube Analysis

The combined open/closed tube analysis was not performed. It was concluded that the combined approach would necessarily require a longer tube length than would be obtained with a compartmentalized tube due to less uniformity of deceleration. However, it would probably be shorter than the closed tube approach considered above, since the closed tube length is dictated more by tube pressure limits than model stopping distance. This concept will be considered further in Subsection 3.3.

For completeness, a schematic of the analysis approach for such a tube concept is depicted in Figure 3-9. Essentially, the analysis would be similar to the closed tube analysis except that at the tube end a net outflow would be allowed. This type of boundary condition would reduce the strength of the reflected shock wave.

3.2.4 Compartmented Tube Analysis

Although the analysis method used here is also a simple characteristics solution, the procedure itself is somewhat unique in that an indirect approach is required. Here it was assumed that the projectile deceleration remains absolutely constant at 10 Kg's. This required the projectile face pressure to be constant.

In order to achieve this limiting condition, an infinite number of compartments would be required. This idealization does not limit the validity of the calculation. Hence, both the projectile trajectory (through the known deceleration) and face pressure are known apriori. It is, therefore,
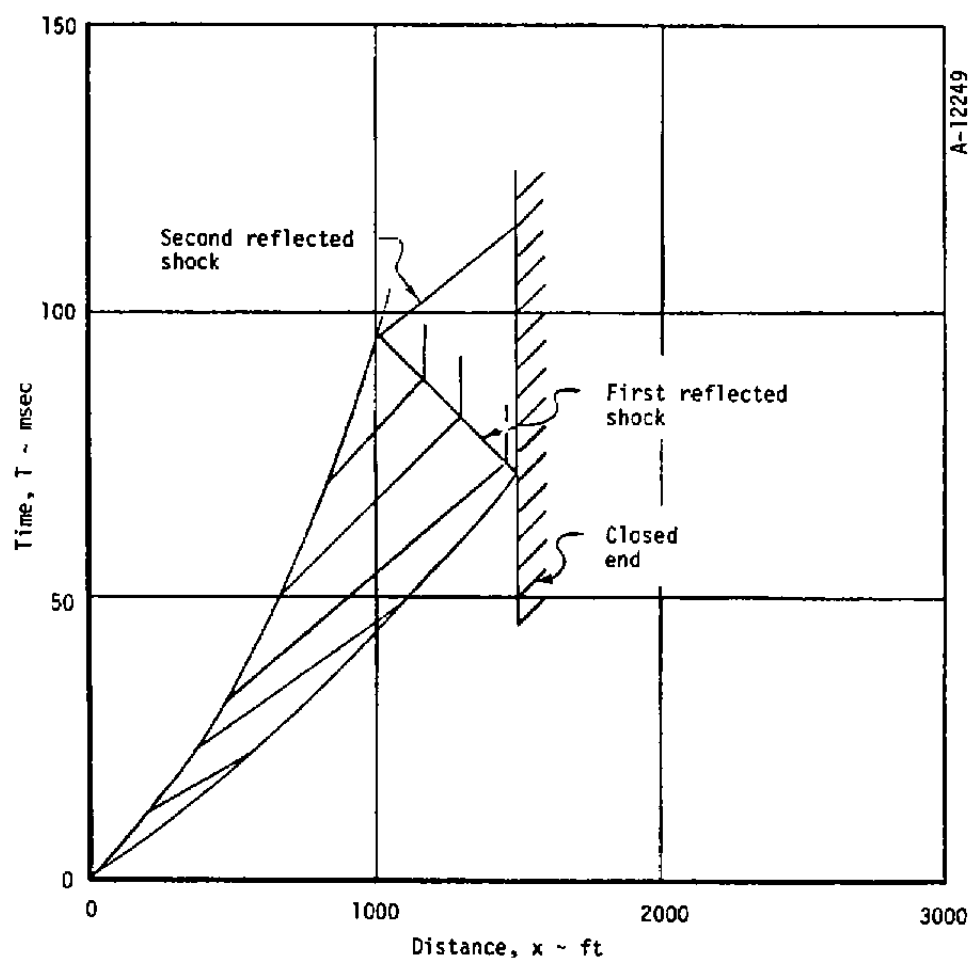
Figure 3-7. Closed tube analysis wave diagram.
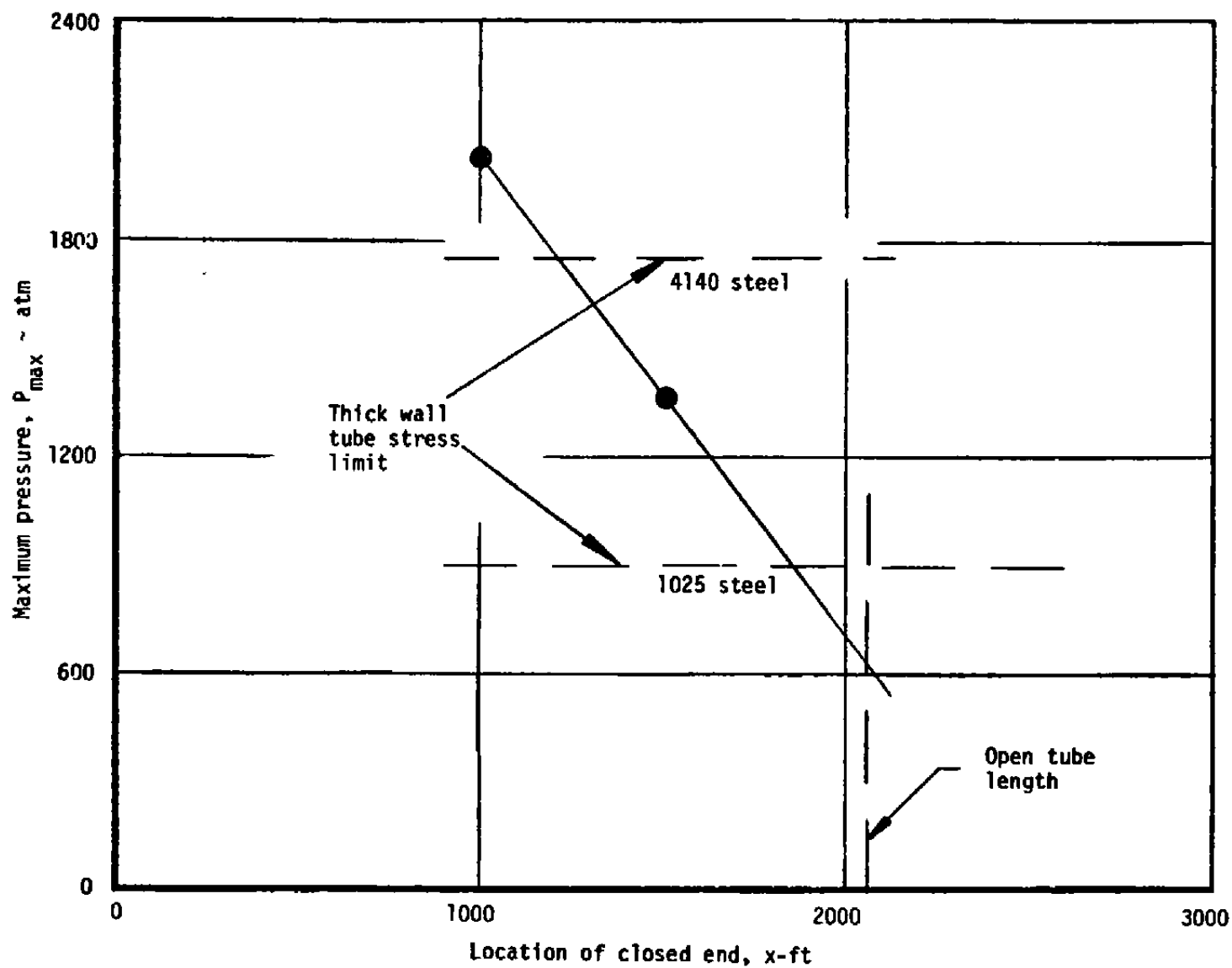
Figure 3-8. Projectile face pressure after first shock reflection.
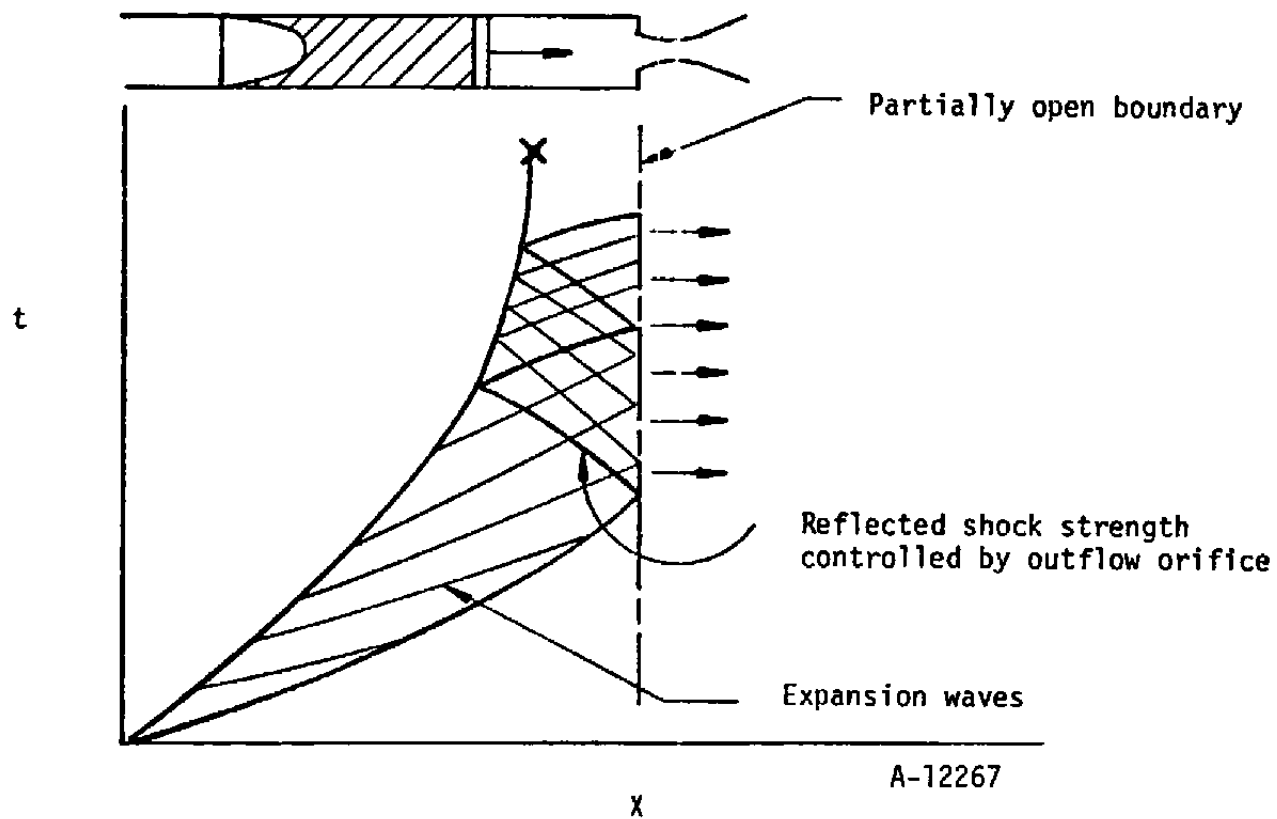
Figure 3-9. Combined open/closed tube analysis wave diagram.

required to find the pressure distribution ahead of the shock, that is, the compartment pressures. Thus, it can be seen that the method is an indirect one, but one which the method of characteristics handles easily.

Figure 3-10 shows the wave diagram for the problem described above. In the finite approximation a select number of waves are used to generate the wave diagram. Note that each time an expansion reaches the primary shock a compression is emanated due to exposure of a new compartment, which just cancels the effect of the expansion. In this manner the face pressure is held constant.

Again the required tube length is determined by tracing an expansion wave from the projectile face to the shock at the time when the projectile reaches 1000 fps. Thus, for the compartmented tube concept, the required length was found to be about 700 feet for an average deceleration of 10^4 G's.

The projectile face pressure and projectile velocity histories are shown in Figure 3-11. Note that both the projectile pressure and deceleration are absolutely constant. Figure 3-12 shows the resultant smooth variation of compartment pressures required to maintain those constant conditions shown in Figure 3-11. It should be noted that in order to achieve constant deceleration, tube pre-pressures must be selected which cause higher pressures behind the shock than those appearing at the projectile (peak pressure for this example is 670 atm when the principal shock reaches the end of the tube at about 40 msec).

In the next section of this report an exact procedure for performing the compartmented problem analysis will be described. However, that method cannot predict the required compartment pressures and is only capable of handling a direct type of problem. Consequently, the indirect analysis described here was used to define appropriate required compartment pressures.

Rather than use an infinite number of compartments, however, the practical problem of considering a finite number of compartments was desired. Consequently, an iterative scheme was developed to predict, approximately, the required pressures in a finite number of compartments by using the smooth infinite compartment results. This procedure is described in Subsection 4.1.2.

3.3   SUMMARY OF RESULTS OF TUBE CONCEPTS

Table 3-1 summarizes the results of required tube lengths and model transit times for the tube concepts considered. The compartmented tube concept was a factor of 3 better than the open tube concept on the basis of required tube length. The time of model exposure for the compartmented tube was almost a factor-of-4 better than the open tube concept. In view of these results, the compartmented tube concept was selected to be best and was the concept used in all subsequent calculations in this report.
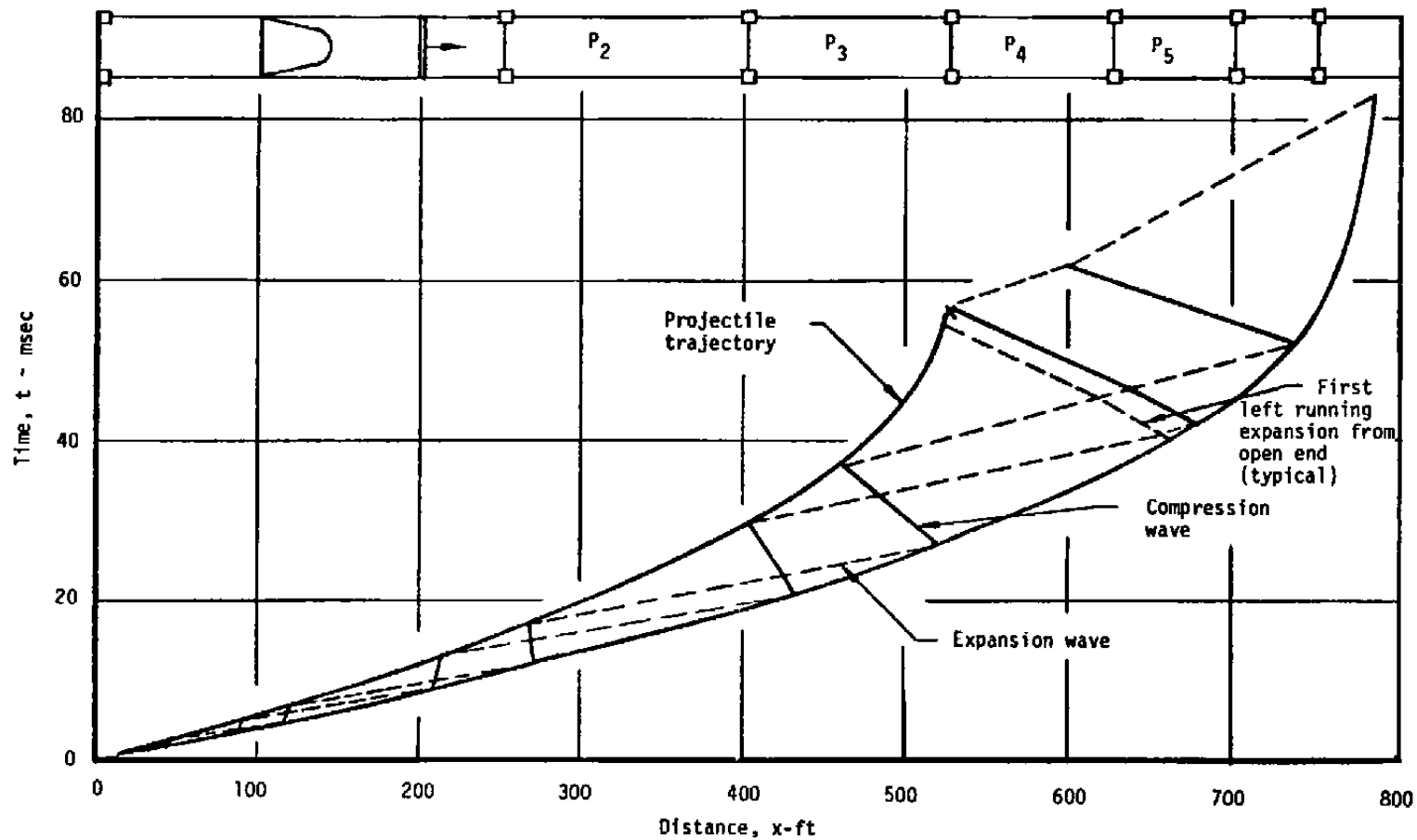
Figure 3-10. Compartmentalized tube analysis wave diagram.
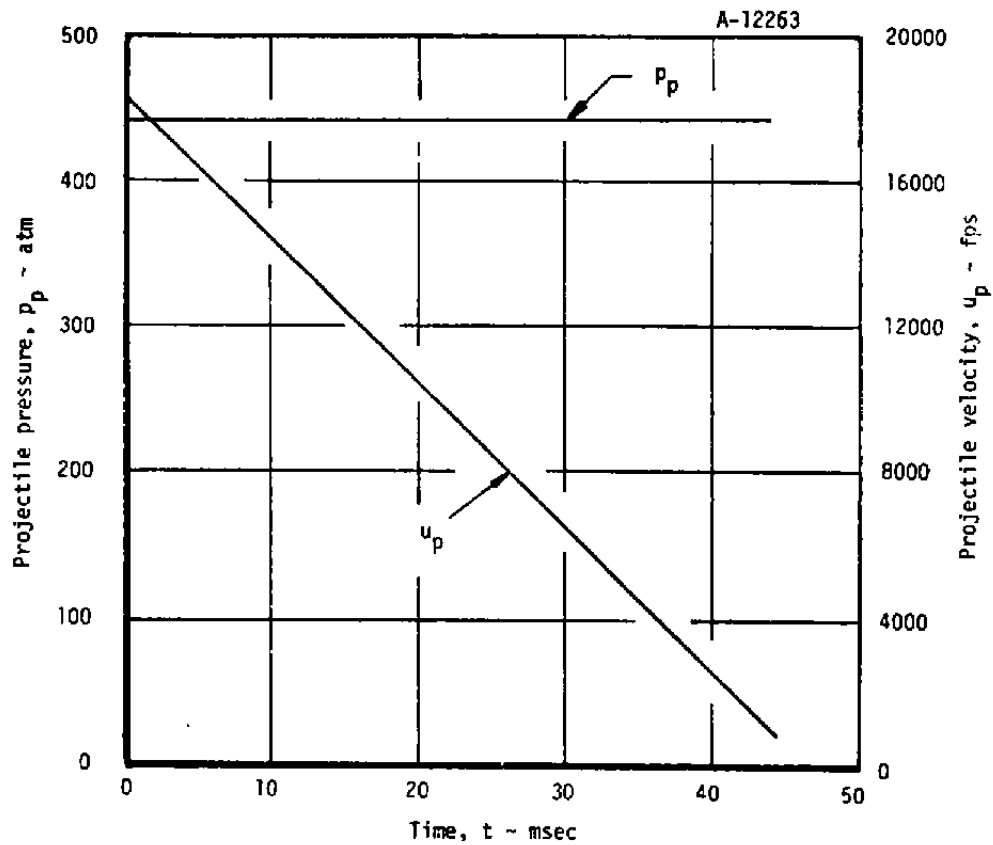
Figure 3-11. Projectile face pressure and velocity
for compartmentalized tube analysis.
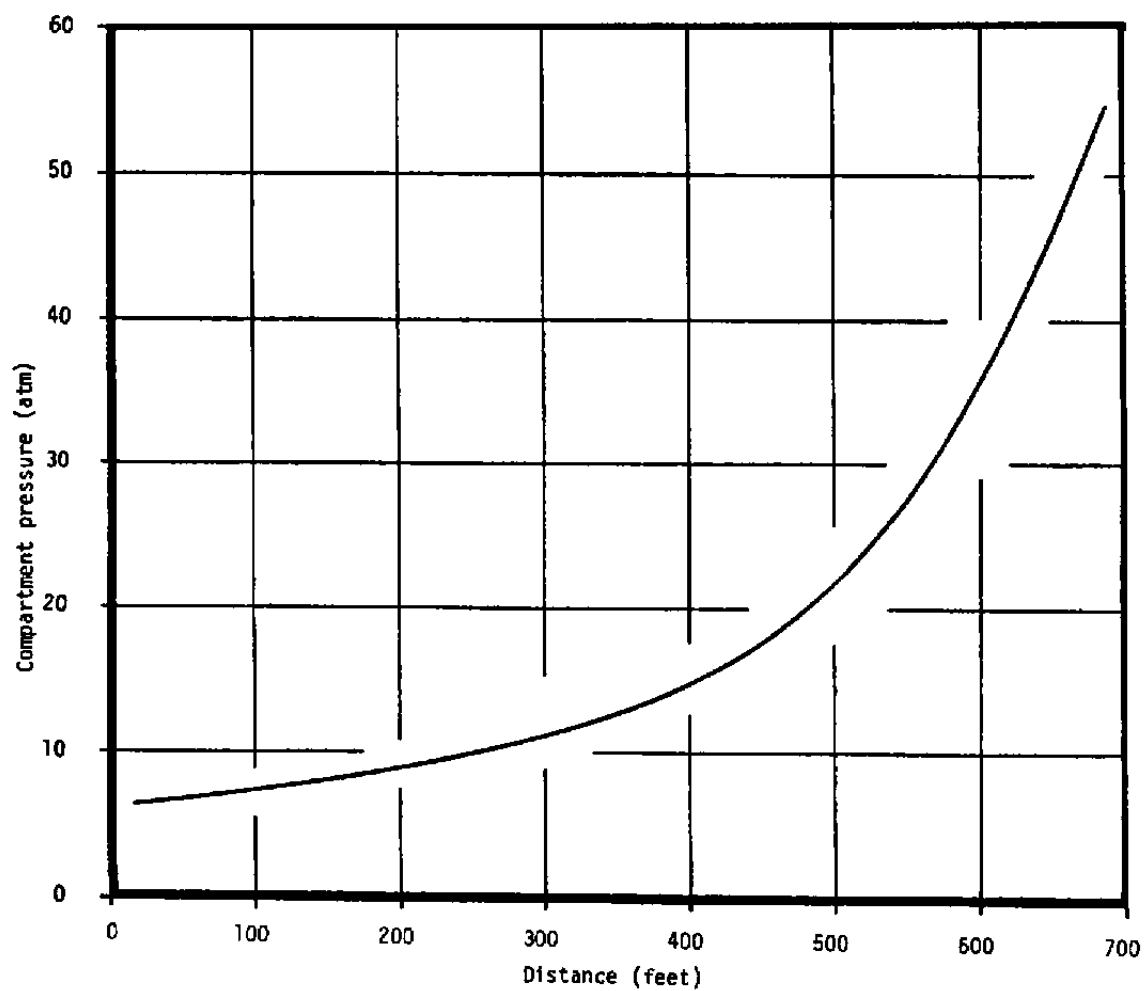
Figure 3-12. Required prepressurized compartment pressures.

TABLE 3-1. SUMMARY OF DYNAMIC BEHAVIOR OF CONCEPTS

(for $a_{INITIAL} = 10^4$ G's)

Type	Tube Length (ft)	Projectile Travel (ft)	Travel Time (msec)
Open	2100	1400	230
Closed	≈2000	(Based on P reflected = 750 atm)	
Combined	--	--	--
Compartmented	700	525	57

This selection does not obviate the use of a compartmented tube design in the combined open/closed tube mode which is described in Subsections 3.1.3 and 3.2.3. The combined mode should yield behavior which is approximately analogous to that obtained with a compartmented tube with only two compartments, but with no need for the valve between compartments. This mode of operation might be considered at some later time, for it appears to have some operational advantages.

SECTION 4

TECHNIQUES FOR ASSESSING MODEL DAMAGE

A major part of this study was directed at predicting the level of model damage during recovery. The analytical techniques used to compute model damage are discussed in this section.

As indicated in the introduction model damage during recovery was expected to be due to three principal causes:

- ablation

- structural loading

- material property changes.

A quantitative evaluation of the above phenomena requires calculation of model thermal and structural response in both the range and in the recovery tube.

The calculation of model thermal and structural response is, in turn, dependent on a whole chain of physical phenomena which occur during recovery. The key elements in this chain of phenomena are illustrated in Figure 4-1. The rest of this section gives detailed descriptions of the analytical techniques used to model these key phenomena affecting model damage.

4.1   GAS AND MODEL DYNAMICS

A brief description of the operating principles of a compartmented recovery tube (which is the type considered here) was given in Section 3. Preliminary evaluations of that concept were made using a modeling technique which neglected certain wave interactions and assumed an infinite number of valves. In this section a more exact calculation for compartmented tubes with a finite number of valves is presented.

The system evaluated is one dimensional in space, and considers the time dependent behavior of a high speed piston in a tube. The analysis is that of Reference 6, which is outlined briefly here. The independent variables are positioned along the tube (x), and time (t), while the primary dependent variables are gas velocity (u), pressure (p), and specific volume (v) or density.
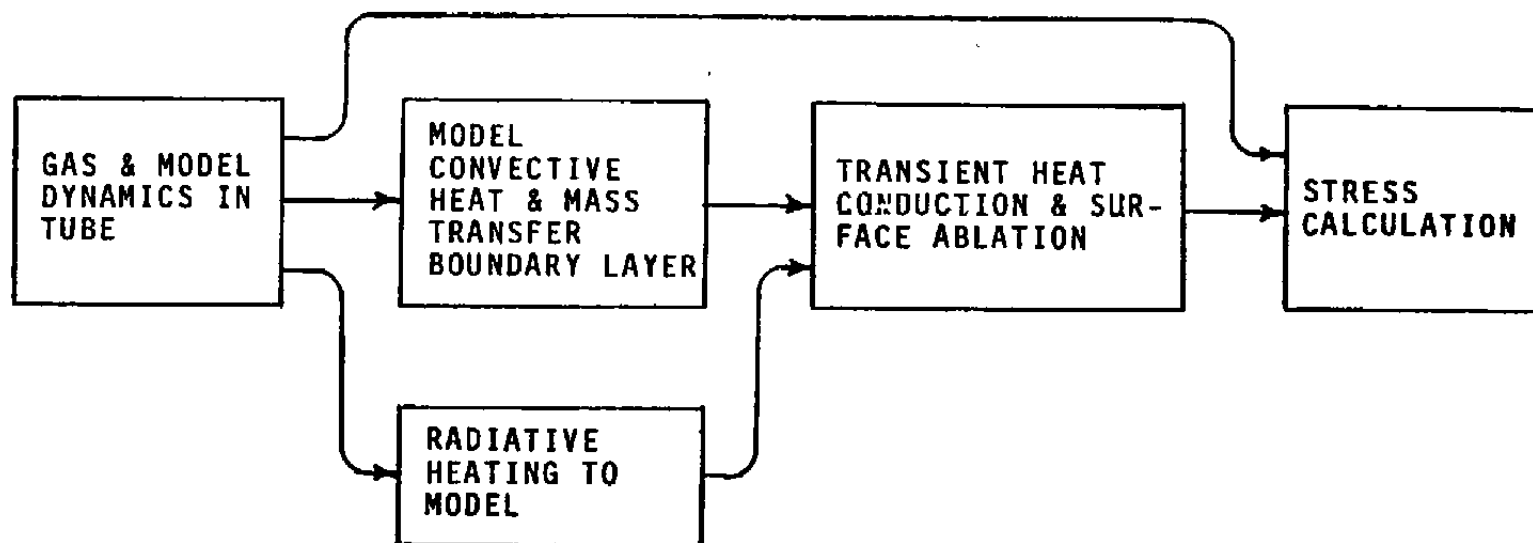
Figure 4-1. Key elements of model damage evaluation.

4.1.1 Analysis

An element of mass provides a convenient reference frame for writing the appropriate conservation equations. In differential form, conservation of mass, momentum and energy are expressed, respectively, as:

$$\partial v / \partial t = v \partial u / \partial x \qquad (4-1)$$

$$\partial u / \partial t = -v \partial p / \partial x \qquad (4-2)$$

$$\partial e / \partial t = -p \partial v / \partial t \qquad (4-3)$$

In Equation 4-3, e represents specific internal energy which is

$$e = pv / (\gamma - 1) \qquad (4-4)$$

for a perfect ideal gas,* where γ is the ratio of specific heats.

This system of differential equations tacitly assumes the flow field to vary continuously with respect to time and position. Thus, the system will not correctly determine the virtual discontinuities associated with shock fronts. The situation is corrected by including an artificial viscous mechanism in regions where compressions are tending to become shock front discontinuities. This mechanism insures that shock fronts will be relatively narrow zones (as compared to the scale of the flow field) of continuous change. While this shock structure does not conform to experimental observations, the state and flow properties outside the shock zones are predicted accurately.

The viscous mechanism (π) is a function of velocity gradients present in compressive regions:

$$\pi \equiv \begin{cases} 0, & \text{if } \partial v / \partial t \text{ or } \partial u / \partial x \geq 0 \\ \frac{1}{v} \left[C_L \sqrt{pv} \mid \frac{\partial u}{\partial x} dx \mid + (C_o \frac{\partial u}{\partial x} dx)^2 \right], & \text{otherwise} \end{cases} \qquad (4-5)$$

C_L and C_o are constants of an order of unity, selected so as to minimize the shock front zones. The parameter, π, has the dimension of pressure.

Hence the conservation equations are modified to include the artificial viscous mechanism. Replacing p with P, where:

---

*Perfect ideal gases are assumed for all evaluations of model/shock dynamics within the tube.

Hence, the conservation equations are modified to include the artificial viscous mechanism. Replacing p with P, where:

$$P \equiv p+\pi \qquad (4-6)$$

leads to modified forms of Eqs. 4-2 and 4-3:

$$\partial u/\partial t = -v\partial P/\partial x \qquad (4-7)$$

$$\partial e/\partial t = -P\partial v/\partial t \qquad (4-8)$$

However, since e is a state function, Equation 4-4 is not modified.

The kinematic relation between position and velocity is a consequence of differentiation along mass element paths, that is:

$$u = \partial x/\partial t \qquad (4-9)$$

It is included as an auxillary equation.

The initial, boundary, and auxillary conditions define the recovery tube configuration. The initial conditions are:

$$p_i = p(o,x) \qquad (4-10)$$

$$v_i = v(o,x) \qquad (4-11)$$

$$u_i = u(o,x) \qquad (4-12)$$

The auxiliary conditions partition the tube at $x = \ell_j (j=1, 2, \cdots, n-1)$ into n chambers:

$$u_{\ell_j} = u(t < t_j, \ell_j) = 0, \; j = 1, 2, \cdots, n-1 \qquad (4-13)$$

The times t_j (j = 1, 2, $\cdots$, n-1) are the instants when the initial shock front, generated as the piston enters the tube, reaches the partitions at $\ell_j (j = 1, 2, \cdots, n-1)$.

Model dynamics provide the closure condition for the system. Initially, the model velocity (u_m) is:

$$u_m(0,0) = u_{mi} \qquad (4\text{-}14)$$

Subsequently, from Newton's law (ignoring frictional effects)

$$d\left[u_m(t,r)\right]/dt = -p(t,r)A/m \qquad (4\text{-}15)$$

where r is the model position (x_{model}), A is the cross-sectional area of the model, and m is model mass.

A high-speed digital computer numerically generates the general solution:

$$\bar{u} = \bar{u}(t,x) \qquad (4\text{-}16)\text{a}$$

$$\bar{p} = \bar{p}(t,x) \qquad (4\text{-}16)\text{b}$$

$$\bar{v} = \bar{v}(t,x) \qquad (4\text{-}16)\text{c}$$

Contained within the general solution are the local conditions at the model; these include model velocity history:

$$u_m(t) = \bar{u}(t,r) \qquad (4\text{-}17)$$

and model pressure loading history:

$$p_m(t) = \bar{p}(t,r) \qquad (4\text{-}18)$$

4.1.2 Selection of Compartment Pressures

It is obvious that considerable freedom exists in the choice of compartment locations and pressure levels. It is also apparent that suboptimization within a given general configuration (e.g., number of compartments) is desirable in terms of maximizing benefits (or minimizing problems). However, the degree of optimization in this study is necessarily restricted to evaluations of general configurations. Thus, a scheme was developed to select compartment parameters which was deemed applicable to all general configurations, and at least systematic. No attempts were made to improve the definition of compartment parameters in response to the consequences of the selections as revealed by the gas/shock dynamics analysis results.

The procedure employed for these selections is outlined below.

1. Assume the principal shock Mach number and pressure ratio variation along the tube (x) with a finite number of compartments is the same as that derived from the infinitesimal compartment analysis of the previous section.

2. Select a compartment pressure p_1, so that the pressure behind the shock is equal to $p_2 + \Delta$ as the shock enters the compartment. P_2 is the pressure behind the shock at the same location, obtained in the infinitesimal compartment analysis.

3. Find the shock location, x_s, where $\dfrac{p_2 - \Delta}{p_2/p_1} = p_1$ (this location is found by iteration). This location is established as the downstream end of the compartment being defined, and the beginning of the next compartment.

4. Return to step 2, and continue developing compartment pressures and locations until the downstream end of a compartment exceeds the shock locations (x_{sf}) in the infinitesimal analysis that exists when the model velocity is reduced therein to 1000 feet per second.

5. Revise Δ, return to the beginning of the tube, and proceed through the selection of compartment locations and pressures. Continue to redefine Δ as necessary to obtain the condition where the last of the correct number of compartments has its terminus at x_{sf}.

The resulting data are then input to the tube gas dynamic analysis described above. However, the last compartment is allowed to be as long as necessary to accomplish the completion of model deceleration (≈ 1000 fps) without interference on the model of compression or expansion waves off a closed or open tube end, respectively.

4.1.3 Example Results

Figure 4-2 presents a schematic description of the wave structure within a three compartment recovery tube. The principal shock, C_1, is generated upon entrance to the tube. The strength of this shock is modified as it impinges on the higher pressures existing in the second and third compartments. It continues to be transmitted downstream and eventually emerges from the downstream end of the tube. The valves located at the downstream ends of the compartments are assumed to open instantaneously when the mass element just upstream of the valve experiences a pressure rise. This opening causes incident shocks to be generated (C_2, and subsequently C_3) which eventually reflect off the model (C_{2R}, and subsequently C_{3R}). At some point, C_{2R} and C_3 interact, and reflected shocks may overtake the principal shock. These interactions may cause extraordinarily high pressures to exist within the tube. The number of incident/reflected shock interractions is:
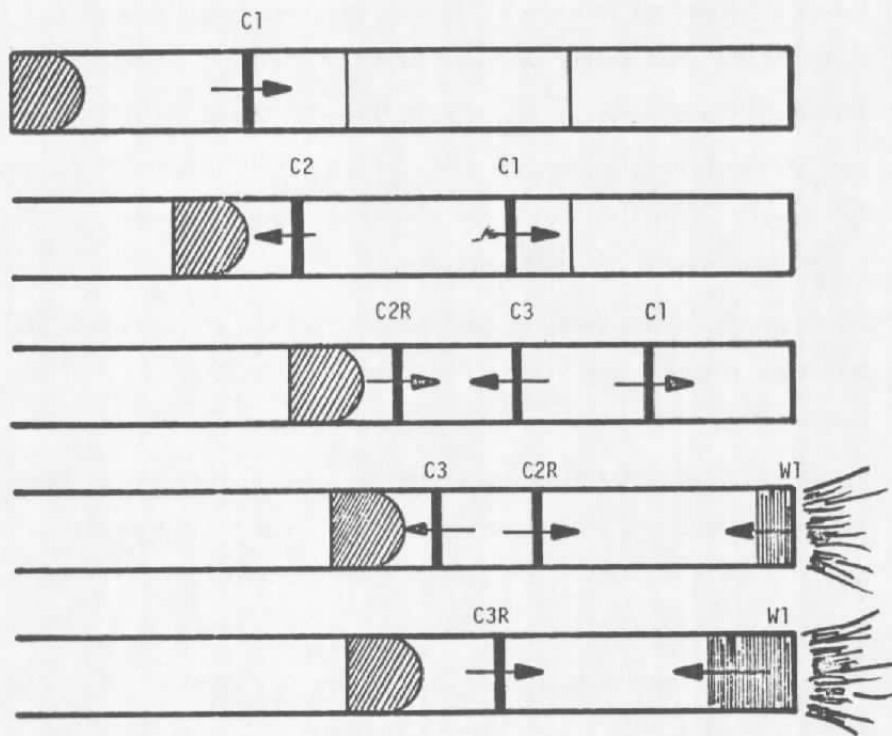
Figure 4-2. Model/shock dynamics — morphology.

$$\sum_{1}^{n-2} m \qquad\qquad (4-19)$$

where n is the number of compartments

TABLE 4-1. NUMBER OF SHOCK INTERACTIONS

No. of Compartments n	No. of Principal Shock Interactions n	No. of Incident/ Reflected Shock Interactions $\sum_{1}^{n-2} m$	Number of Reflected Shock/ Principal Shock Interactions $n-1$	Total Possible Shock Interactions
1	1	0	0	1
2	2	0	1	3
3	3	1	2	6
4	4	3	3	10
5	5	6	4	15
6	6	10	5	21
7	7	15	6	28
8	8	21	7	36
9	9	28	8	45
10	10	36	9	55

As shown in Table 4-1, the number of possible interactions increases remarkably with number of compartments. The strengths of these interactions are mitigated somewhat by the left traveling rarefaction wave, W_1, which is formed at the time that C_1 emerges from the down stream end of the tube (Figure 4-2), and by the right traveling rarefactions which emanate from the model. However, the probability of multiple and undesireable interactions occurring at the same position along the tube at any given time is high with a large number of compartments.

Figure 4-3 presents typical model and wave dynamic results for a 5 compartment tube. The wave diagram on the upper right of the figure shows the model and principal shock trajectories, as well as the incident shocks originated by the opening of the compartment valves (the shocks reflected off of the projectile are not shown). The compartment pressures, and the computed pressure distributions within the tube for two times are shown in the lower right hand part of the figure. The history of projectile velocity and projectile face pressure is shown in the upper left hand portion of the figure.

The tube pressure distribution results show that peak pressures within the tube occur far ahead of the model. In fact, shortly after the valve to compartment number 5 is opened in this
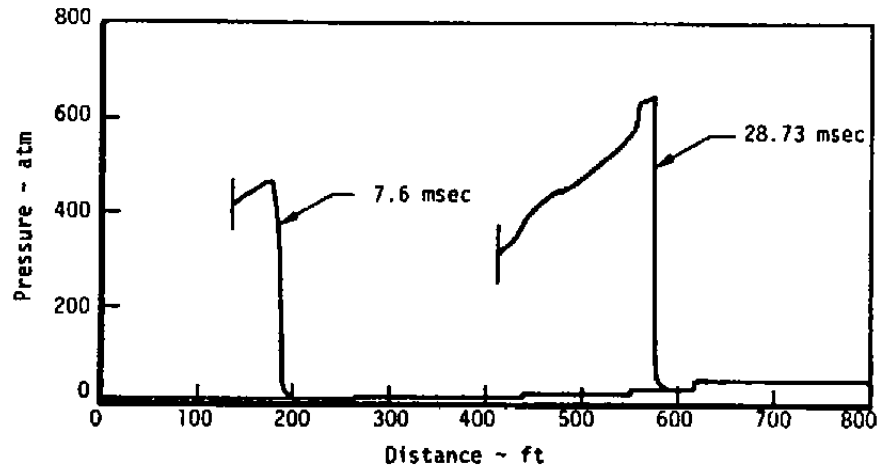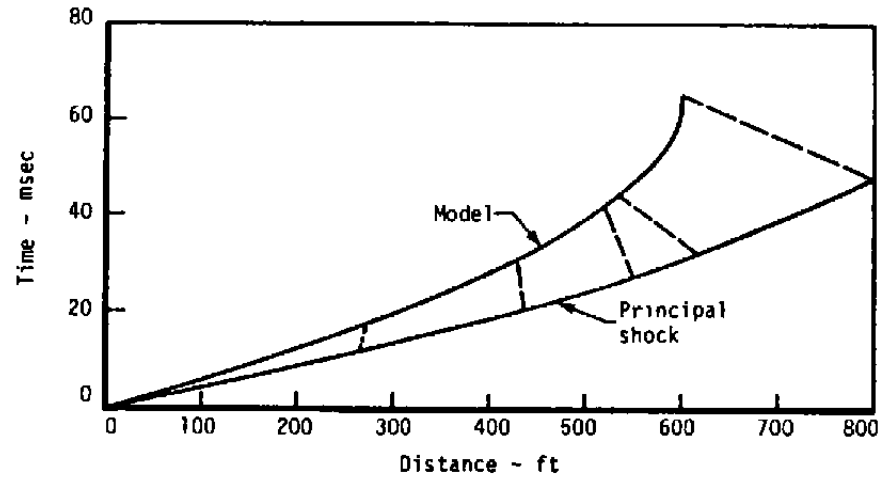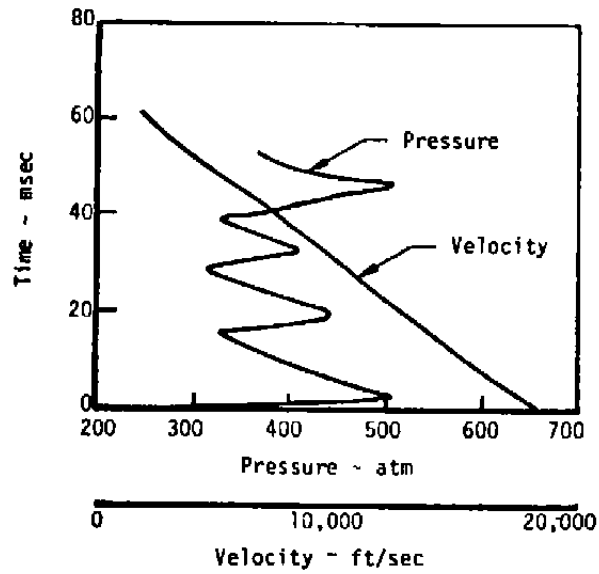
U_o = 18,364 ft/sec

D = 8 in

Accel = 10^4G (nominal)

m = 32.92 lbm

5 compartments

Figure 4-3. Typical dynamics results — compartmented tube.

example, the peak pressure is nearly 1200 asmospheres. However, the region of the tube over which these high pressures act is relatively small (see the 5 compartment results in Figure 6-4). The cause for the high pressure is the coalescence of the C_{2R} wave with the principal shock,* which approximately coincides in time with the interception of the principal shock with the entrance to the last compartment.

As indicated earlier, no attempts have been made to eliminate these high pressures. Rather, outputs from the calculations were scanned to establish duration and location of peak pressures, and tube strength characteristics were modified locally as necessary. This approach was dictated by the number of interactions that must be considered in order to improve matters. The associated effort is beyond the scope of the project.

4.2   MODEL CONVECTIVE HEATING

Convective heating of the model during recovery was anticipated to be the primary root cause of model damage. This was expected because convective heating leads to:

- Thermochemical ablation

- Thermal stresses causing structural loads

- High indepth temperature causing material property changes

For these reasons significant effort was devoted to determining convective heat transfer levels.

The problem of calculating model convective heat transfer in a recovery tube can be divided into three subproblems as follows:

- Definition of flow regimes (temporal and spatial) in the region between the model and the shock wave

- Evaluation of the flow field near the model using the flow regime definitions

- Evolution of the boundary layer over the model using the flow field near the model as a boundary condition.

The following sections describe the analysis of each of these aspects of the model heating problem.

---

*This coalescence can be seen in the pressure distribution at 28.73 msee in Figure 4-3, signified by the high pressure plateau of about 650 atm.

4.2.1 Evaluation of Tube Flow Regimes, Characteristics

Flow characteristics over the model while it is in tube are quite time dependent. These flows can be characterized in part with the aid of Figure 4-4. (Velocity vectors shown therein are gas velocities relative to the model).

Early Times

Prior to model exit of the range, the valve at the upstream end of the first compartment will be opened. The shock that is formed by this event propagates toward the model and may establish a quasi-steady flow over the model. The flow will be similar to the conventional flow within the range, but with augmented velocities (relative to the model) upstream of the model bow shock due to the passage of the valve-opening shock (these effects are ignored for evaluations of range flight behavior).

At valve opening time, a centered rarefaction wave propagates into the tube at sonic velocity, causing the affected flow within the tube to be accelerated toward the model. Subsequently, the model fully enters the tube to position x_p, causing the cessation of rearward flow over the model (since the model completely fills the tube cross section), and initiating a shock ahead of the model (shown at position x_s). Once this principal shock overtakes the previously established rarefaction wave, the gases ahead of the shock approach the model at model velocity (i.e., these gases are quiescent upstream of the shock). The principal shock establishes a motion of the tube gas in the same direction and approximately the same magnitude of velocity as the projectile. However, the boundary layer which is continuously initiated at the shock retards the motion of the tube gas near the wall, causing the gas at the wall to move toward the model at model velocity. The amount of gas affected by the boundary layer grows with time, both due to increasing separation of the principal shock from the model, and the time dependent growth of the boundary layer toward the tube centerline.

This boundary layer flow must be re-accelerated to model velocity as the model traverses the tube. Continuity requirements dictate flow forward on the model, and the mass of this reverse flow increases with boundary layer thickness ahead of the model.

Intermediate Times

Eventually, the boundary layer becomes fully developed behind the shock, at plane 3 indicated in the center sketch of Figure 4-4. The boundary layer developing region between the shock and plane 3 is designated as Region I. To the left of Region I is a region characterized by fully

EARLY TIMES

INTERMEDIATE TIMES

LATE TIMES (CLOSED TUBE ONLY)
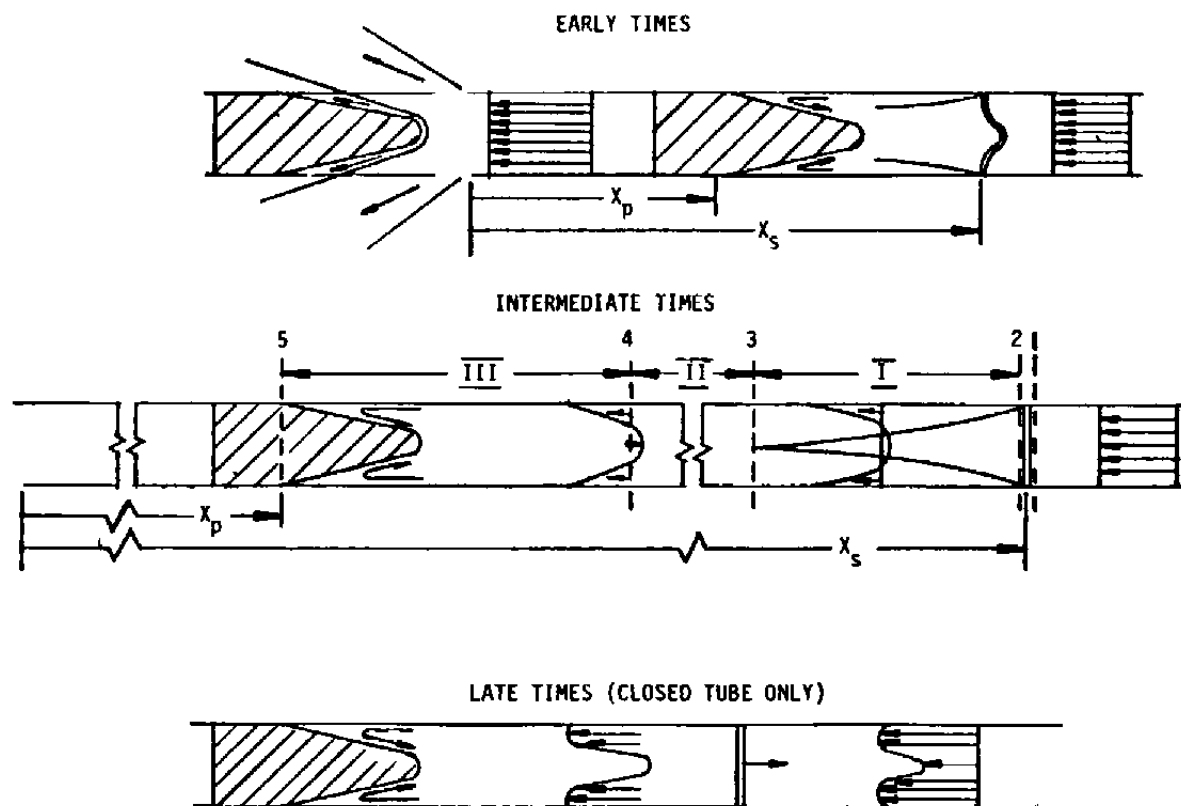
Figure 4-4. Temporal and spatial flow regimes within the tube.

developed viscous flow over the entire cross section, designated Region II. The extent of this region, once it is established, grows monotonically with time as the shock moves away from the projectile. Its boundary close to the projectile, plane 4, is defined as the closest plane to the model where the gas velocity distribution across the cross section is undisturbed by the proximity of the projectile. The final Region III between planes 4 and 5 is the model near flow field. This is characterized by rather extreme axial and radial velocity variations which are strongly influenced by the existence of the tube wall and model surfaces and their zero slip boundary conditions, and the nature of the flow emerging from Region II.

Late Times

Eventually, incident shocks which are created by the partitions or reflections off a closed end of a tube disrupt the flow described at intermediate times. The sketch on the bottom of Figure 4-4 represents the most severely disrupting case that would exist: within a closed tube (either by design, or by complete failure of a valve to open at the entrance to one of the compartments). The state shown in the sketch describes conditions after the incident shock has 1) reversed the flow (yielding the velocity profile shown on the right of the figure); 2) reflected off the model causing a momentary reversal of flow over the model; and 3) reversed the flow again due to the action of the shock reflected off the model, which is the shock shown in the sketch.

It is clear that a complete and accurate description of all of these details is well beyond the state-of-the-art of fluid mechanical predictive technology. Thus, the problem must be simplified in order to obtain a practical solution. Accordingly, certain evaluations employed in this study to achieve this end are described briefly in the following paragraphs.

It is worthwhile to evaluate the length of Region I during the intermediate time regime. The analysis of Reference 7 is employed to evaluate the growth of the boundary layer behind the shock. In this reference, a generalized integral momentum equation is written to include time dependent terms and moving wall boundary conditions. The details of the analysis will not be described here. However, the variation of momentum thickness (as defined therein) with distance away from a moving shock can be approximated by adopting a coordinate system attached to the shock, and assuming the flow is steady in that coordinate system (consistent with the analysis of Mirels, Reference 8). The coordinate transformation is shown in Figure 4-5, and the appropriate integral momentum equation is (Reference 7)*

_____

*This equation differs from that of Mirels which does not include all of the necessary terms.
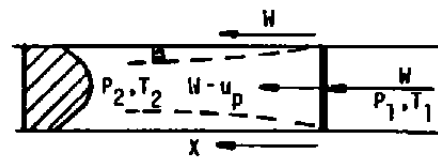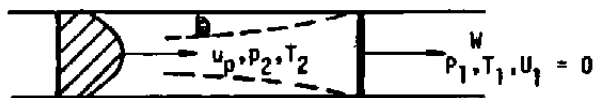
Figure 4-5. Coordinate transformation for boundary
layer analysis behind the shock.

$$\frac{d\theta}{dx} = \frac{u_p}{W_s G - u_p} \frac{C_f}{2} \tag{4-20}$$

The parameters θ, G, and $C_f/2$ are developed in Reference 7 through transformation of conventional relations applicable to 1/7 power turbulent velocity and stagnation temperature profiles. The solution to Equation 4-20 is

$$\frac{\theta}{x} = \frac{0.037}{\left(\frac{u_p x}{\nu}\right)^{1/5} \left(G - \frac{u_p}{W_s}\right)^{4/5}} \frac{\left(\frac{u_p}{W_s}\right)^{2/5}}{} \tag{4-21}$$

Evaluating Equation 4-21 out to the distance away from the shock where the boundary layer thickness equals 1/2 of the tube diameter, the length of Region I is defined:

$$\frac{\Delta x_I}{d} = 0.81 \left(\frac{u_p d}{\nu}\right)^{1/4} \tag{4-22}$$

for

$$G \approx 1.3, \frac{\theta}{\delta} \approx 0.09, \frac{u_p}{W_s} \approx \frac{2}{\gamma+1} \ (= .75 \text{ for helium})$$

Evaluation of Equation 4-22 for a gas particle velocity (u_p) of 20,000 feet per second, helium shocked to 500 atms, and an 8 inch diameter tube yields a length of Region I equal to about 40 diameters. Assuming that the intermediate time regime is established at the inception of Region II (i.e., the distance between the shock and the body consists only of the boundary layer development region and the near field region which is assumed to be 10 diameters), the projectile traversal distance at the inception of the intermediate time regime is:

$$\frac{x_{po}}{d} = \frac{\sum\limits_{I}^{III} \frac{\Delta x}{d}}{\frac{W_s}{U_p} - 1} = 150 \tag{4-23}$$

for

$$\frac{\Delta x_I}{d} = 40, \frac{\Delta x_{II}}{d} = 0, \frac{\Delta x_{III}}{d} = 10, \frac{U_p}{W_s} = 0.75$$

56

The corresponding flow establishment time (span of early time behavior) becomes:

$$t_o = \frac{x_{po}}{d} \frac{d}{\bar{U}_{xp}} = 5.7 \text{ msec} \qquad (4\text{-}24)$$

for

$$\frac{x_{po}}{d} = 150, \ d = 8", \ U_{po} = 18.3 \text{ kfps}, \ a = 10^4 g's$$

The flow establishment time is small compared to the model deceleration time (Figure 4-3, $\Delta t \approx 60$ msec). Also, the amount of gas which undergoes flow reversal over the model is maximum when the boundary layer is fully developed (t_o and later). Consequently, it appears conservative to ignore the details of the flow during early times in favor of using results which are applicable to intermediate times.

Certain non-varying elements exist during intermediate times. For example:

● The gas along the tube wall always approaches the model at model velocity

● The length of the near field region is probably invariant with time

● The velocity profile emerging from Region II can be characterized as that resulting from fully developed turbulent viscous flow

● The lengths of Regions I and II are not important during intermediate times

Thus, it seems reasonable to presume that during intermediate times the model convective environment is quasi-steady in a coordinate system which moves with the projectile. This is the model employed herein.

Flows during late times can be complex in the extreme. However, it is believed that none of the incident shocks which are formed are so strong as to cause complete reversals of gas flow direction, as would happen if the incident shock were formed by virtue of a reflection off a closed end. Thus, it is probable that the disturbances of gas velocity profiles emerging from Region II are not great due to the incident shocks, although gas density disturbances will be significant. Accordingly, it is convenient to presume that late time flows over the model can also be reasonably represented by using results of an analysis of the intermediate time flow field behavior which is described in the next subsection.

4.2.2 Evolution of the Flow Field Near the Model

4.2.2.1 Quasi-Viscous Near Field Evaluation

In spite of the significant reductions of problem complexity suggested above, the flow behavior near the model cannot be accurately characterized employing available computational procedures. What is needed is a complete solution of the Navier-Stokes equations employing satisfactory representations of the turbulent eddy viscosity and conductivity relations*. Lacking adequate procedures for solving the full Navier-Stokes equations, an estimate of the near field flow was made by solving the inviscid and viscous solutions decoupled. The rationale for this approach is that near the body the pressure field is probably dominated by inertial forces, and the inviscid solution is used to obtain a solution for the surface pressures. The pressures are then used as input to an approximate boundary layer solution to estimate the model heat transfer rates.

What is needed is the inviscid solution to the flow field sketched in Figure 4-6a in which the flow across plane BC is known. There were no known existing procedures for solving such inviscid flows, but the flow field is quite similar to that of a supersonic blunt body, Figure 4-6b. Therefore, the solution of the recovery tube inviscid flow field was obtained by modification to a computer code developed for solving the blunt body problem.

The code which was modified is a derivative (Reference 11) of the work of Moretti and Abbett in which the steady state blunt body flow field is obtained as the time asymptotic solution of a transient flow. The transient solution stabilizes to the correct steady solution because appropriate steady state boundary conditions are imposed on the transient solution. For the blunt body problem, these are the specified steady free stream flow variables. For the recovery tube problem, they are the inflow conditions along CE and the pressure across BC, Figure 4-6a.

To apply the blunt body code to the recovery tube problem required modifying the calculations along the entrance boundary, B'C', and the outflow boundary, C'D', Figure 4-6b. The latter calculation was replaced by a calculation for a fixed, impermeable wall. The wall pressure was calculated using a quasi-one-dimensional method of characteristics calculation (c.f. Moretti and Abbett, Reference 12).

Modifications to the inflow boundary calculation (B'C', Figure 4-6b) were somewhat more complex and follow the procedure developed by Abbett (Reference 13). Basically, along CE the entrance

---

*Attempts under this program to apply the laminar solution methodology of Reference 9 to this problem presented major difficulties. Although solutions are believed possible using an adaptation of an existing tube flow code (Reference 10) the requisite development effort was deemed beyond the project scope.

a) Inviscid flow field in recovery tube

b) Supersonic blunt body flow field.
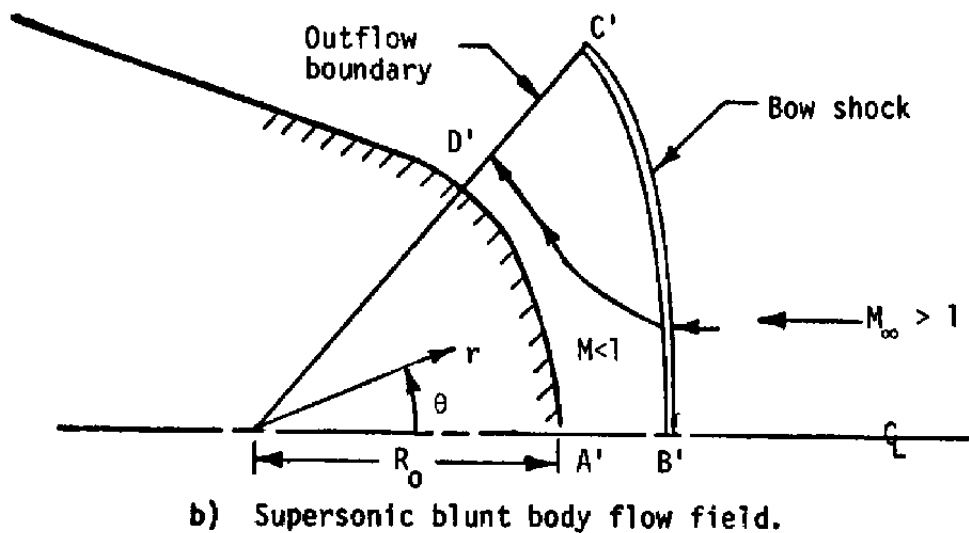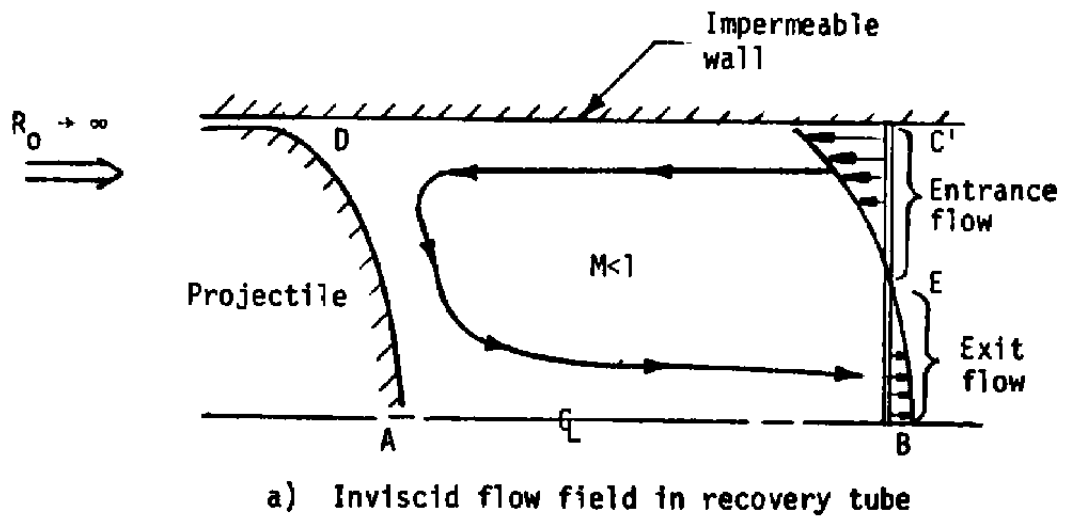
Figure 4-6. Schematic of inviscid flow field solution procedure.

flow is specified and the Rankine-Hugoniot shock jump conditions appropriate to the blunt body prob-
lem are replaced with the condition that during the transient solution only positive or zero entropy
changes are permissible across the entrance flow boundary. (Details of this entrance flow modeling
are given in Reference 13).

The inflow velocity and temperature profiles are derived through the assumption of adiabatic
flow and 1/7 power velocity profile, and by requiring the exit flow in Figure 4-6 to equal the inflow,
as required by the assumption of steady state

$$u_{c'-E} = u_p \left[1 - A \left(1 - \frac{r}{R} \right)^{1/7} \right] \text{where } A = A \left(u_p, T_1, \gamma \right) \qquad (4-25)$$

$$T_{c'-E} = T_2 + \frac{u}{C_p} \left(u_p - \frac{u}{2} \right) \qquad (4-26)$$

It can be seen from Equation 4-25 that the flow at the centerline of the upstream boundary is
away from the model. Consequently, the gas velocity on an absolute scale exceeds the model velocity
somewhat, as a direct consequence of the viscous action upstream of the model. Pressure is specified
as being uniform across the upstream boundary. Gas velocities and temperatures within the exit flow
zone are actually computed by the code.

A brief comment on coordinate systems is in order. The blunt body code utilizes a spherical
polar coordinate system (Figure 4-6b) while the tube wall and centerline are exactly parallel. In
making calculations for the recovery tube, the origin of the spherical polar coordinate system was
selected so that the angle between the tube wall and centerline in the computational model was equal
to 0.04 degrees.

Typical results from the calculation are shown in Figure 4-7. Several noteable features of
the solution include:

- Calculated velocities in the exit flow agree almost exactly with those computed from the
  application of Equation 4-25 to the exit flow region. This is quite satisfying in view
  of the elliptic nature of the flow and the features noted below

- Temperatures (and densities) do not agree with those inferred from Equation 4-26, and can-
  not without considering diffusion effects (which are ignored, by definition, in an invis-
  cid analysis)
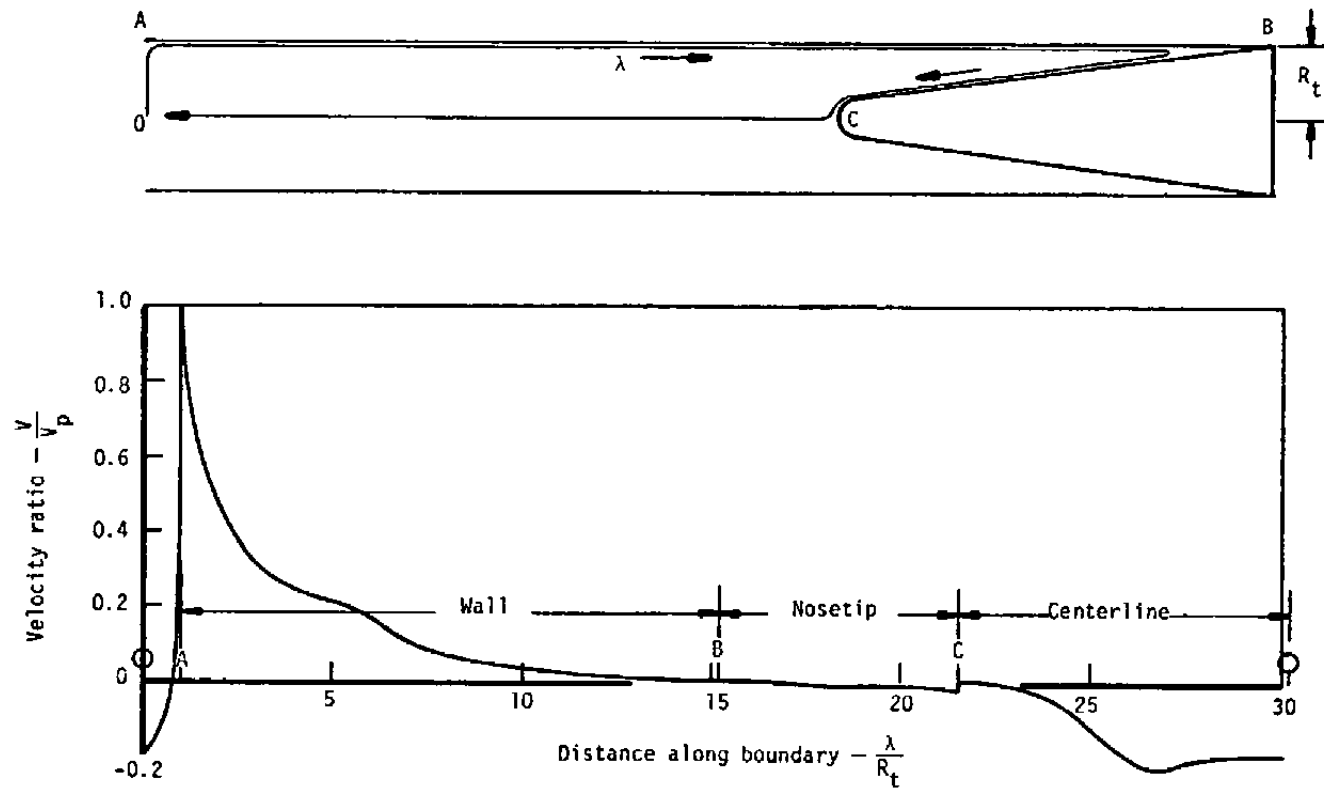
Figure 4-7. Typical results, inviscid near field analysis.

- The model causes a rapid decay of velocity along the wall, once the zero slip boundary condition is relaxed (as required by the inviscid assumption)

- Inviscid gas velocities along the body are only a small fraction of the upstream wall velocity (projectile velocity), due largely to the requirement that the flow stagnate both at the juncture of the model and the tube, and at the model "stagnation" point. (Velocities along the surface of the model are presented in expanded form in Figure 4-11).

In spite of the simplifications and shortcomings of the analysis, it is believed that the velocity results are reasonable.

Referring now to Equation 4-26, it can be seen that in adiabatic flow the peak temperature is at the wall, a necessary result of energy conservation in response to viscous shear at the wall. The gas will adhere to the wall at high temperature and be raised to an even higher temperature when it is transferred to the projectile, by virtue of the wall gas kinetic energy relative to the model. Thus, the maximum recovery temperature the model sees is

$$T_R = T_2 + 2 \left(\frac{u_p^2}{2\ c_p} \right) \tag{4-27}$$

compared to T_2 if the gas behind the shock had not been required to adhere to the tube wall. Thus, viscous effects are not only responsible for gas flows along the model (creating a forced convection heating environment) but they are also responsible for creating high driving potentials for heat transfer.

Up to this point, it has been convenient to ignore model deceleration and other effects insofar as they give reason to require a distinction between particle velocity behind the shock, and projectile velocity (both taken as u_p). However, these distinctions do exist and must be accounted for to evaluate recovery temperature. (It is assumed that these distinctions are not necessary relative to computed gas velocities over the model, providing they are scaled with projectile velocity as suggested by the format of Figure 4-7). The procedure for accounting for these effects is outlined in Figure 4-8 and described below.

- The principal shock compresses the gas to p_2, T_2, and u_2 at a position x along the tube, at a time t'

- The gas is immediately stagnated at the tube wall where it attains a stagnation temperature, $T_{t_2}(t')$

model

shock

$$p_p(t), \; T_{t_2}(t')\left(\frac{p_p(t)}{p_2(t')}\right)^{\frac{\gamma-1}{\gamma}} + \frac{u_p^2(t)}{2c_p} = T_r(t)$$

$$p_2(t'), \; T_2(t') + \frac{u_2^2(t')}{2c_p} = T_{t_2}(t')$$

$$p_1, \; T_1, \; u_1 = 0$$

t

t'

$X \longrightarrow$
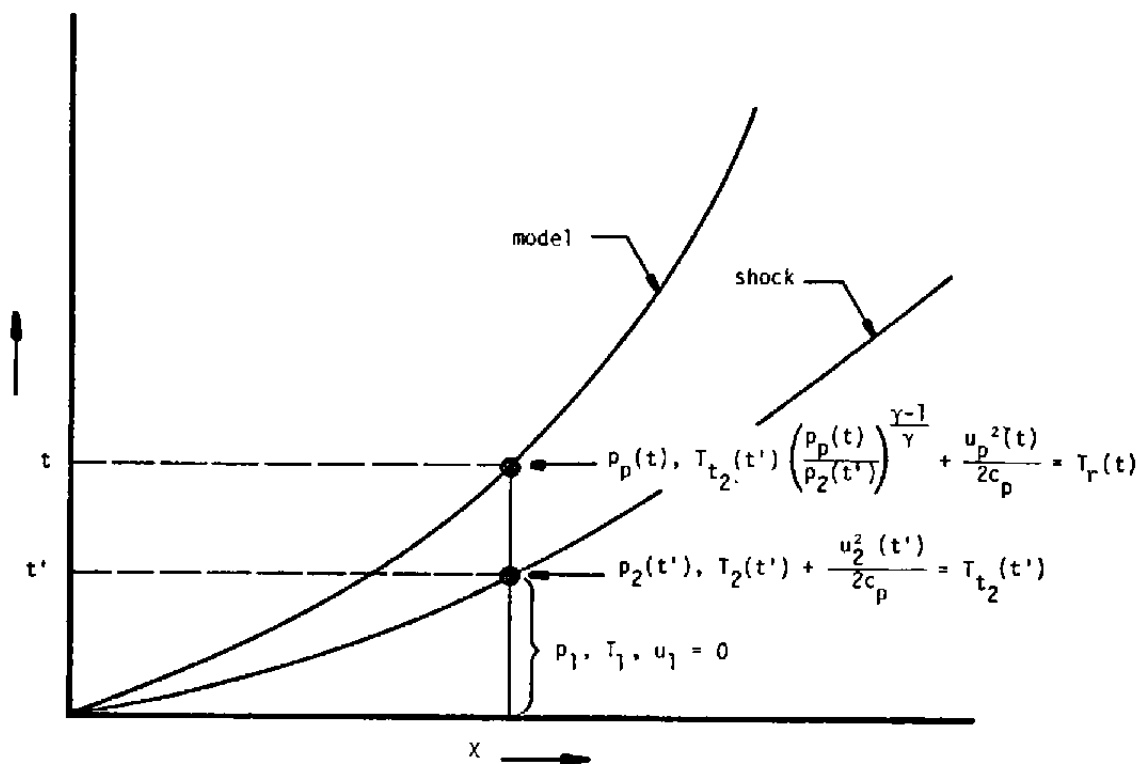
Figure 4-8. Recovery temperature evaluation procedure.

● The gas stays on the wall, and is subjected to pressure changes due to wave actions within the tube. Consequently, the gas temperature changes, isentropically by assumption.

● Finally, the model passes over the position x at time t, where the wall gas temperature at the pressure acting on the model face is augmented by the kinetic energy of the wall gas relative to the model $(u_p^2/2C_p)$

In this way, the unfavorable recovery temperatures at early times during the recovery are offset somewhat by favorably low temperatures in the later phases of model motion. The maximum computed recovery temperatures are certainly conservatively high, due both to heat transfer to the tube wall and to the vanishingly thin layer of gas that goes through these extreme processes.

When required, real gas temperatures have been estimated by evaluating Mollier chart data at the ideal gas enthalpy $(C_p T)$ and the local pressure.

4.2.2.2   Experimental Flow Visualization of the Near Field

Since the hypothesized flow is so unconventional, it was decided that an experimental verification of the theorized features of the flow was worthwhile. Thus, a simple experiment was devised as shown in Figure 4-9. In this experiment, polypropylene particles were suspended in a neutrally bouyant solution of water and alcohol for flow visualization purposes. The model was held stationary, and the tube was moved relative to the model to simulate the motion of a model within a recovery tube. The analysis of Reference 7 provides techniques for evaluating the non-steady boundary layer development within the tube, subject to impulsive tube motion at constant velocity.

The appropriate integral momentum equation for these conditions is:

$$\frac{d\theta}{dt} = k_1(m) \frac{u_w}{G}\left(\frac{u_w\theta}{\nu}\right)^{-\frac{m}{1-m}} \tag{4-28}$$

where m is equal to 0.5 and 0.2 for laminar and turbulent flow, respectively, and $k_1(m)$ is a constant which depends primarily on m and secondarily on the flow boundary conditions. The solution of Equation 4-28 is of the form

$$\frac{\delta}{u_w t} = k_2(m)\left(\frac{u_w^2 t}{\nu}\right)^{-m} \tag{4-29}$$
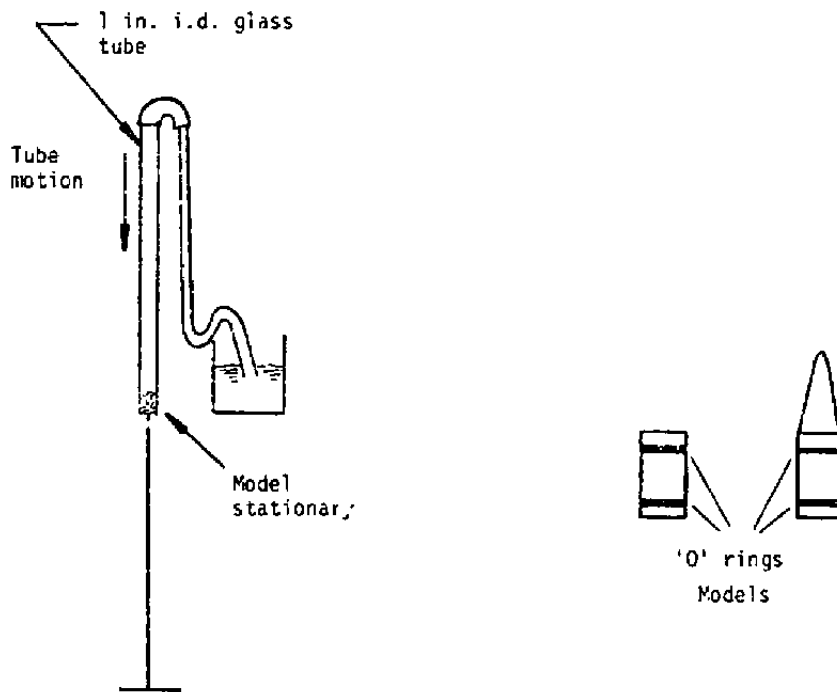
Figure 4-9.   Experimental flow visualization.

where $k_2(m)$ contains appropriate values of G, δ/θ, etc. Equation 4-29 assumes the boundary layer is either all laminar or all turbulent. Actually, the boundary layer would start out laminar and become turbulent at some critical Reynolds number on momentum thickness. This latter parameter grows in laminar flow as follows:

$$Re_\theta = k_3 \left(\frac{u_w^2 t}{\nu} \right)^{1/2} \tag{4-30}$$

Finally, the boundary layer would develop to the tube centerline ($\delta/d = 0.5$) to obtain fully developed viscous flow. The time required for this to happen can be estimated from Equation 4-29.

$$\frac{u_w^2 t}{\nu} = \left(\frac{u_w d}{2 k_2(m)\nu} \right)^{\frac{1}{1-m}} \tag{4-31}$$

Equations 4-30 and 4-31 have been evaluated for a 1 inch diameter tube filled with water, yielding the following results:

● Fully developed laminar flow in the tube for

$$t > \frac{1}{\nu} \left(\frac{d}{6.2} \right)^2 = 16.6 \text{ sec}, \quad u < 2400 \frac{\nu}{d} = 0.31 \text{ ft/sec} \tag{4-32}$$

● Transitional flow in the developing tube boundary layer for:

$$\frac{u't}{\nu} \sim 1.4 \times 10^5 \text{ (based on } Re_{\theta_{trans}} = 200) \tag{4-33}$$

● For large $\frac{u^2 t}{\nu}$ (large u^2), fully developed turbulent flow in the tube for:

$$t > 2.5 \frac{d}{u} \left(\frac{ud}{\nu} \right)^{1/4} < 1.0 \text{ sec for } u > 2.4 \text{ ft/sec} \tag{4-34}$$

From the above relations, it was determined that a 5 foot long tube was sufficient to provide either fully developed laminar or turbulent flow within the tube subsequent to an impulsive start of motion. However, a tube velocity of approximately 1000 feet per second is required to simulate recovery tube Reynolds numbers, which was not feasible. In addition, Mach number is not simulated with the scheme.

Experiments were conducted with a glass tube 5 feet in length. Photos of the flow behavior are presented in Figure 4-10 for both a flat piston, and a sphere-cone model. The flat piston results show flow generally as expected, i.e., particles follow the tube motion and reverse flow direction near the model. The flat piston results in Figure 4-10a show a region near the center of the model which is devoid of particles. This was presumed to be as a result of separation of the boundary layer which forms along the model surface. This postulate was verified with the sphere/cone model where a tip vortex is noted (left hand side of Figure 4-10b).

4.2.3 Model Boundary Layer Analysis

4.2.3.1 Attached Flow Convective Transfer Coefficients

For this study, the boundary layer heat and mass transfer coefficients have been assumed to be equal. In the attached flow regions along the model, they have been evaluated employing the integral energy boundary layer solution methodology described in Appendix A of Reference 14.

The configuration being analyzed is as shown in the following sketch.
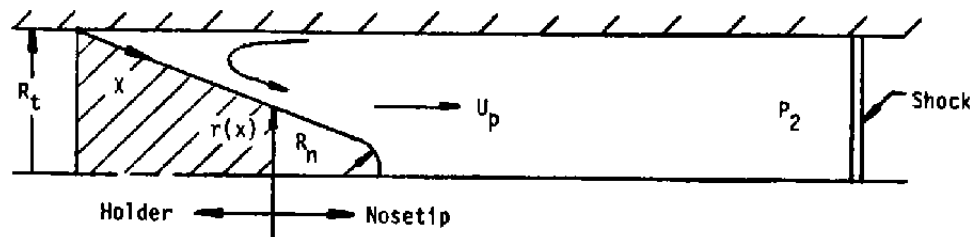
The boundary layer energy equation is:

$$\frac{d\phi}{dx} + \frac{\phi}{r\rho_e u_e} \frac{d(r\rho_e u_e)}{dx} + \frac{\phi}{(h_r - h_w)} \frac{d(h_r - h_w)}{dx} = C_H \frac{\rho'}{\rho_e} \tag{4-35}$$

where ϕ is the boundary layer enthalpy thickness and C_H is the Stanton Number, which for turbulent flow is taken as

$$C_H = \left[0.0309/Pr^{2/3} \; (\rho_e u_e \phi/u')^{1/5} \right]^{5/4} \tag{4-36}$$

The solution of Equation 4-35 is presented in Equation 4-37, under the assumption of $\phi \simeq 0$ at the tube/model juncture (the origin of the boundary layer integration), and employing the following simplifications:
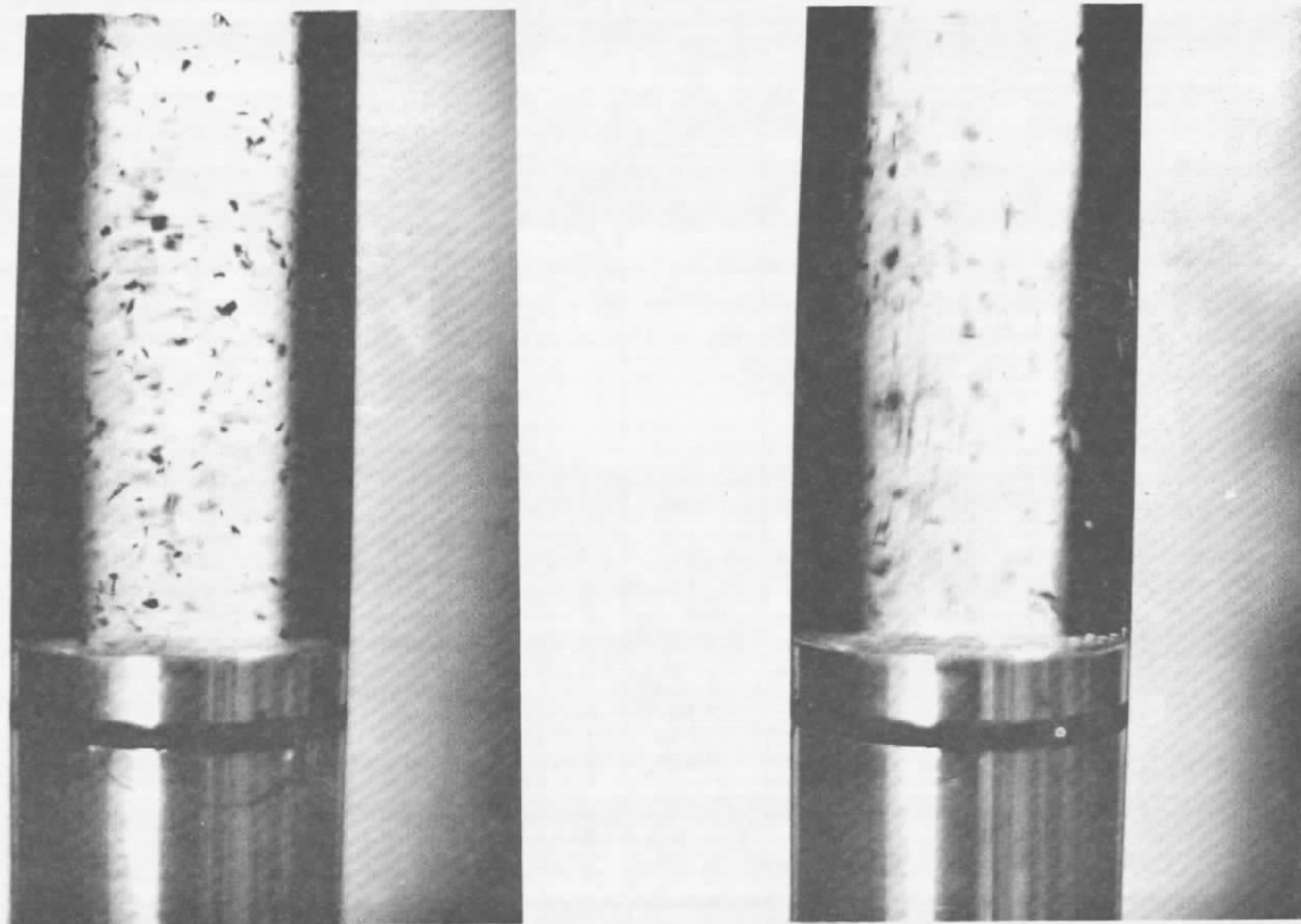
a.   Flat piston.

Figure 4-10.   Experimental flow visualization.
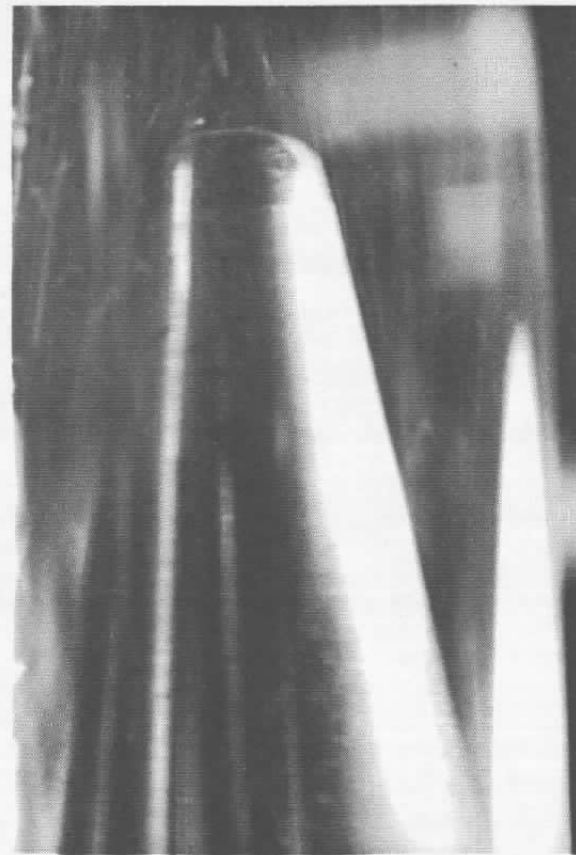
Tip vortex   Typical behavior

b. Sphere/cone model.

Figure 4-10. Concluded

$$\rho' = \rho_e; \ \mu' = \mu_e; \ Pr = 1; \ h_r - h_w = constant$$

$$\phi = \frac{0.037}{r\rho_e u_e} \left[\int_0^x \frac{(r\rho_e u_e)^{5/4}}{\left(\frac{\rho_e u_e}{\mu_e}\right)^{1/4}} \, dx \right]^{4/5} \tag{4-37}$$

Equation 4-37 has been evaluated for the computed inviscid velocities along the model; for densities evaluated at the recovery temperature and model face pressure; and for viscosities evaluated at the recovery temperature. The inviscid velocities and non-dimensional heat transfer coefficients are presented in Figures 4-11a and 4-11b, respectively.

Since the model cone angle was held constant for all tube diameters considered, the results in Figure 4-11 apply to all tube diameters up to the point of flow separation near the model stagnation point. Furthermore, the heat transfer coefficient results are applied at all times during the model deceleration phase; for all model velocities, recovery temperatures, and model face pressures. The locations of the holder/nosetip interface and boundary layer separation point shift on the figures for tube diameters different from 8 inches.

The boundary layer separation point is defined as that experimentally observed on the base of spheres — 108 degrees from the sphere stagnation point which is 72 degrees around the spherical nosetip from the model stagnation point.

4.2.3.2   Convection in the Separated Region Near the Model Stagnation Point

The flow along the model is not only highly unconventional, but boundary layer separation must occur near the model stagnation point for the same reasons that flow separates in the base region of a sphere. Since heat and mass transfer in turbulent separated regions cannot currently be calculated accurately from first principles, and since no directly applicable data exists for a high speed model in a recovery tube, available heat and mass transfer data behind spheres were evaluated and modified to suitable form for this problem.

A fairly large body of data relating to convection in the bases of spheres has been correlated in Reference 28. Considerations were given to the effects of freestream turbulence, and under conditions of subcritical (laminar) and supercritical flows (laminar like attached flow, turbulent flow in the separated region and the wake). The basic correlation is of the following form:

$$F_s = A \left(\frac{v_\infty}{v_1} \right)^{0.16} + \left[B\alpha_t(\alpha_t + C) + D \right] Re_\infty^{1/2} \ Pr^{1/6} \tag{4-38}$$

70

Figure 4-11. Model boundary layer analysis results.

where the Frössling number, Fs is

$$Fs \equiv \frac{Nu-2}{Re_\infty^{1/2} \, Pr^{1/3}} \tag{4-39}$$

and

Nu = Nusselt Number

ν_i = kinematic viscosity at the sphere surface

$$Re_\infty = \frac{u_\infty d}{\nu_\infty}$$

α_t = apparent level of freestream turbulence, $\frac{\sqrt{\bar{u}'^2}}{u_\infty}$

∞ = freestream conditions upstream of the sphere

The coefficients A, B, C, and D are tabulated functions of angle around the sphere, and depend upon whether the flow is subcritical or supercritical. For supercritical flows, the contributions of the B and C terms can be ignored.

The correlation was modified herein in order to base the results on conditons at the point of separation (which can be computed for spheres and for the model in the recovery tube) rather than the freestream conditions which only make sense for the sphere. The BLIMP boundary layer code (Reference 15) was used to evaluate the laminar momentum thickness Reynolds numbers at the point of separation for a sphere immersed in an infinite stream, using as input the potential flow velocity distribution around a sphere

$$\frac{u_e}{u_\infty} = \frac{3 \sin \alpha}{2}, \alpha \text{ measured from the forward stagnation point} \tag{4-40}$$

The BLIMP output was correlated with the relation:

$$Re_{\theta,s} = 0.581 \, Re_\infty^{1/2} \tag{4-41}$$

The heat transfer coefficient based on properties at separation can be evaluated with the aid of equations 4-38 and 4-41, the assumption of unity Prandtl number, and the fact that Nu >> 2 for supercritical flow:

$$H \equiv \rho_s u_s C_{H's} = \left(\frac{.406}{Re_{\theta,s}} A + 0.7D \right) \rho_s u_s \qquad (4-42)$$

TABLE 4-2.   COEFFICIENTS OF EQUATION (4-42)

Body Angle (Degrees)	A	$D \times 10^4$
113.6	0.84	9.0
126.9	1.34	13.8
143.1	1.10	5.5
180. (stag.pt.)	0.1	37.4

The appropriate coefficients A and D from Reference 28 are tabulated in Table 4-2. The Stanton Numbers based on separation point properties are presented in Figure 4-12, based on linear variations of the coefficients with cosα and the data of Table 4-2.

In order to evaluate the momentum thickness Reynolds number at separation, $Re_{\theta,s}$, it has been approximated as equal to the enthalpy thickness Reynolds numbers evaluated from the attached flow heat transfer analysis of the previous subsection. This assumption together with the data at the separation point in Figure 4-11 yields:

$$Re_{\theta,s} \approx .0056 \left(\frac{\rho_e u_p R_t}{\nu_e} \right)^{0.8} \qquad (4-43)$$

which is equal to approximately 1000 for the representative data presented in Figure 4-11.

It is noteable that:

• Stagnation point (180 degree) Stanton Numbers in Figure 4-12 are approximately independent of the Reynolds numbers at separation

• Stanton Numbers are on the order of those expected in turbulent flow ($1-3 \times 10^{-3}$)

• Separated region heat transfer coefficients at a given position on the nose are approximately proportional to the boundary layer edge mass flux at the point of separation.
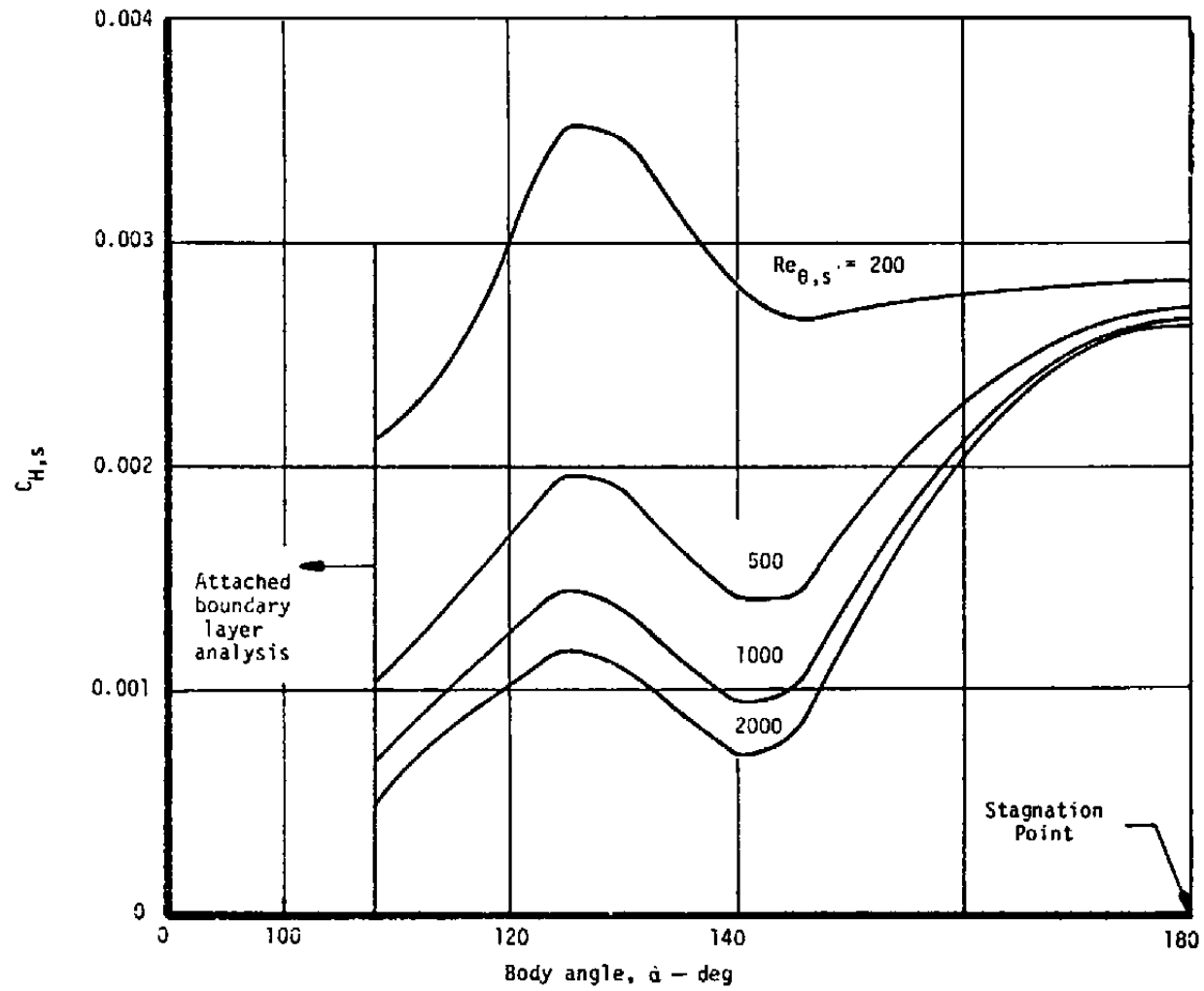
Figure 4-12.   Separated flow heat transfer Stanton number.

● The heat transfer behavior on the nosetip during the recovery process is dominated by turbulent, viscous phenomena which are complex in the extreme and subject to a good deal of uncertainty.

4.3   RADIATIVE HEATING TO MODEL

Radiative heat transfer from the shock layer to the model surface may be significant depending upon the type of gas and its thermodynamic state. The predictions of the radiative fluxes are usually quite complex. For any quantitative prediction, a knowledge of the frequency dependent radiative properties of the participating species, the gas temperature, and the species composition is required.

The spectral adsorption coefficient is the frequency dependent radiative property which is used in calculating the radiation transport. These coefficients are made up of contributions from the allowed radiative transitions associated with the constituent species of the gas mixture. The continuum contributions to the absorption coefficient include transitions associated with atomic photoionization, photodetatchment, molecular photoionization and photo-dissociation. The atomic line transitions and the molecular band systems are also usually important.

The analytical model used to calculate the spectral absorption coefficients of high temperature gas mixtures in local thermodynamic equilibrium is described in detail in Reference 16. The model accurately accounts for both the atomic and ionic line and continuum transitions for the gas mixture. The above properties are used in a transport model to compute the radiative heat fluxes or intensities along a line of sight or in a plane-parallel slab. The transport model employed solves the equation of (radiative) transfer using a tangent slab approximation. This approach enables a convenient formulation of the solution to the equation of transfer. The calculational procedure outlined in Reference 16 has been automated and has been extensively used in computing the radiative heat fluxes associated with probes entering the various planetary atmospheres at high velocities. The detailed spectral absorption coefficients, intensities, and fluxes for a given temperature, pressure, path length, and gas mixture composition are obtainable from the RAD/EQUIL/1973 code (Reference 17).

Radiation calculations were performed for the two conditions summarized in Table 4-3.

TABLE 4-3. SUMMARY OF RADIATION CALCULATION RESULTS

Gas	Gas Temperature (°R)	Pressure (atm)	Path Length (in)	Radiation to Model (Btu/ft² sec)
Helium	20,000	445	2.0	77
Air	25,000	445	2.0	≈ 20,000[a]
[a]This can be considered as only an upper limit estimate.				

These calculations represent upper limit estimations for the maximum radiative model heating rate in cases where the recovery tube gas is helium or air, respectively. The calculations are extremely conservative because:

● The upper limit recovery temperatures calculated using the technique described in Section 4.2.2.1 were used. (In reality, recovery temperature would be lower due to heat transfer to the tube wall and the vanishingly thin layer of gas that goes through these processes.)

● A conservatively long estimate for path length was used, and it was assumed to be isothermal at the recovery temperature.

● The initial value of recovery temperature was used. This is the maximum value and it drops rapidly with time.

As Table 4-3 indicates, even with the extremely conservative nature of the calculation, radiative heating in helium gas represents no problem. (It is small compared to the convective flux). However radiation in the air case may be a problem, but the current calculation is too conservative to establish this.

To improve the radiative calculation for the air case would require a much more sophisticated modeling of the entire recovery tube flow field and tube heat transfer. Such a calculation is beyond the current state of the art of computational fluid mechanics, and the problem is probably best handeled experimentally.

Assuming that air would prove to be an impractical recovery tube gas the above radiation calculations do show that helium could be safely used. Because it is small, radiative model heating was neglected in the calculations that follow of model thermal response in helium filled recovery tubes.

4.4 MODEL HEAT CONDUCTION AND SURFACE ABLATION

The previous analyses described in Sections 4.1 through 4.3 provide input for the calculation of model heat conduction and surface ablation which are potential damage modes. This section

describes the technique used for evaluation of these phenomena as well as the sequence of events modeled and boundary conditions used.

4.4.1 Analysis Technique

The ablation and thermal response of the model was calculated using the surface energy balance and in-depth analysis portion of the ANAP (Aerotherm Nosetip Analysis Procedure) code (Reference 18. In this code the in-depth thermal response is coupled fully implicitly to the energy, mass, and species conservation relations at the model surface to predict ablation and heat soak. The sketch below illustrates the ablating surface control volume and the energy fluxes of interest. The surface energy balance
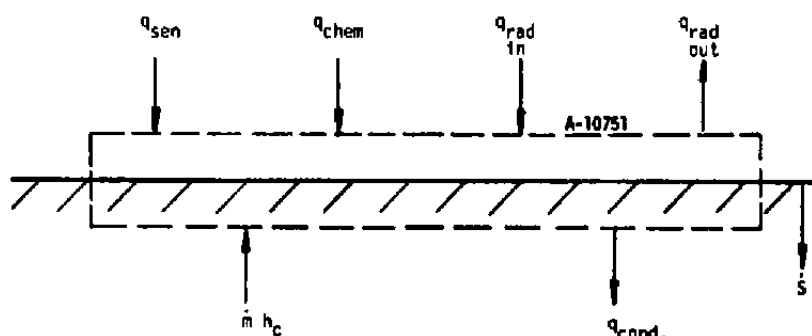
Sketch of Surface Energy Balance Control Volume
and Energy Flux Terms

equation employed is of the convective transfer coefficient type. The energy balance equation takes the following form:

$$\underbrace{\rho_e u_e C_H (H_r - h_{ew})}_{q_{sen}} + \underbrace{\rho_e u_e C_M \left[\sum (z_{ie}^* - z_{iw}^*) h_i \bigg|^{T_w} - B' h_w \right]}_{q_{chem}} - q_{cond} + \underbrace{\alpha_w q_{rad}}_{\substack{q_{rad} \\ in}} - \underbrace{F\sigma\varepsilon_w T_w^4}_{\substack{q_{rad} \\ out}} = 0 \qquad (4\text{-}44)$$

The usefulness of this formulation has been demonstrated by successful application to both data and "exact" solutions in simple heat or mass transfer problems, and in combined heat and mass transfer problems for unity (or near unity) Lewis number. Descriptions of the individual terms in the energy balance equation are as follows:

q_{sen} — represents the sensible convective heat flux.

q_{chem} — represents the net amount of chemical energy fluxes at the surface. The z^*-difference term represents transport of chemical energy associated with chemical reaction of the wall and in the boundary layer. The z^* terms are calculated parametrically by thermochemistry codes such as the ACE (Aerotherm Chemical Equilibrium) code, (Reference 19) using JANAF thermochemistry data. The $B'h_w$ term represents energy leaving the surface in gross motion (blowing) of the gas adjacent to the surface.

q_{cond} — is the heat conducted from the surface to the in-depth material. This flux is related to surface temperature and recession rate by the solution of the in-dept heat conduction equation which is solved numerically by an implicit/explicit finite difference procedure.

q_{rad} — is the incoming radiation .

$q_{rad_{out}}$ — is the outgoing radiation.

The indepth analysis portion of the ANAP code solves the transient two-dimensional heat conduction equation for an axisymmetric nosetip. It uses a dual orthogonal conduction grid technique to accurately model both the high temperature gradients near the surface and the shallow indepth gradients. Temperature dependent material properties are accounted for.

4.4.2 Sequence of Events Modeled

Because of the transient nature of the conduction problem the entire preheat, launch, flight, recovery and cool down sequence described in the introduction must be modeled in the thermal analysis. The specific boundary conditions for each of these events are described in the following paragraphs.

Preheat and Launch

Preheat was assumed to be accomplished by a uniform radiative heat flux of 700 Btu/ft²-sec for 6 seconds which brings the surface temperature to about 4500°R. These conditions are felt to be realistically achievable based on current technology, even though no specific hardware currently exists to accomplish this. Free convection under these conditions was calculated and found to be negligibly small. Thus, no significant ablation occurs during preheat. It was assumed that no material is lost during launch.

Range Flight

The range flight portion of the test sequence was modeled using the coupled shape change computational procedure employed in the basic ANAP code (Reference 18). In this procedure the bow shock shape and surface pressure distribution are calculated from correlations. These are then used as input to an integral boundary layer technique for calculation of heat and mass transfer coefficients. Transfer coefficients are used in the surface energy balance along with parametric thermochemistry solutions for graphite ablation in air to calculate ablation rate and surface temperature.

As far as the freestream environment is concerned it was assumed that constant pressure segments in the range could be made short enough to closely approximate reentry flight.

Recovery

Boundary conditions for the thermal response during recovery come from the analysis described in Sections 4.1 through 4.3. Specifically, boundary layer edge recovery temperature and pressure come from the shock/dynamic calculation described in Section 4.1. Heat and mass transfer coefficients (they are assumed equal) come from the model boundary layer analysis covered in Section 4.2. Radiative heating to the model (for recovery in a helium filled tube) was neglected as dictated by the radiation results of Section 4.3.

These input were used in the surface energy balance along with graphite ablation in helium parametric thermochemistry solutions to calculate ablation rate and surface temperature.

Cooldown

The cooldown portion of the test is similar to the preheat in that heat transfer occurs primarily by radiation. Again, this is due to the negligibly small size of the free convection term. And, as with preheat, no significant ablation occurs during cooldown.

4.5   STRUCTURAL RESPONSE

Nosetip structural failure under loads is a potential damage mode. Stresses which could cause structural damage to the model are induced by four types of loading:

- Indepth temperature gradients

- Surface pressure

- Inertial load

- Impulsive load

Time dependent indepth temperature gradients are produced by heat transfer in flight, recovery and cooldown. Surface pressure during recovery may reach levels many times those experienced in flight.

The inertia load is a dynamic load due to surface pressure. If the surface pressure is applied suddenly, an impulse effect may be produced, and stress waves will travel in the nosetip material. The stresses generated by these stress waves may be many times higher than that of a static loading case. However, an approximate calculation using the one dimensional stress wave equation indicates that the impulse effect is negligible for these conditions, since the natural period of vibration is much smaller than the duration of surface pressure change (10^{-5} seconds versus 10^{-3} seconds).

Structural calculations were performed with the Aerotherm DOASIS code (Deformation, Plastic, Orthotropic, Axisymmetric Solution of Inelastic Solutions, reference 20). It is a very general two-dimensional finite element program used predominantly to calculate the static nosetip response. It has the capability of analyzing the elastic-plastic behavior of an axisymmetric solid composed of multimodulus, orthotropic materials with temperature dependent properties. Arbitrary axisymmetric thermal, pressure, mechanical and body force loadings can be treated.

ATJ-S graphite was the nosetip material considered for the current analysis. The mechanical properties for this material are outlined in Table 4-4 (Reference 29). The across-grain direction is parallel to the z direction, and the with-grain direction is parallel to γ-θ planes. Both tension and compression properties are given in this table.

The analysis procedure for using the DOASIS code is as follows:

1. Finite element grids for the DOASIS code are generated by a preprocessing program MESHGN. The structural mesh is shown in Figure 4-13 along with the boundary conditions.

2. The external pressure loading and the deceleration rate were given from the dynamic analysis described earlier. The temperature distributions as function of time were received from the ANAP code. An interface code TNAP interpolates and translates the temperature field to the structural finite element mesh.

3. With this required information, the DOASIS code outputs stresses, strains and displacements of every finite element.

4. To assist the engineer in evaluating the large amount of data generated, a post-processing program, CONTUR, plots isostresses and isostrains.

Constant surface pressure

5"

Finite element grids

No radial shear

No axial displacement
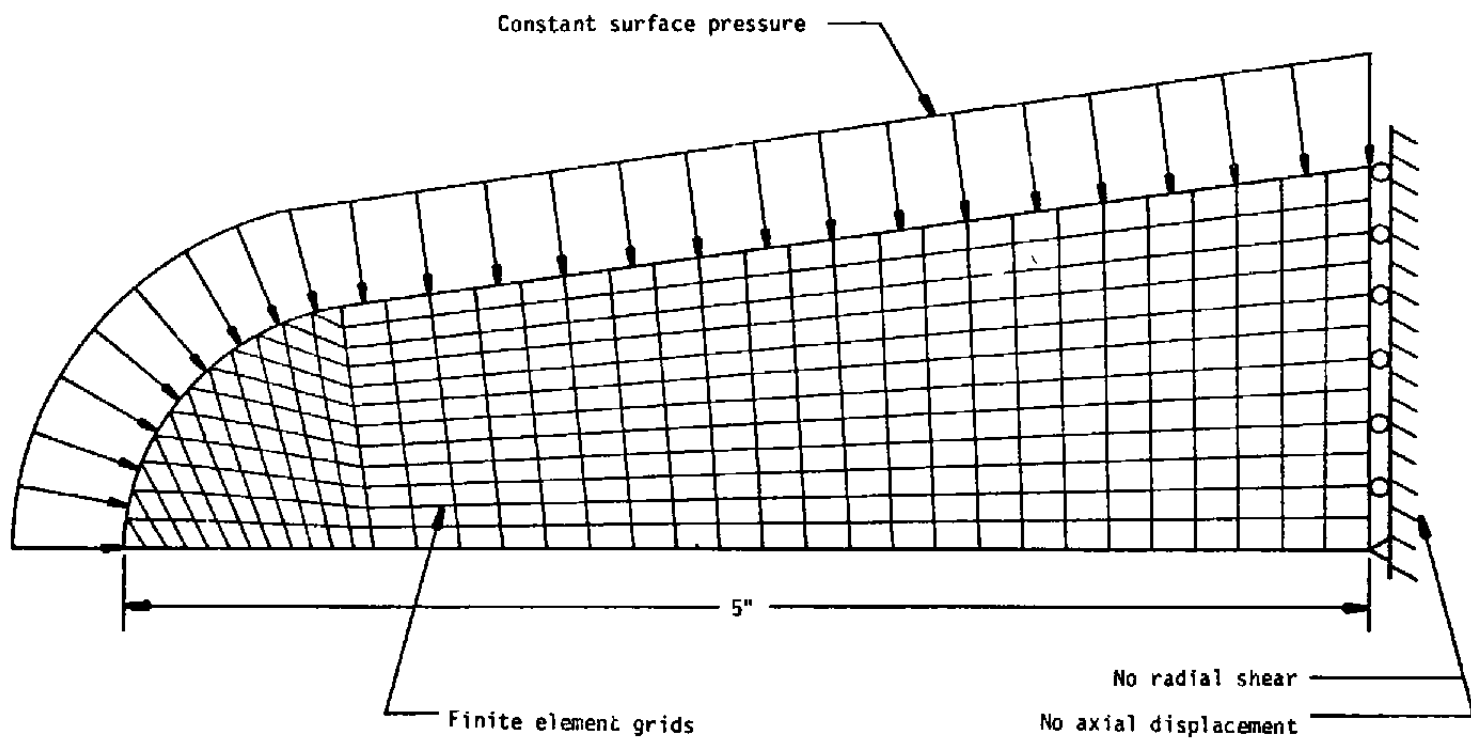
Figure 4-13. Geometry and boundary conditions for structural analysis.

TABLE 4-4. MECHANICAL PROPERTIES OF ATJ-S GRAPHITE

Temperature (°F)	Tension					Compression					G_{rz} (10⁶ psi)	$\alpha_r = \alpha_\theta$ (10⁶ in/in/°F)	α_z (10⁶ in/in/°F)
	$E_r = E_\theta$ (10⁶ psi)	E_z (10⁶ psi)	ν_{zr}	$z_{\theta r}$	$\nu_{\theta z}$	$E_r = E_\theta$ (10⁶ psi)	E_z (10⁶ psi)	ν_{zr}	$\nu_{\theta r}$	$\nu_{\theta z}$			
70	1.67	1.15	0.09	0.110	0.131	1.4	1.05	0.06525	0.065	0.087	0.5870	1.21	1.72
1000	1.70	1.17	0.097	0.120	0.141	1.5	1.10	0.07407	0.074	0.101	0.6032	1.57	2.13
2000	1.76	1.25	0.107	0.130	0.151	1.65	1.20	0.08218	0.082	0.113	0.6421	1.92	2.47
3000	1.91	1.39	0.116	0.140	0.159	1.95	1.40	0.08974	0.090	0.125	0.7235	2.19	2.73
4000	1.67	1.22	0.125	0.150	0.171	1.75	1.30	0.10029	0.10	0.135	0.6426	2.41	3.00
5000	0.75	0.62	0.162	0.177	0.196	1.15	0.9	0.20035	0.20	0.256	0.3503	2.69	3.38
5500	0.5	0.43	0.180	0.190	0.2	0.8	0.65	0.24944	0.25	0.307	0.2374	2.80	3.54
6000	0.34	0.32	0.188	0.194	0.2	0.6	0.56	0.31656	0.317	0.343	0.1779	2.92	3.68
6500	0.196	0.183	0.193	0.197	0.2	0.4	0.37	0.385	0.385	0.403	0.1070	2.99	3.76
7000	0.06	0.06	0.200	0.200	0.2	0.14	0.14	0.45	0.45	0.45	0.0358	2.77	3.49

4.6   SUMMARY OF MODELING TECHNIQUES

A summary flowchart showing the entire analysis procedure is given in Figure 4-14. This Figure indicates how the analyses described in this section feed one another and ultimately lead to output which can be used to assess model damage and aid in assessing system costs.

Results of model damage and system cost calculations using these procedures are covered in Sections 5 and 6 which follow.

Figure 4-14. Summary flowchart of analysis procedure.

SECTION 5
MODEL DAMAGE CALCULATION RESULTS

Results of a matrix of model damage calculations are presented in this section. The objective of this matrix of calculations is to establish the level (probability) of model damage for the most severe values of interest of key recovery tube parameters.
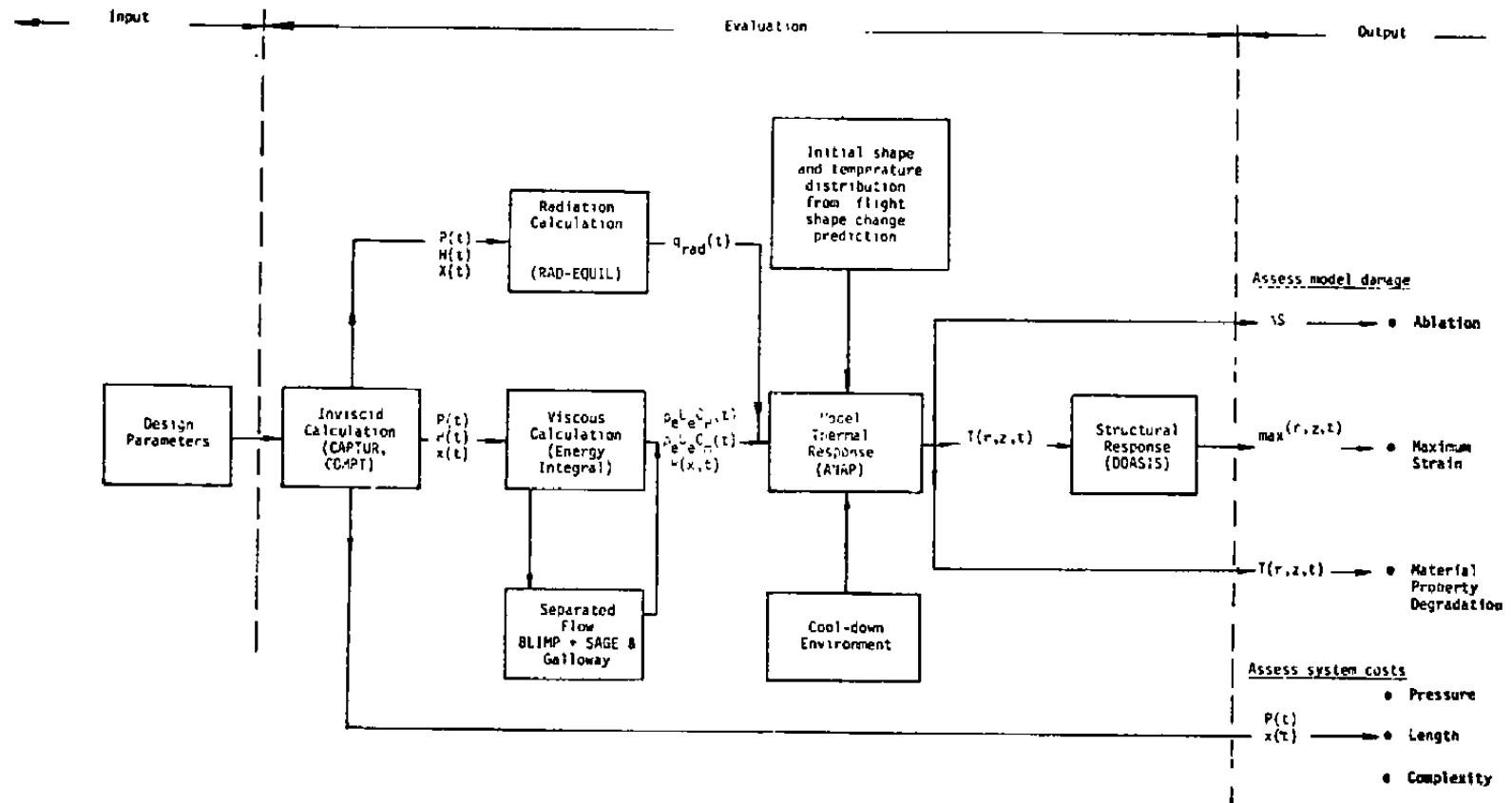
Section 5.1 presents the rationale for the matrix of recovery cases considered. Section 5.2 covers the thermal and ablation results and Section 5.3 discusses the structural results.

5.1 MATRIX OF RECOVERY CASES CONSIDERED

System sizing considerations presented in Section 2 indicate that tube diameter and projectile deceleration rate are two key parameters. Furthermore, analyses presented in Section 4 show that there is significant uncertainty in the calculation of the model convective heating which is a key quantity affecting model damage.

Therefore, the objective of the calculation matrix is to establish model damage for the most severe values of tube diameter, deceleration rate, and heating uncertainty. Table 5-1 presents the matrix of calculations performed to accomplish this objective. Case 1 of the matrix establishes the baseline response to which comparisons are made. Cases 2 and 3 are used to determine the effect of varying diameter and deceleration rate. Finally, in Case 4 the nominal heating rates calculated using the technique described in Section 4 are multiplied by a factor of 10. The objective of this calculation is to determine the effect of a gross error in the heating technique.

TABLE 5-1. MATRIX OF MODEL DAMAGE CALCULATIONS

Case No.	Tube Diameter (in)	Nominal Deceleration (10^3 g's)	Nominal Pressure (atm)	Heating Rate Multiplier	Comments
1	8	8	356	1x	Establish baseline
2	14		624		Largest diameter of interest
3		4	312		Effect of reduced acceleration and increased time
4		8	624	10x	Effect of increased heating

Specifications regarding model, range, and recovery tube configurations for the damage calcu-
lation matrix are presented in Table 5-2. The nominal projectile configuration is shown in the sketch
below.
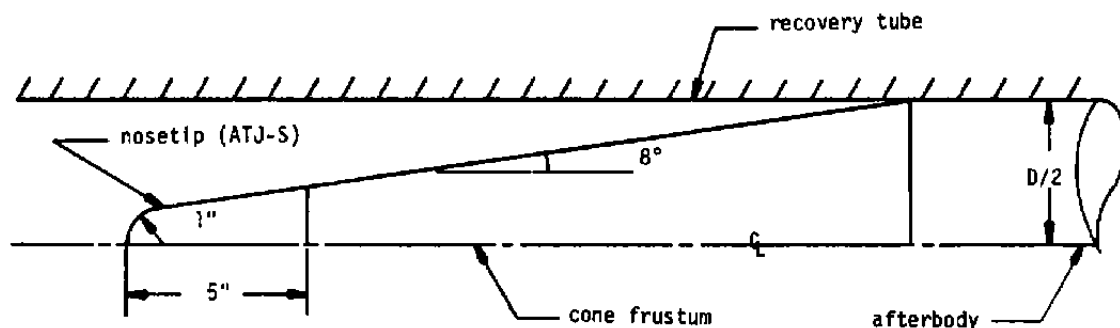
Sketch of projectile configuration.

Figure 5-1 shows a plot of the flight trajectory for which simulation was desired. It is a
nominal ICBM trajectory. A range simulation altitude interval of 40 to 50 kft was selected because
it is the highest altitude interval (and hence requires the greatest recovery velocity) which has
begun to experience any appreciable ablation.

Trajectory simulations for the two different tube diameters called out in the calculation
matrix are also shown in Figure 5-1. The 8-inch diameter (Case 1) results in a nominal ballistic co-
efficient (β) of 1000 psf (see Figure 2-2, Section 2). This β gives an adequate simulation of the
desired trajectory. The 14-inch diameter projectile (Cases 2, 3, and 4) yields a nominal β of 2870
psf. In order to make the damage calculation results of the two different diameters comparable, the
initial velocity for the 14-inch cases was selected such as to yield the same recovery velocity as
the 8-inch case.

5.2 THERMAL AND ABLATION RESULTS

The results of the thermal and ablation analysis are covered in this section. First the input
from the shock/dynamics and convective heating calculations which are required to perform the thermal
analysis are presented. Then the ablation and thermal analysis results are discussed.

5.2.1 Required Input

The input required from the shock/dynamic analysis are the model pressure and recovery tempera-
ture history. Model pressure history for Case 1 is shown in Figure 5-2. The peaks in the distribution
correspond to the valve/shock interactions discussed in Section 4.1. Pressure histories for Cases 2
and 4 have the same temporal distribution as Case 1 (since the specified deceleration rate is the same)

TABLE 5-2. SPECIFICATIONS FOR DAMAGE CALCULATION MATRIX

| Quantity	Specification	Comments
Model Configuration		
Nose radius	R_N = 1.0 inch	
Nosetip length	L = 5.0 inch	Typical R/V quantities
Cone half angle	θ_c = 8°	
Material	ATJ-S graphite	
Range Quantities		
Preheat	700 Btu/ft²-sec for 6 sec	Brings surface temperature to 4500°R
Preconditioning section	None considered	
Range length	20,000 ft	
Altitude interval in range	50 to 40 kft	Results in greatest recovery velocity of interest
Recovery Quantities		
Number of compartments	5	
Gas	Helium	Minimizes radiation to model
Entry velocity	18.36 kfps	Greatest recovery velocity of interest
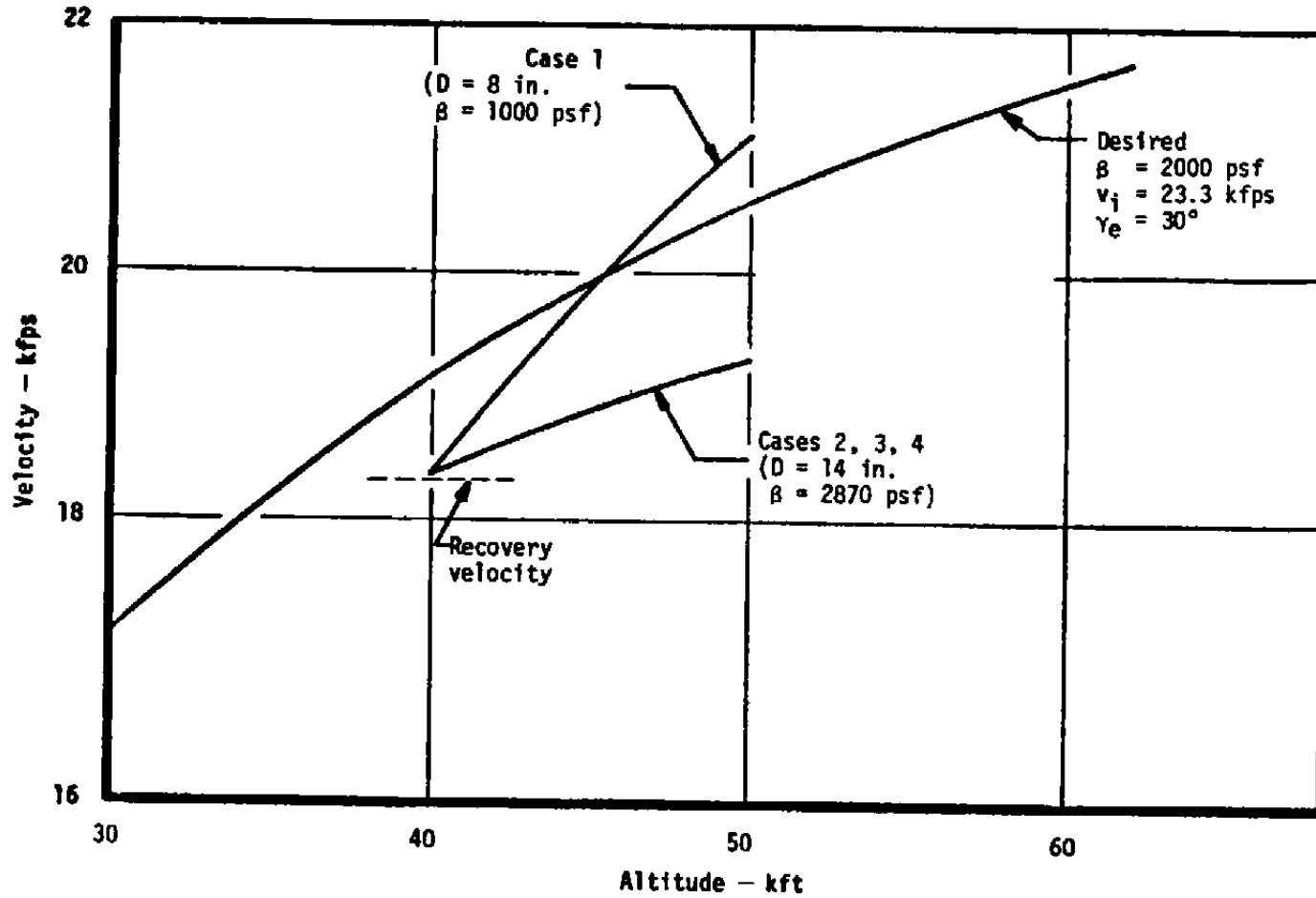
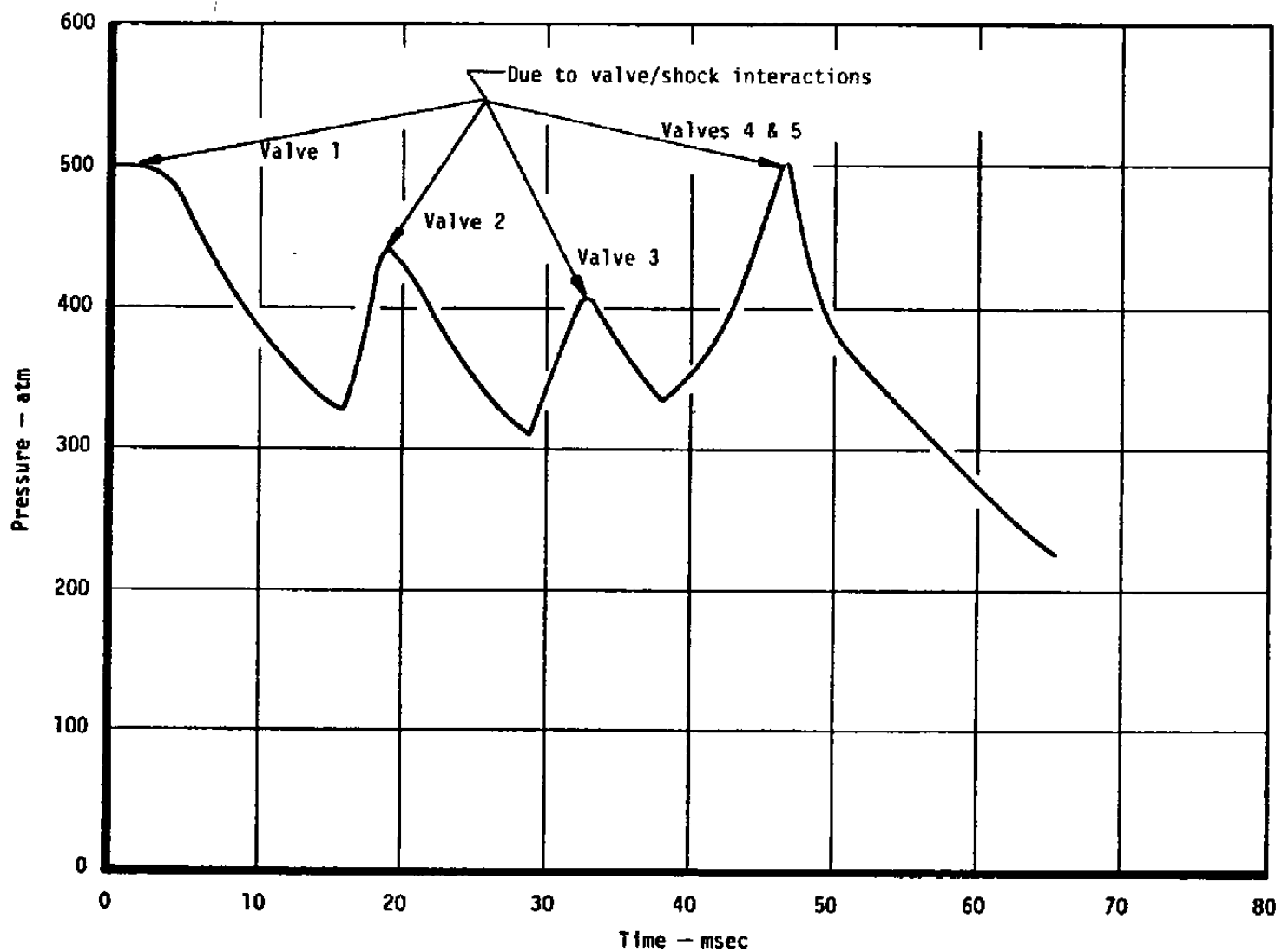Figure 5-1. Trajectory simulation for model damage calculations.

Figure 5-2. Model pressure history for Case 1.

but are scaled in value by the ratio of tube diameters. This is the result of the projectile mass per unit base area scaling discussed in Section 2. The pressure history for Case 3 is similar to Case 1 with time scaled inversely with deceleration rate (8 kg's/4 kg's) and pressure scaled by the product of tube diameter and deceleration rate (14 inches x 4 kg's/8 inches x 8 kg's).

The recovery temperature histories are shown in Figure 5-3. The initial value for the temperature of the helium is 22,000°R. The temperature decreases with time parabolically in direct correlation with the velocity of the projectile which is decreasing linearly with time. The localized temperature peaks are again a result of valve/shock interactions. The recovery temperature history for Cases 2 and 4 is identical to Case 1. Since the deceleration for Case 3 is one-half that of Case 1, the times for Case 3 are twice those for Case 1.

The other input required for the thermal analysis is the heat transfer coefficient which is determined from the model boundary layer analysis. Several typical heat transfer coefficient distributions are shown in Figure 5-4 for the flight and recovery test phases. The flight distribution is for a laminar boundary layer at an altitude of 40,000 feet. The distribution of heat transfer coefficient during recovery shows a stagnation point value about one-tenth that for flight. The values on the cone are nearly the same for recovery and flight. The distribution for Case 4 which is 10 times Case 2 is also shown.

Model pressure and stagnation point heat transfer coefficient histories are presented in Figure 5-5. Here it can easily be seen that the heat transfer coefficient history very closely follows the pressure. Again, the rises in pressure are a direct result of the compartments in the recovery tube.

The above input was used in the ANAP code to calculate the thermal response which is described next.

5.2.2 Output Results

The output of primary interest from the thermal calculation are temperatures (surface and in-depth) and surface recession.

Temperature Response

The stagnation point surface temperature history for Case 1 is shown in Figure 5-6 for a complete test sequence. Initially the model is preheated for 6 seconds during which it attains a temperature of 4370°R at the stagnation point. This is followed by the track guided flight at speeds on the order of 20,000 fps for approximately 1 second. In flight the stagnation point temperature rapidly increases to a steady state value (approximately 7900°R) and remains nearly constant. During recovery
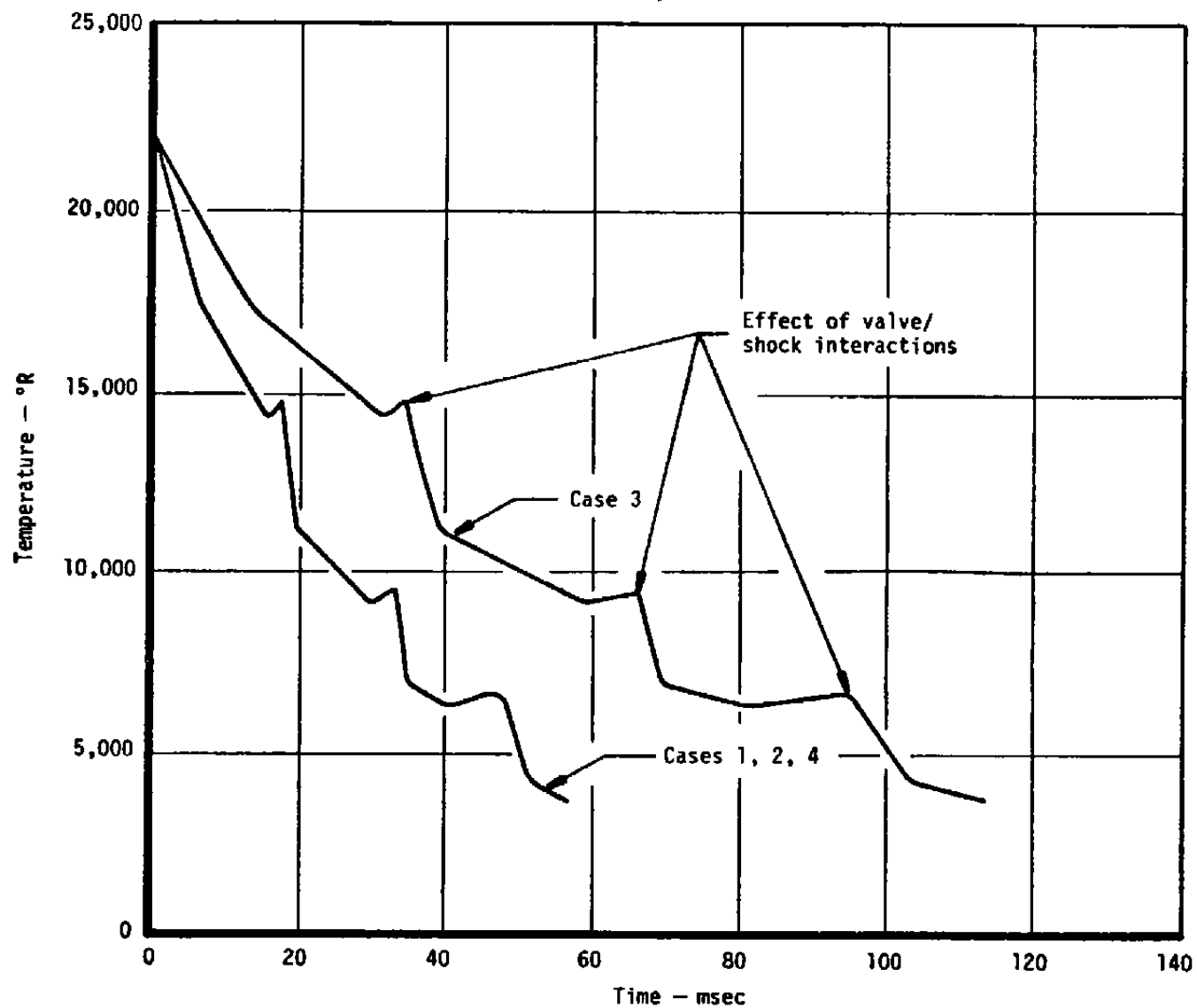
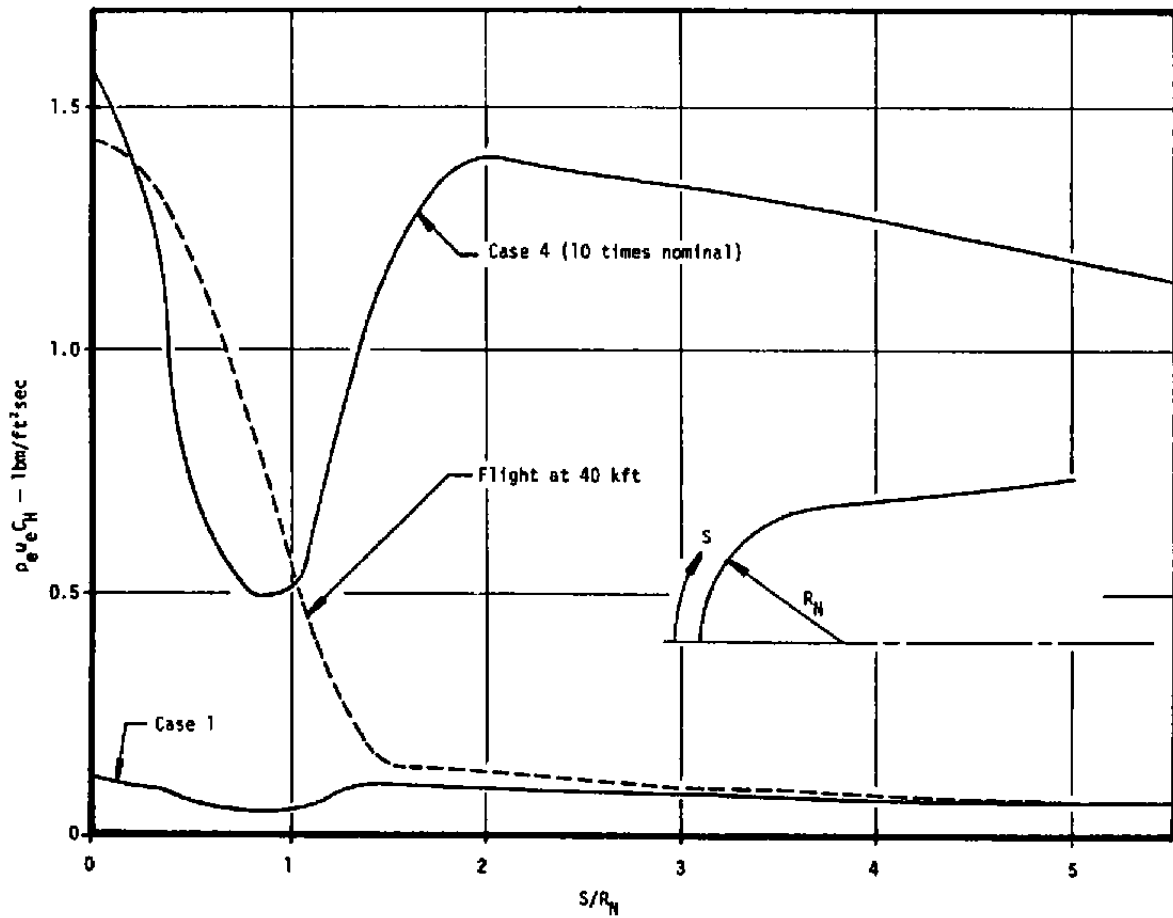Figure 5-3. Recovery temperature histories.

Figure 5-4. Example flight and recovery heat transfer coefficient distributions.
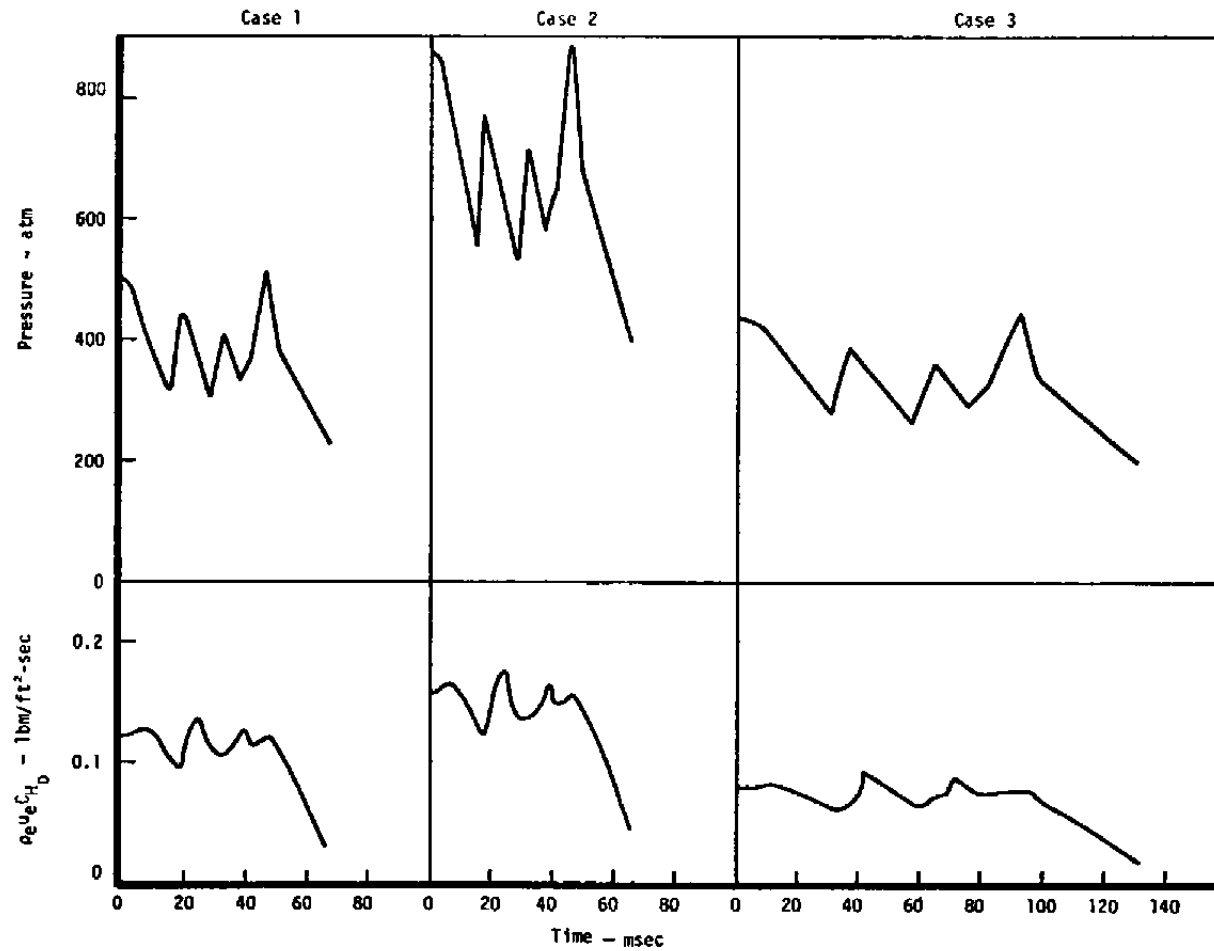
Figure 5-5. Variation of stagnation point heat transfer coefficient
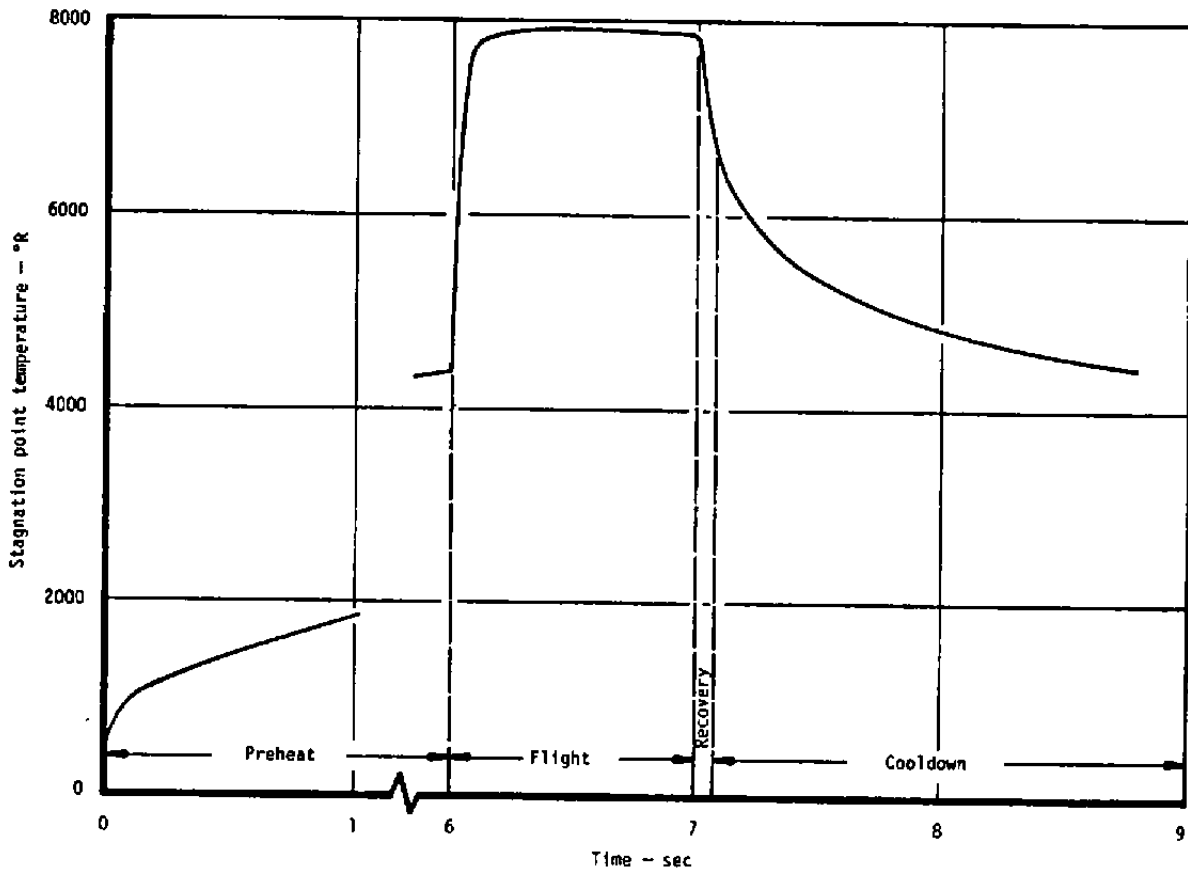with time during recovery.

Figure 5-6.   Case 1 stagnation point surface temperature history
for complete test sequence.

in the helium filled tube, the stagnation point temperature rapidly decreases to 6800°R. After re-covery, cooldown by radiation reduces the temperature to 4500°R in 1.5 seconds and 3800°R in 5 seconds.

The stagnation point temperature histories for all cases during recovery are presented in Fig-ure 5-7. The histories for Cases 1, 2, and 3 are very similar, but for Case 4 the temperature in-creases in the initial part of the recovery.

The fact that the initial recovery temperature in the recovery tube is significantly higher than in flight (22,000°R versus 13,000°R) and yet the surface temperature still decreases emphasizes how small the predicted recovery heat transfer coefficient is. Only when the predicted heating is increased by a factor of 10 (as in Case 4) does the high recovery temperature have an effect.

The in-depth cooldown thermal response for Case 1 is illustrated in Figure 5-8 by plots of temperature distribution along the nosetip centerline for various times. The radiation cooling at the surface causes a rapid reduction in surface temperature such that after 1 second of cooldown the temperature is 4780°R and 3800°R after 5 seconds. As a result of this rapid decrease in surface temperature the maximum temperature, after a short time, is no longer at the surface, but a small distance in depth. The value of peak temperature is plotted versus time in Figure 5-9 for all four cases. Peak temperature is shown plotted versus in-depth location in Figure 5-10.

In-depth temperatures are of concern because if the virgin in-depth graphite is exposed to temperatures greater than the graphitization temperature for relatively long periods of time, the properties of the material can be changed to such an extent that further testing of the nosetip would no longer be valid. Since the graphitization process is governed by reaction rate kinetics, not only is the peak temperature important, but also the length of time for which the material is exposed to the elevated temperatures. In a typical graphitization process an isothermal temperature of nominally 5000°R is maintained for many minutes and this cycle is repeated several times.

During the recovery/cooldown process the peak temperature is typically down to 5000°R within 1 second and has penetrated to a depth of less than 0.1 inch. Therefore, only a small amount of mate-rial is exposed to elevated temperatures and only for a very short period of time. Thus, any change in the microstructure and/or properties of the nosetip are anticipated to be small and localized near the surface.

Ablation Response

Stagnation point surface recession during recovery for all cases is shown in Figure 5-11. Ab-lation during recovery for Cases 1, 2, and 3 is less than 0.1 mil and is certainly negligible. Even for 10 times nominal heating (Case 4), ablation during recovery is still only about 2 mils which is less than 5 percent of the ablation during the range flight.
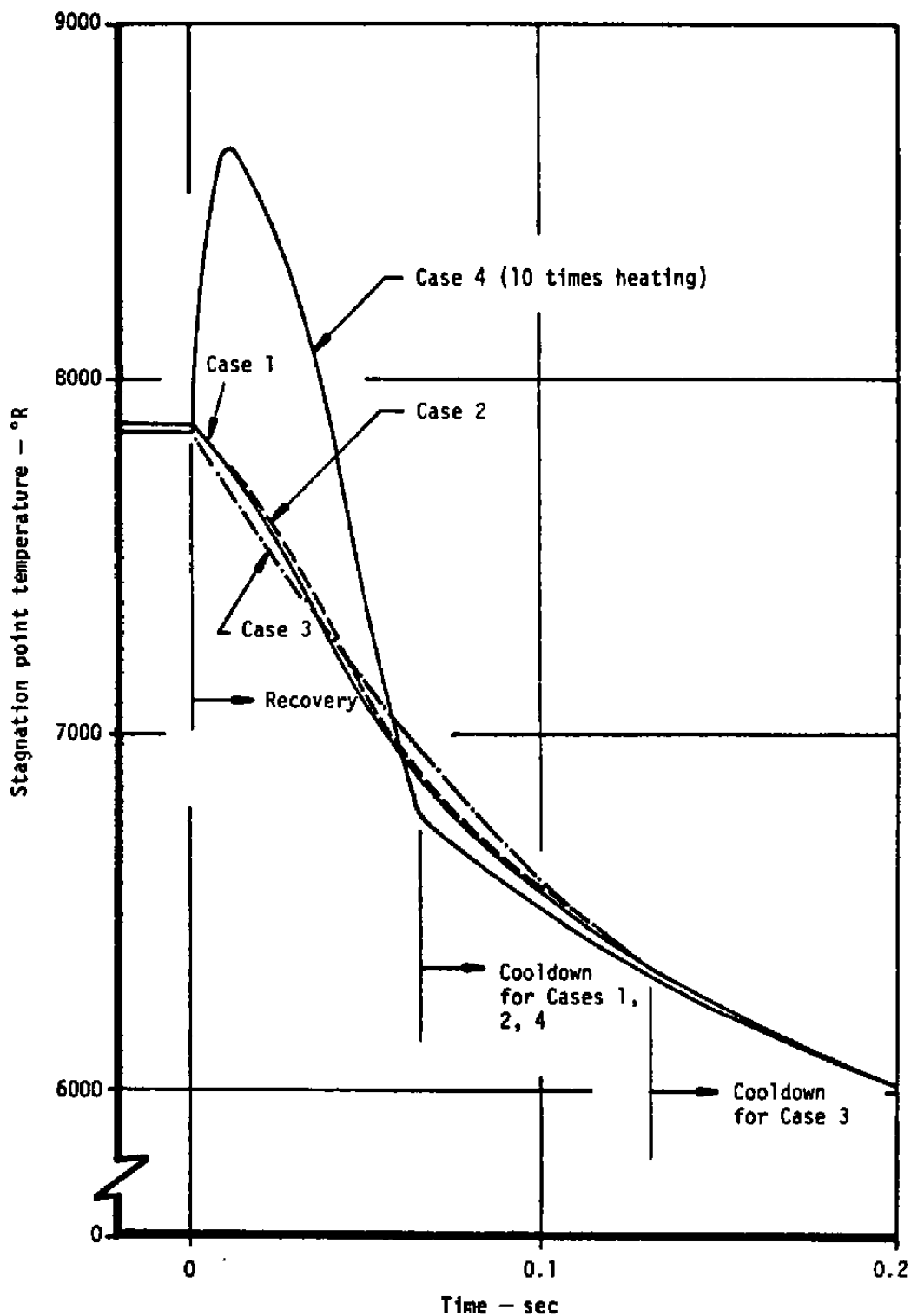
Figure 5-7. Stagnation point surface temperature during recovery for all cases.
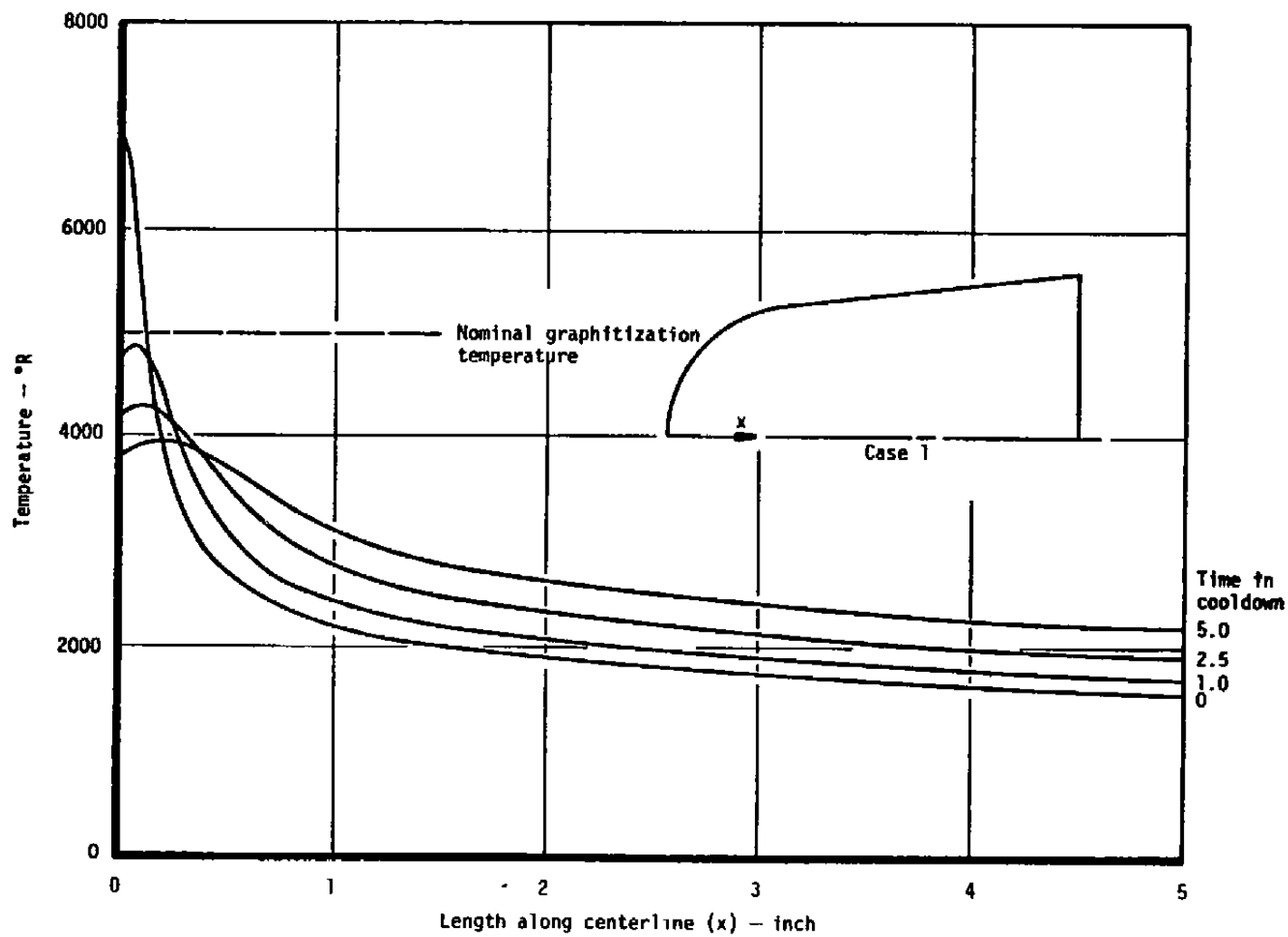
Figure 5-8.   In-depth thermal response during cooldown (Case 1).
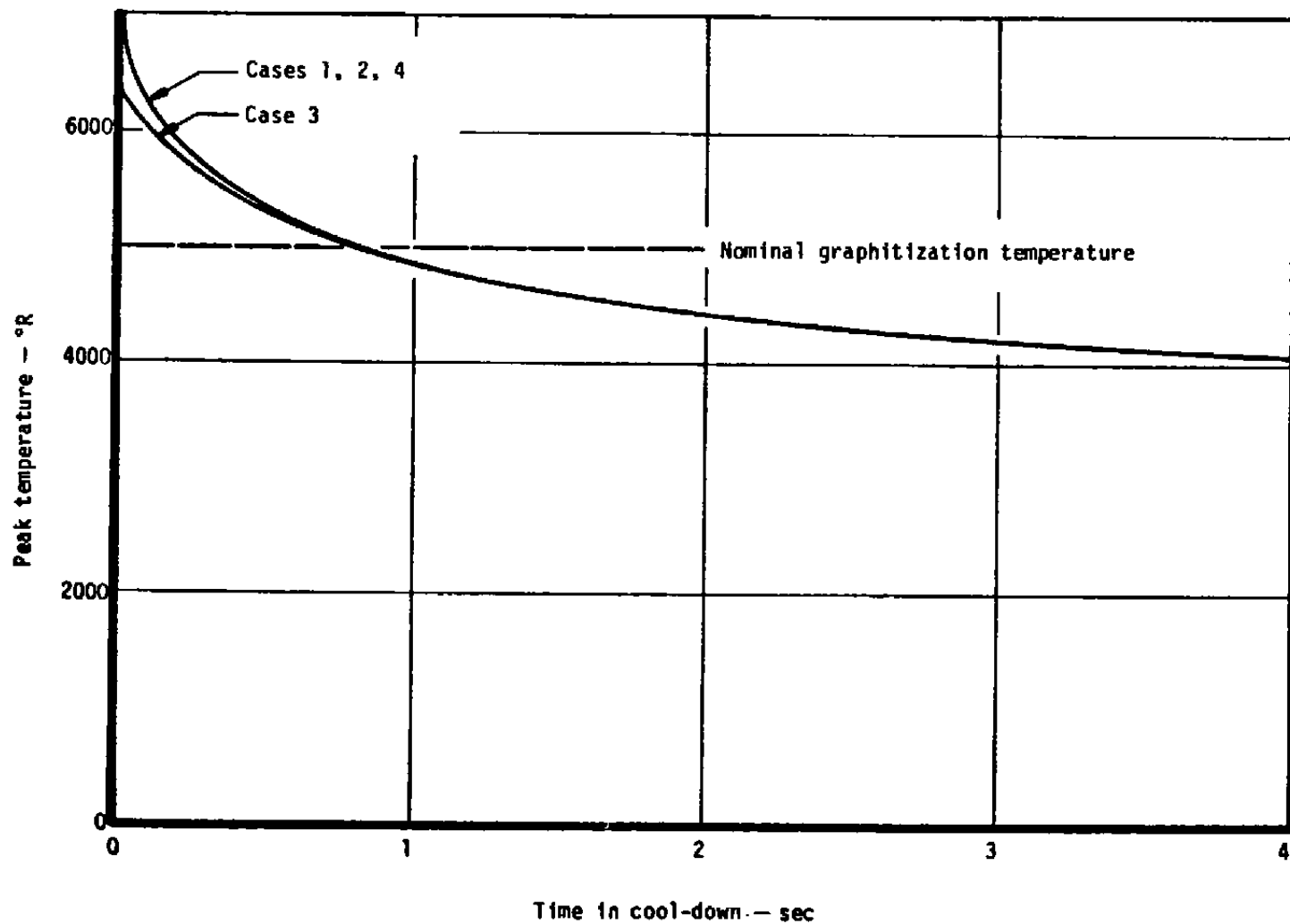
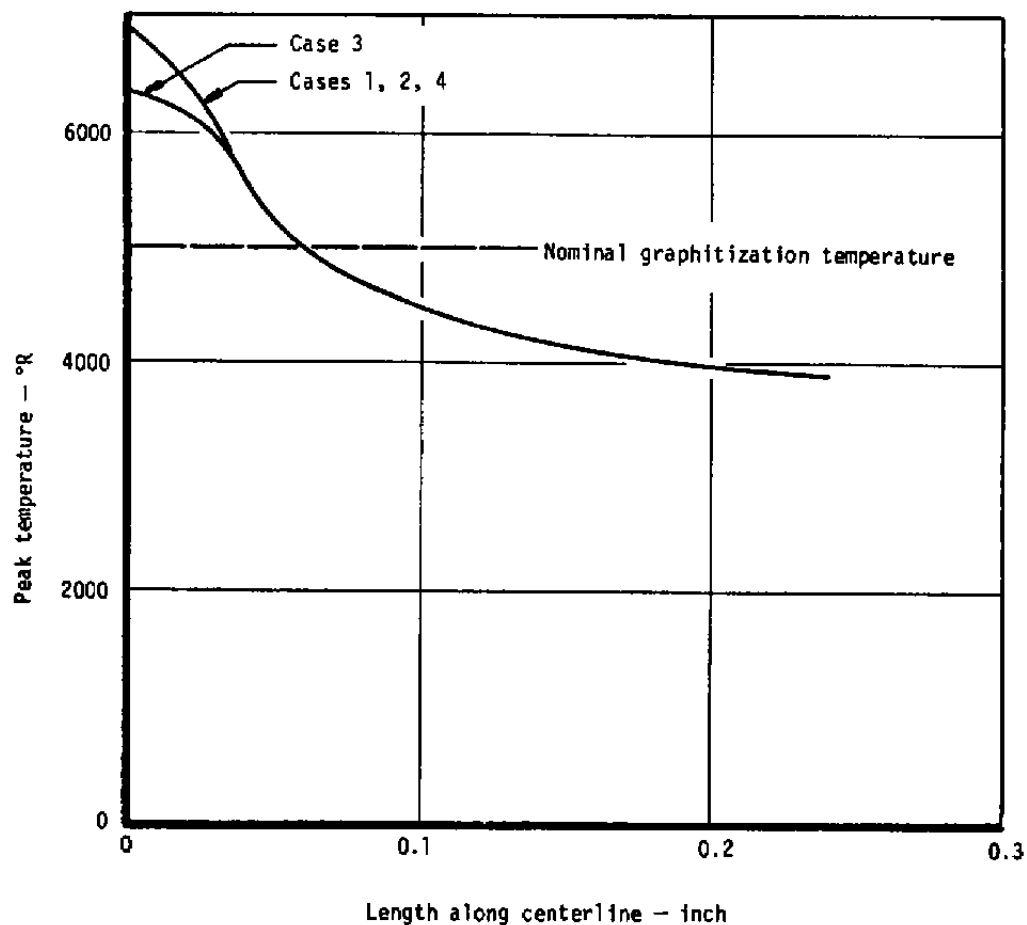Figure 5-9. Peak temperature during cooldown versus time.

Figure 5-10. Peak temperature during cooldown versus
in-depth location.
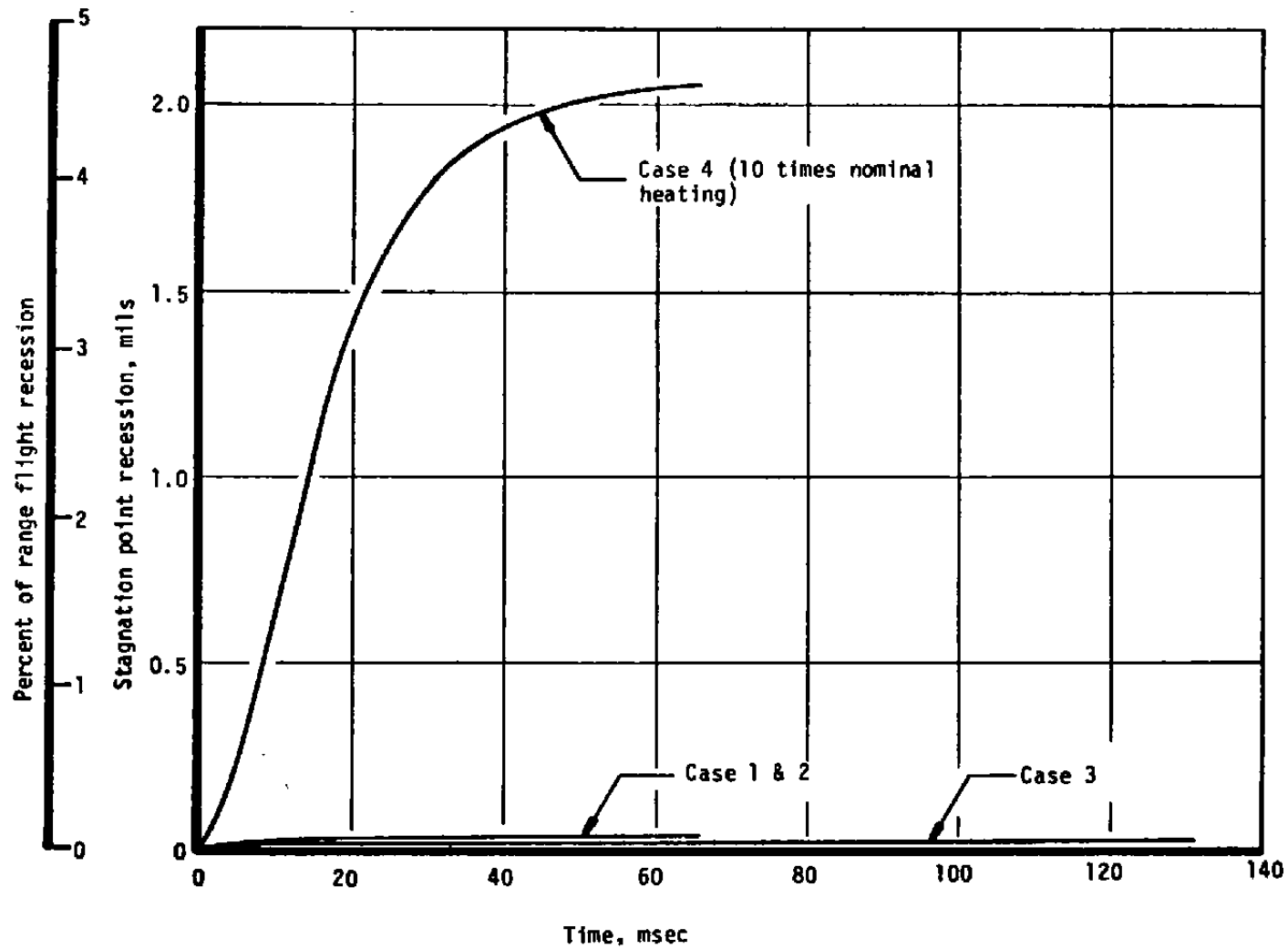
Figure 5-11.   Stagnation point surface recession during
recovery for all cases.

5.3   STRUCTURAL RESPONSE

This section presents the results of a matrix of structural solutions performed with the DOASIS code to assess the probability of model failure as a function of recovery tube design variables. First a description of the stress state and failure criteria during recovery is given. This is followed by a similar discussion of structural failure during cooldown.

5.3.1 Structural Response During Recovery

Structural analyses were performed for one time during recovery for each of the four cases outlined in Table 5-1. A description of the model stress state during recovery is first given. Next considerations of structural failure are discussed.

Description of Stress State

The model stress is determined by three forcing functions which are related to the key design variables as follows:

Forcing Function		Controlling Variables
Thermal stress	⟶	Heating
Pressure load	⟶	Deceleration, diameter
Body force	⟶	Deceleration

Consider first the thermally induced stresses. A typical temperature field during recovery is shown in Figure 5-12. The temperature varies from 8000°F to 1000°F. The outside region with about half of the nosetip volume has temperatures above 2000°F; the inner region has temperatures below 2000°F. This temperature field leads to stresses which are compressive in the temperature regions above 2000°F and tensile in those below 2000°F (Figure 5-13).

Stresses produced by pressure loads are always compressive. Body force stresses may be either tensile or compressive depending on location and body configuration.

The resultant stress state is determined by superposition of all stress. Figure 5-14 shows plots of the four stress components (σ_r — radial, σ_z — axial, σ_θ — hoop, and τ_{rz} — shear) as calculated by DOASIS for a typical recovery case.

All stress components are compressive which indicates that the compressive stresses generated by surface pressure are higher than the tensile stresses generated by temperature gradients. It should be noted that the stress state during recovery is quite different from that in flight. The stress state in flight is primarily due to thermal stresses.

CONTOURS PLOTTED

SYM	VALUE
⊡	1.20000E+03
	1.60000E+03
⊙	2.00000E+03
	2.40000E+03
△	2.80000E+03
	3.20000E+03
+	3.60000E+03
	4.00000E+03
✕	4.40000E+03
	4.80000E+03
◈	5.20000E+03
	5.60000E+03
✦	6.00000E+03
	6.40000E+03
✕	6.80000E+03
	7.20000E+03
Z	7.60000E+03
	8.00000E+03
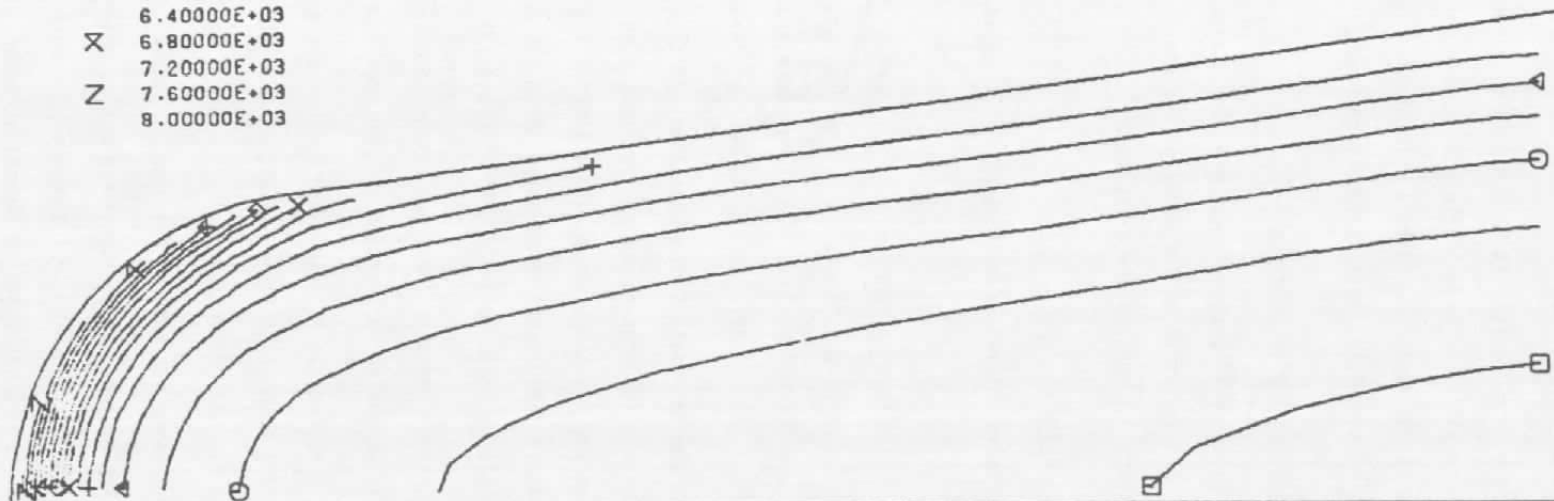
Figure 5-12.   Typical isotherm plot during recovery
(Case 1, 3 msec after tube entry).
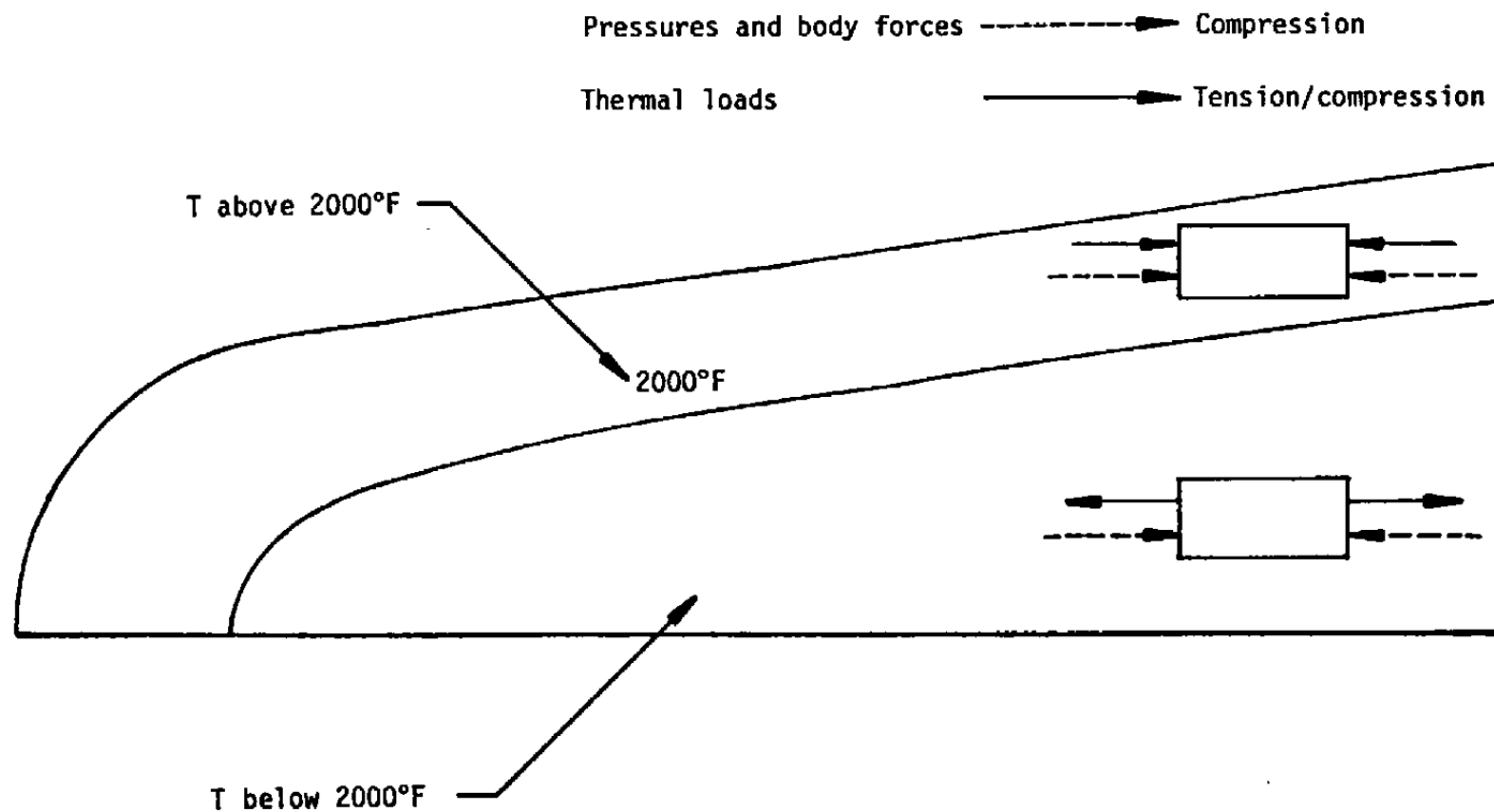
Figure 5-13.   Description of model stress state during recovery.

CONTOURS PLOTTED
SYM   VALUE

⊡	-1.50000E+04
	-1.40000E+04
⊙	-1.30000E+04
	-1.20000E+04
△	-1.10000E+04
	-1.00000E+04
+	-9.00000E+03
	-8.00000E+03
✕	-7.00000E+03
	-6.00000E+03
◇	-5.00000E+03
	-4.00000E+03
♠	-3.00000E+03
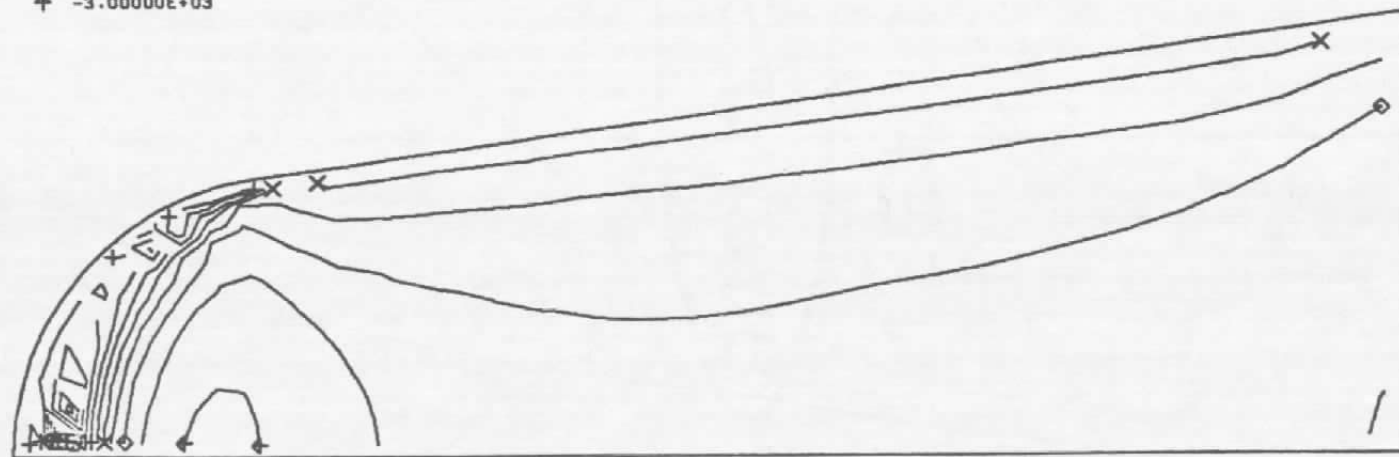
a.   Radial stress — σ_r

Figure 5-14.   Typical stress state during recovery (Case 1, 3 msec after tube entry).

b. Axial stress — σ_z

Figure 5-14. Continued.

CONTOURS PLOTTED
SYM   VALUE

⊡   -1.60000E+04
    -1.50000E+04
◉   -1.40000E+04
    -1.30000E+04
△   -1.20000E+04
    -1.10000E+04
+   -1.00000E+04
    -9.00000E+03
✕   -8.00000E+03
    -7.00000E+03
◇   -6.00000E+03
    -5.00000E+03
⬆   -4.00000E+03
    -3.00000E+03
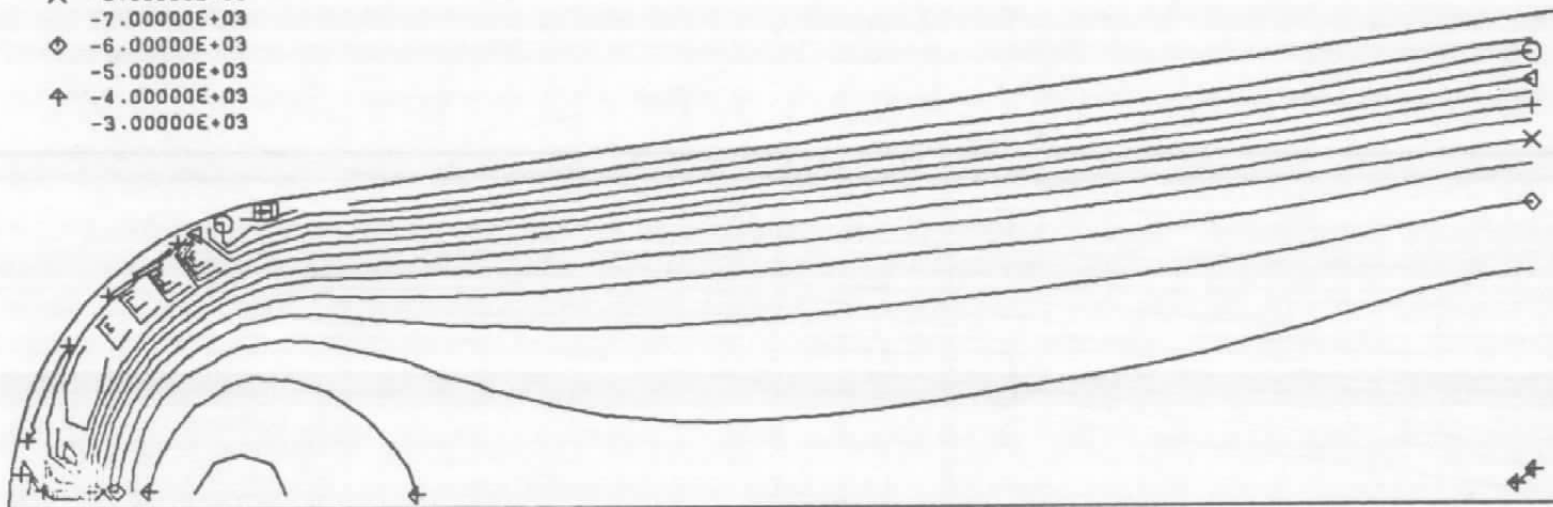
c. Hoop stress — σ_θ

Figure 5-14. Continued.

CONTOURS PLOTTED
SYM   VALUE

⊡   0.00000E+00
       2.50000E+02
⊙   5.00000E+02
       7.50000E+02
△   1.00000E+03
       1.25000E+03
+   1.50000E+03
       1.75000E+03
×   2.00000E+03
       2.25000E+03
◇   2.50000E+03
       2.75000E+03
⬆   3.00000E+03
       3.25000E+03
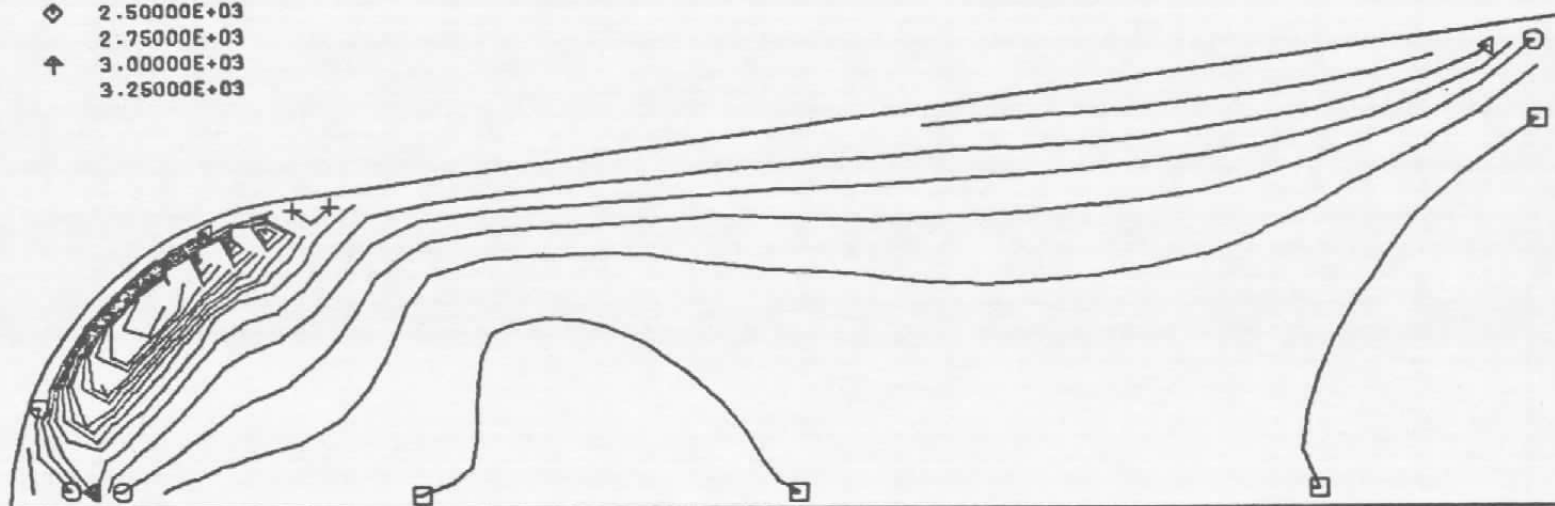
d.   Shear stress — τ_{rz}

Figure 5-14.   Concluded.

The shear stresses τ_{rz} are much less than the compressive normal stresses. This stress field of all compressive normal stresses and low shear stress resembles closely a hydrostatic compressive stress field.

The high stress loads indicated in Figure 5-14 give some concern that plastic yeilding may occur. However, plastic yield theory indicates that under purely hydrostatic compression no plastic yielding will even occur. Thus an elastic solution of a structure under purely hydrostatic compression will be the same as that of a plastic solution. In order to verify that the stress state during recovery is sufficiently close to hydrostatic compression to allow the use of the more easily applied elastic theory a plastic solution for Case 2 was performed. As expected, the stress fields in the nosetip during recovery were very similar to the elastic response. Therefore only elastic solutions were performed for all subsequent cases.

Structural Failure Considerations

There are numerous failure criteria. Some are good for only certain loading conditions and others are valid for only certain classes of materials. The simplest and the most common failure criterion is to compare the maximum tensile and compressive stresses (strains) with the allowable tensile and compressive stresses (strains). This method is not very conservative since it neglects biaxial and triaxial stress effects.

Tsai and Wu (Reference 22) and Priddy (Reference 23) have developed failure criteria for anisotropic materials with biaxial and triaxial effects. To use their failure criteria with confidence, one must have complete experimental data from material strength tests. For ATJ-S graphite, strengths of uniaxial tensile and compressive stresses at various temperatures are quite complete, but there are only a few tests on shear, biaxial and triaxial stresses. In order to use Tsai-Wu' or Priddy failure criteria, we must interpolate or extrapolate strength data from the available data.

Our structural analysis results for recovery cases are somewhat unusual. None of the above mentioned failure criteria are appropriate, and they lead to contradictory results. For example, if we compare the maximum compressive stress in each case with the allowable uniaxial compressive stress (Figure 5-15, Reference 31) the nosetip is predicted to fail in all cases except 3. If we compare the maximum compressive strains with the allowable uniaxial strain of 0.05 in/in (Reference 25). The nosetip is not predicted to fail in any of the cases.

The reason for these contradictions is that the above failure criteria are not applicable to a stress field resembling hydrostatic compression. This leads us to use the allowable shear strain as our failure criteria. This is because shear strains (stresses) are generated by deveiations from a purely hydrostatic load.

108
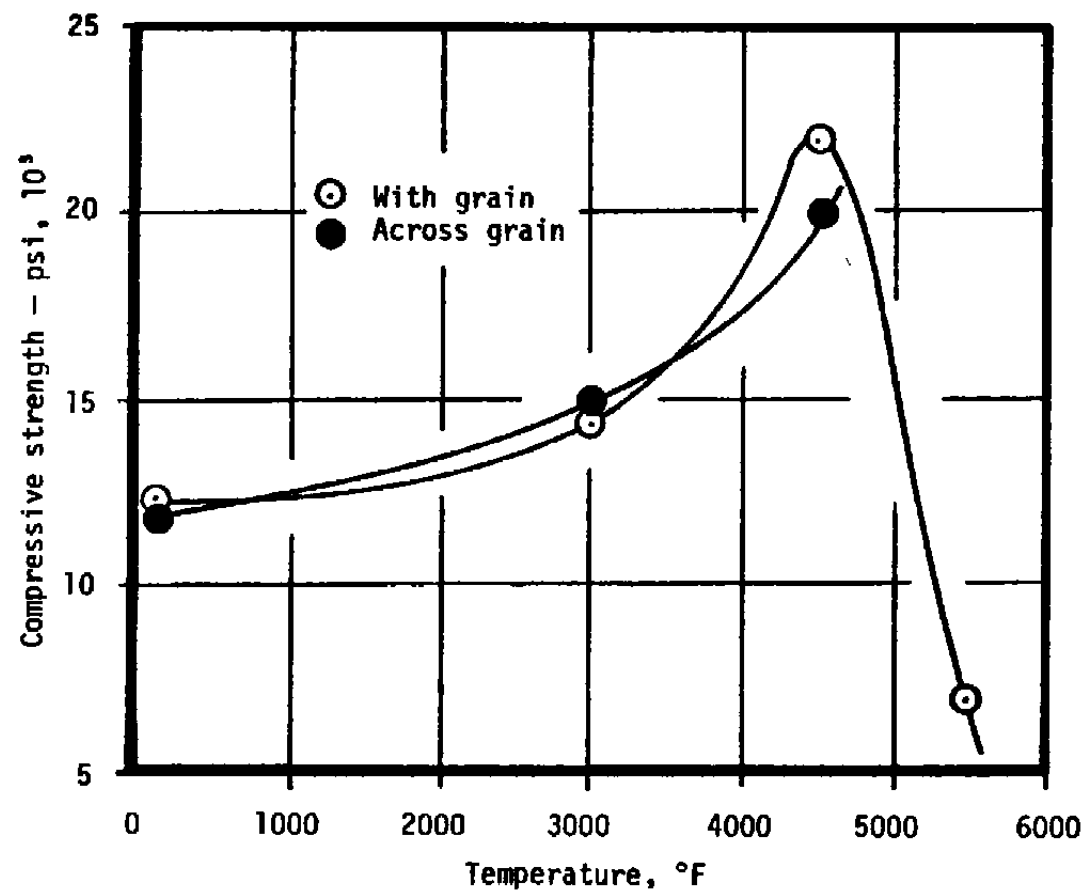
Figure 5-15. Compressive strength for ATJ-S graphite
vs temperature (Reference 31).

There is no available experimental test data for allowable shear strain. But conservative values can be estimated from the allowable uniaxial compressive strains. If the material under compression test fails due to the maximum shear strain on planes at 45° to the compression direction, then the shear stress and the corresponding shear strain are related to the compression stress and strain as:

$$\tau_{rz} = 1/2 \; \sigma_z \qquad\qquad\qquad (5-1)$$

$$\gamma_{rz} = \epsilon_z \qquad\qquad\qquad (5-2)$$

References 24 and 25 report that the compressive fracture strain of ATJ-S graphite at room temperature is about 0.05 in/in. According to Equation (5-2), the allowable shear strain at room temperature is also 0.05 in/in. The values of the allowable shear strains at higher temperatures are extrapolated and are shown in Figure 5-16.

The shear strain ratio is defined as the ratio of the actual to the allowable shear strain. Shear strain ratios were calculated for each recovery case. A typical contour for Case 1 is shown in Figure 5-17. The maximum strain ratio occurs near the nosetip back shoulder. As shown previously (cf Figure 5-14(b)) this is also the region of maximum compression. For each case the maximum shear strain ratio was evaluated and compared with the key design variables. Figure 5-18 summarizes these results.

Figure 5-18(a) shows the effect of model heating on maximum shear strain ratio. The first point on the left was calculated using the loading conditions of Case 2 with an isothermal temperature field (i.e., no heating). The second point is Case 2 with nominal heating, and the third is Case 2 with ten times nominal heating (i.e., Case 4). As the plot shows there is a definite effect going from zero heating to nominal heating but little effect going for nominal to ten times nominal. In any case the maximum shear strain ratio is well below predicted failure.

In Figure 5-18(b), the design variable is the tube diameter D. This figure indicates that the maximum shear strain ratio increases as the tube diameter increases. This is a result of the associated increase in pressure with tube diameter. Figure 5-18(c) shows that deceleration rate has a similar effect on shear strain as diameter. The maximum shear strain ratios for all recovery cases are far below the failure line and thus no structural failure problems are anticipated during recovery.
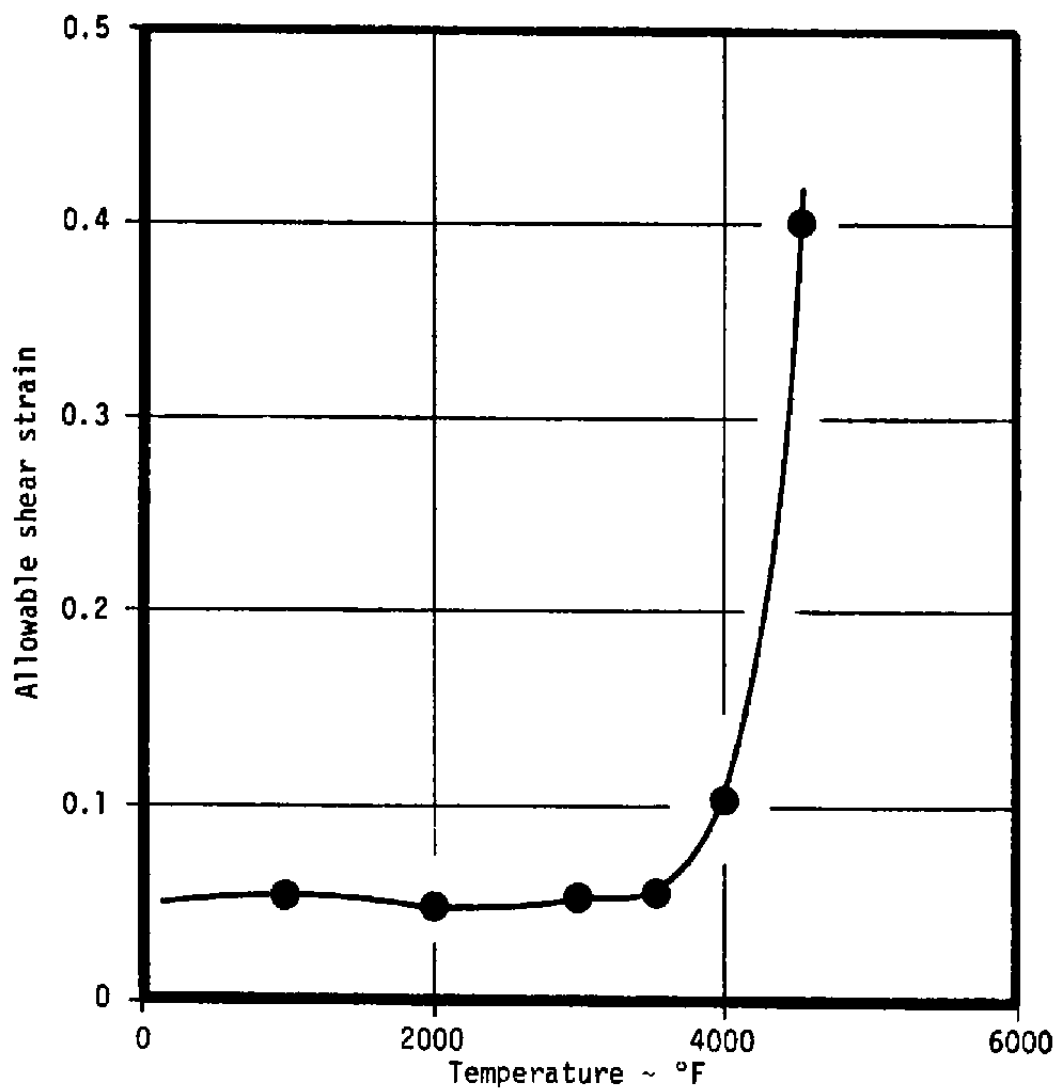
Figure 5-16.   Allowable shear strain versus temperature.
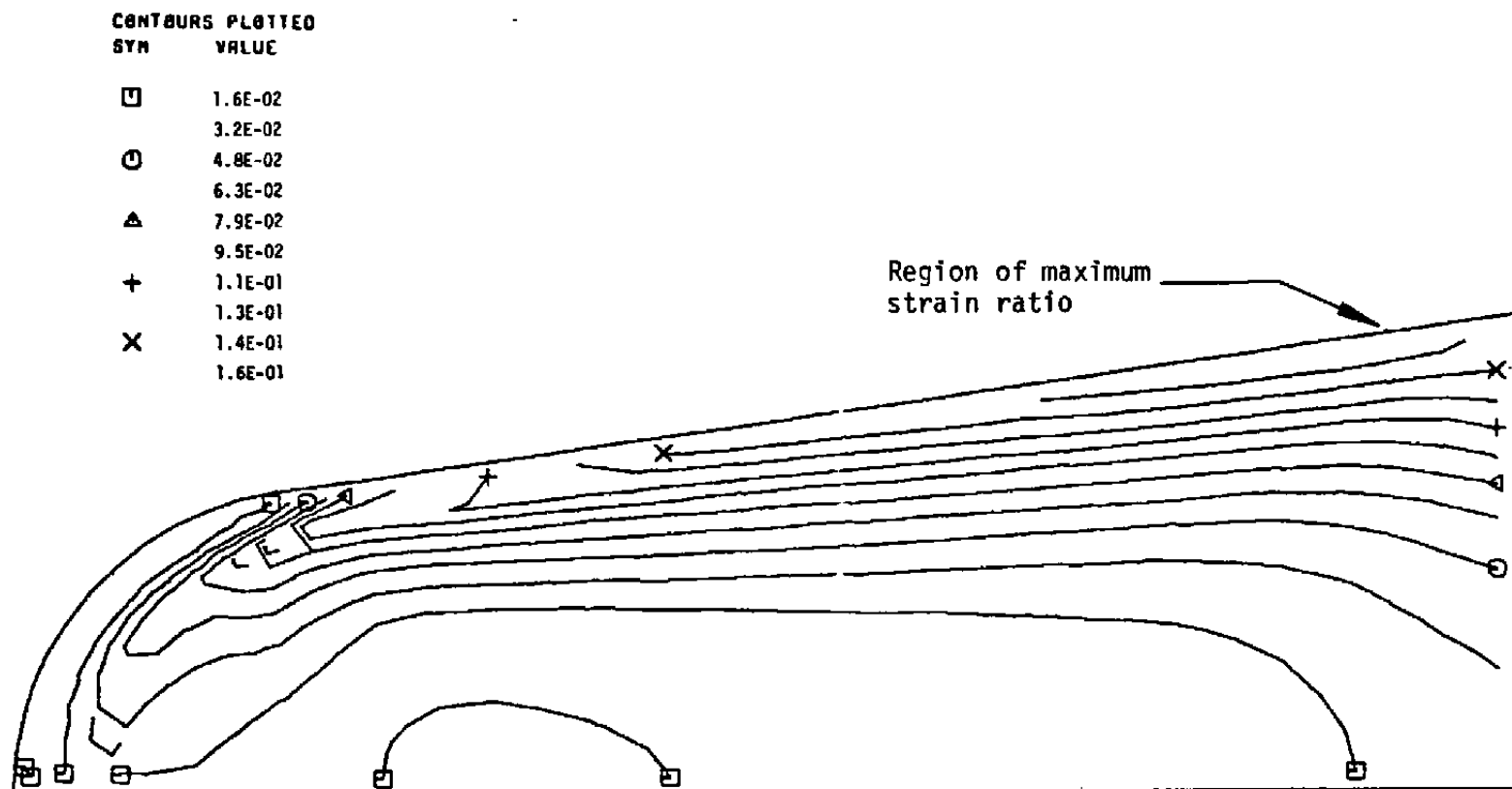
Figure 5-17. Typical shear strain ratio contour (Case 1).
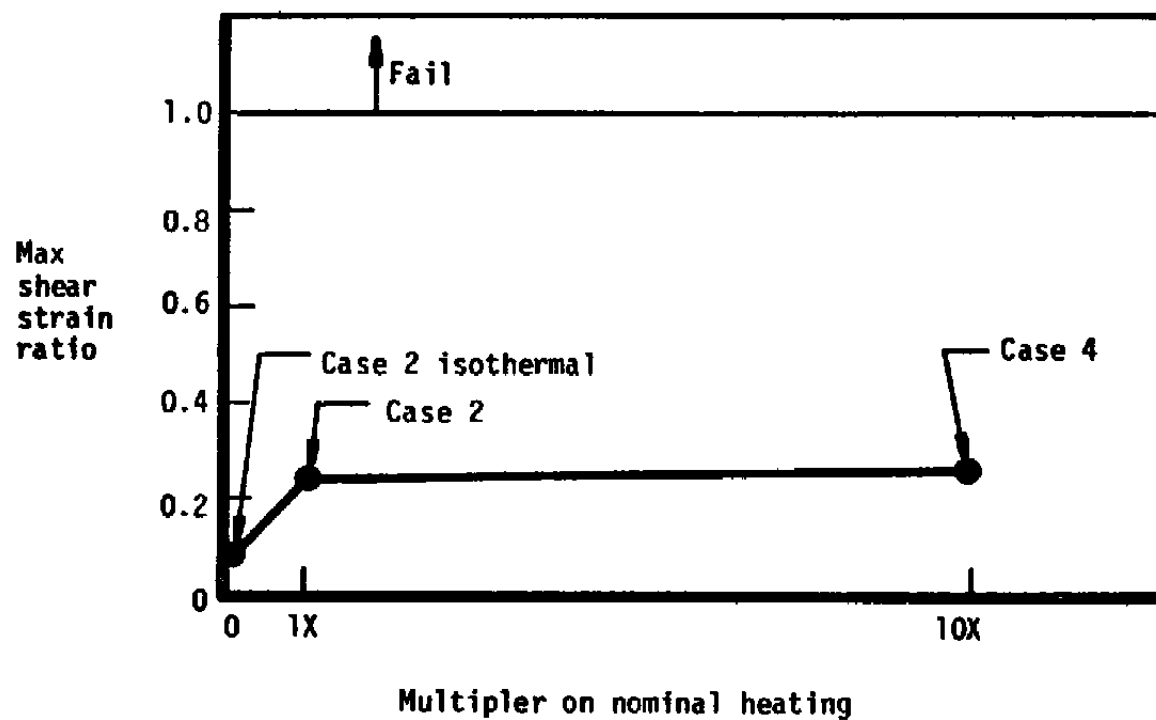
a. Effect of model heating.

Figure 5-18. Effect of design variables on
maximum shear strain ratio.
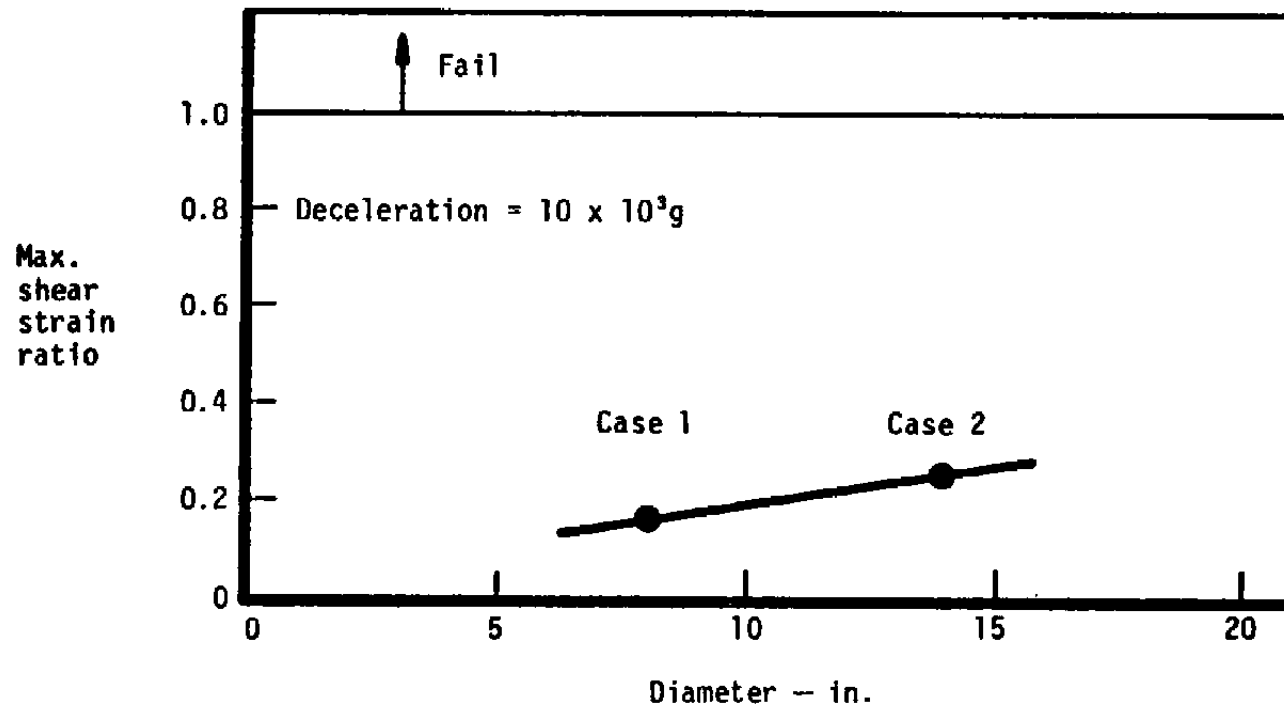
b. Effect of tube diameter

Figure 5-18. Continued.
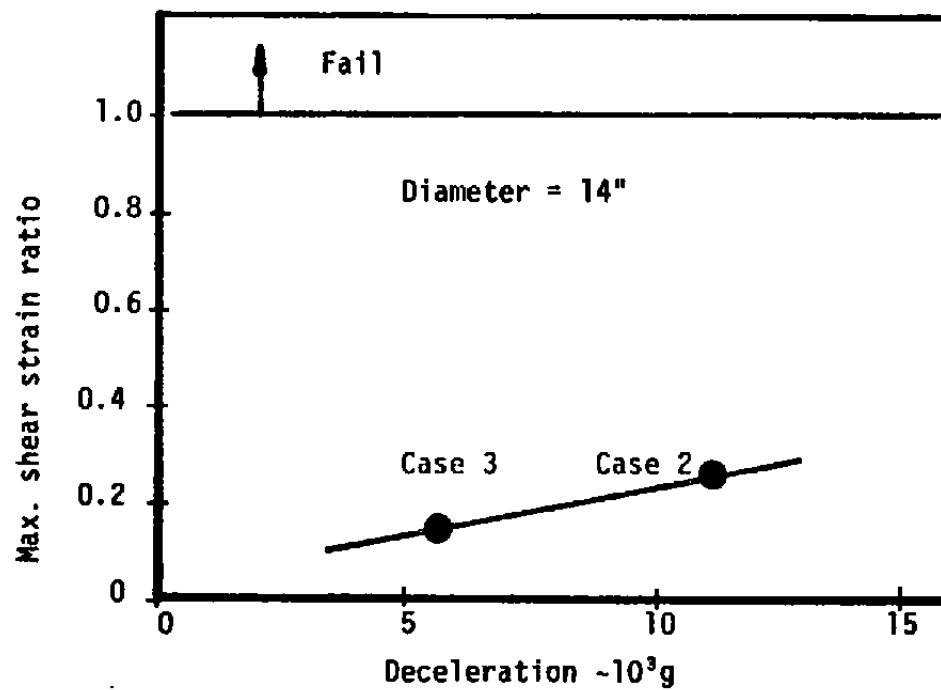
c.   Effect of deceleration.

Figure 5-18.   Concluded.

5.3.2 Structural Response During Cooldown

During cooldown, there is no surface pressure and the stresses in the nosetip are generated by the thermal field alone. To see the effect of thermal load, Case 2 was structurally evaluated during cooldown. The input temperature field is shown in Figure 5-19. The axial stress (σ_z) has the highest magnitude and it is shown in Figure 5-20. This figure indicates that the inner half of the body is in tension and the outer half is in compression.

The Tsai-Wu structural failure criterion was used for Case 2 during cooldown. The failure criterion indicates that the tensile stress components along the nosetip center line will cause structural failure. However, these strains are dependent upon the nosetip overhang length which can be shortened to insure a safe design. This is also true when the model is accelerating during launch and in subsequent flight. Although the present analysis was concerned only with recovery, higher strains are expected during flight than during cooldown. An assessment of model survival must include flight, recovery and cooldown.

Thus in actual application a model which is designed to survive launch and flight stress will, in all likelihood, also survive cooldown stresses.

CONTOURS PLOTTED

SYM	VALUE
⌑	1.20000E+03
	1.60000E+03
◐	2.00000E+03
	2.40000E+03
△	2.80000E+03
	3.20000E+03
+	3.60000E+03
	4.00000E+03
✕	4.40000E+03
	4.80000E+03
◇	5.20000E+03
	5.60000E+03
✛	6.00000E+03
	6.40000E+03
⋈	6.80000E+03
	7.20000E+03
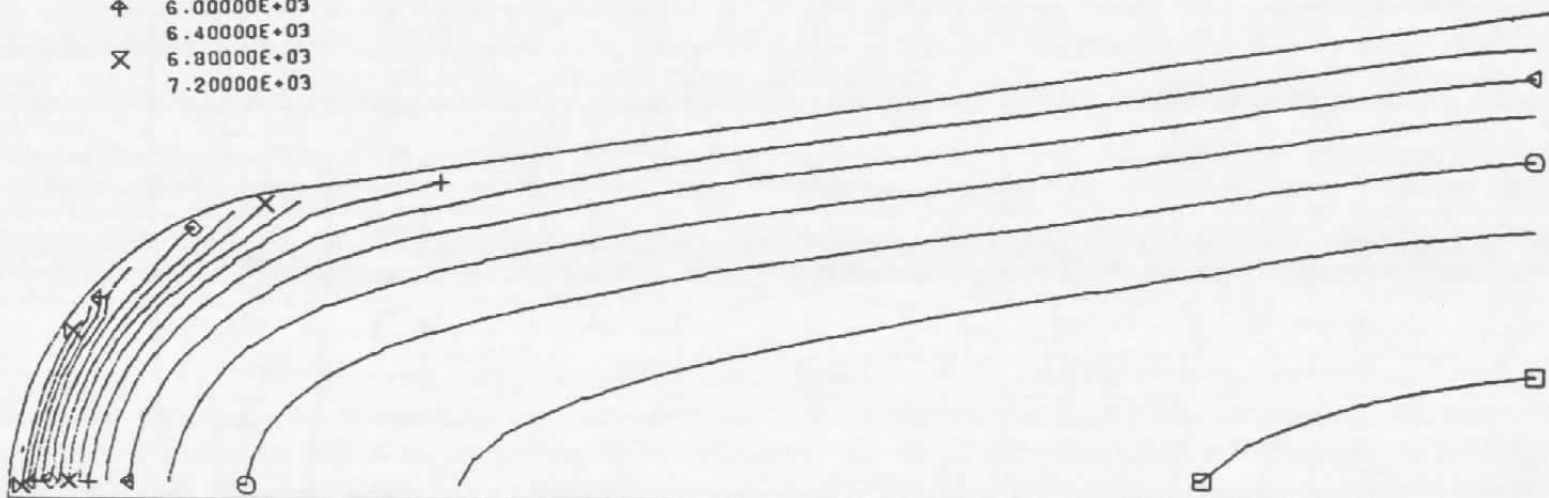
Figure 5-19.   Typical isotherm plot during cooldown
(Case 2, 7 msec after the beginning of
cooldown).

CONTOURS PLOTTED
SYM   VALUE

⊡   -7.00000E+03
    -6.00000E+03
⊙   -5.00000E+03
    -4.00000E+03
△   -3.00000E+03
    -2.00000E+03
+   -1.00000E+03
    0.00000E+00
×   1.00000E+03
    2.00000E+03
◇   3.00000E+03
    4.00000E+03
♦   5.00000E+03
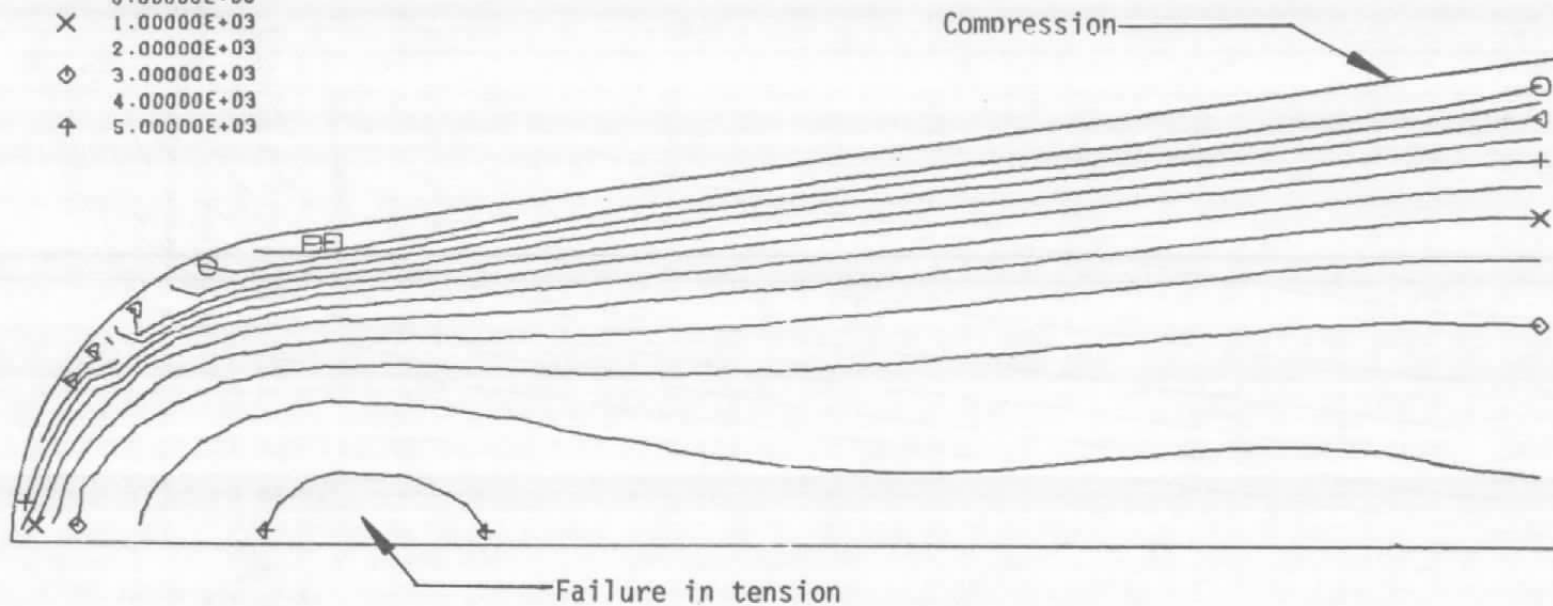
Figure 5-20. Typical axial stress (σ_z) during cooldown
             (Case 2, 7 msec after the beginning of
             cooldown).

SECTION 6

COST OPTIMIZATION RESULTS

The final aspect of the effort described herein is a study of the cost optimization of a re-
covery tube system. The objective of this study is to determine the design parameters of an optimum
cost effective recovery tube system. Section 6.1 below describes the cost analysis technique used.
In Section 6.2 this technique is applied to a matrix of designs covering the range of interest for
the key variables of deceleration rate, tube diameter, and number of compartments. Section 6.3 de-
scribes a preliminary design of the optimum system with an associated refined cost estimate. In
addition, the effects of operating the facility with various gases and variations in projectile
initial velocity are examined.

6.1 COST ANALYSIS TECHNIQUE

In general, the technique used to estimate costs for the various recovery tube systems involved
the following four basic steps:

- List the basic system elements and costs for a conceptual design.

- Segregate the fixed cost elements from the variable cost elements.

- Develop appropriate cost scaling factors and rules for the variable cost elements.

- Estimate the total system costs for various parametric cases.

6.1.1 Conceptual Design

Figure 6-1 shows the recovery tube conceptual design used to develop a cost analysis technique.
It consists basically of an entry section, a deceleration section which is simply a tube with fast
acting valves, a shock extension section, a friction section, and finally a muffler and barricade.
The short entry section was utilized between the end of the range tank and the first valve location
as a transition from the track-guided range to the recovery tube. This section will permit shock
development in the completely confined recovery tube before reaching the first valve location. The
initial portion of the entry section would probably be slightly tapered. Each compartment is sepa-
rated by a quick operating valve actuated by the signal from a pressure transducer placed a suitable
distance upstream of the valve.
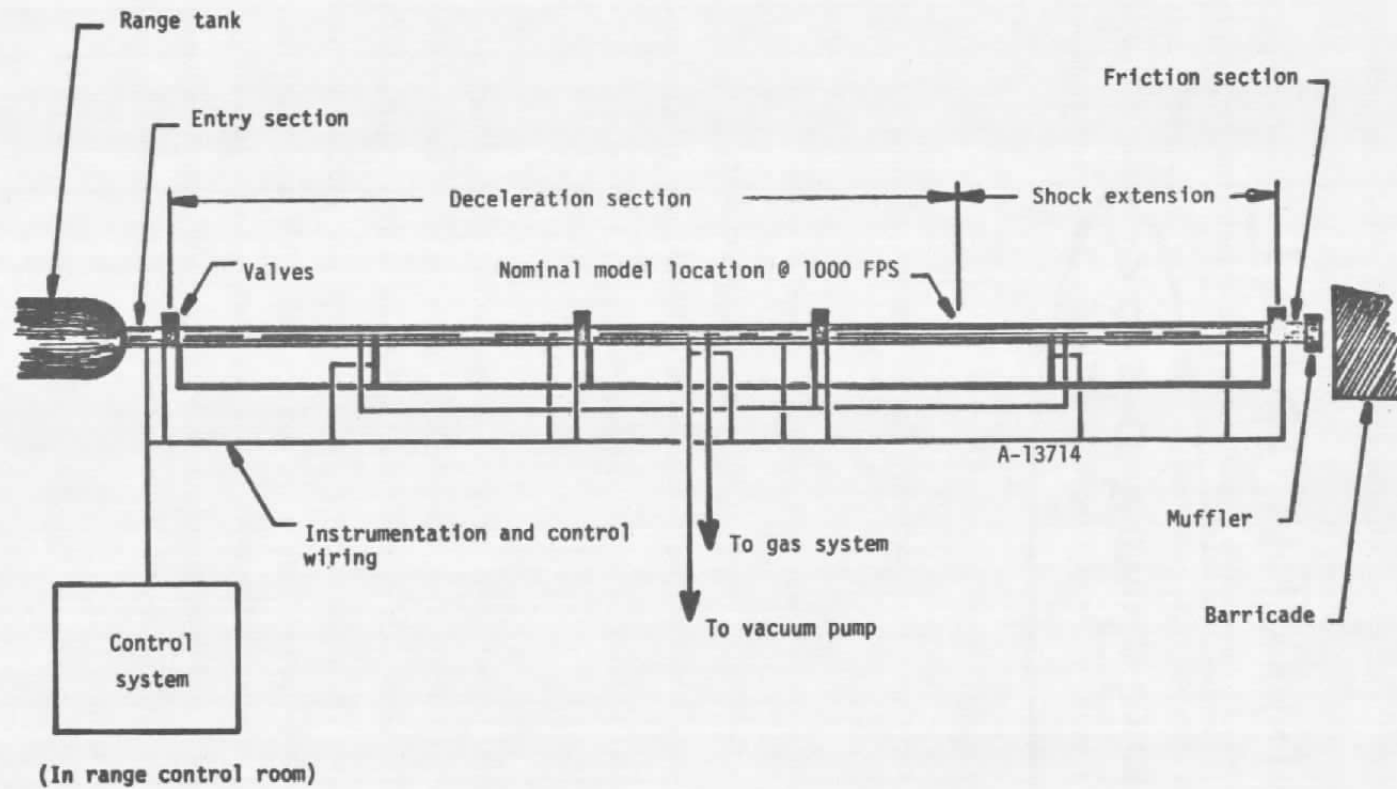
Figure 6-1. Recovery tube conceptual design.

The length of the system has been sized such that the rarefaction wave from the downstream open end reaches the projectile location when a projectile velocity of 1000 ft/sec is achieved. The term "shock extension" has been applied to the tube length between the 1000 ft/sec location and the end. A small amount of additional model deceleration will occur, however, in the shock extension portion.

A valve rather than a burst diaphragm has been used at the end of the shock extension to eliminate the reflection of a compressive wave from a burst diaphragm surface. A short friction section is included after the shock extension. The friction section might, for example, contain spring-loaded rails to bring the model to a complete stop. A muffler and safety barricade complete the downstream end of the facility.

A control system primarily designed to properly control all valve functioning has been included. This equipment is assumed to be located in the control room for the entire range. A vacuum pump and gas charging system have been included to purge the recovery tube of air and backfill the compartments with the desired charge gas.

The various elements involved in the conceptual design of Figure 6-1 are listed in Table 6-1. Those items assumed to be fixed costs regardless of system parameters include the valves, muffler and barricade, detailed design, and facility checkout and debug. It is assumed that the detailed design effort includes the development costs of the quick operating valve.

6.1.2 Structural Sizing

The recovery tube was structurally sized using the distortion-energy (Von Mises-Hencky) yield theory for biaxial principal stresses. This theory is well established for the analysis of gun tubes as discussed in Reference 26. When expressions for the radial and circumferential stresses on the inner surface of a thick-walled tube are substituted into this yield theory, the resulting equation is:

$$W = \left\{ \frac{1 + 2\frac{P}{Y} \sqrt{1 - \frac{3}{4}\left(\frac{P}{Y}\right)^2}}{1 - 3\left(\frac{P}{Y}\right)^2} \right\}^{1/2}$$

where

$W = \dfrac{\text{outside diameter}}{\text{inside diameter}}$

P = design pressure in psi

Y = tensile yield stress in psi

TABLE 6-1. SYSTEM ELEMENTS

Hardware	Labor
1. Tube entry section	*1. Detailed design (includes valve development)
2. Tube deceleration section (standard and high pressure tubing)	2. Site Preparation
3. Tube friction section	3. System installation
4. Spacers	*4. Checkout and debug
*5. Valves	
6. Tube supports	
7. Vacuum system	
8. Gas charging system	
9. Control system	
*10. Muffler and barricade	
11. Asphalt runway	
12. Spares	

*Fixed costs

Tubes were sized for a factor of safety of 2 with respect to tensile yield stress. Two dif-
ferent steels were considered in the tube designs: a 1025 carbon steel with a tensile yield stress
of 44 ksi and a 4140 alloy steel (normalized) with a tensile yield stress of 90 ksi. After applying
the factor of safety, the allowable stresses in the structural sizing equation become 22 and 45 ksi
respectively for carbon and alloy steel.

Vendor prices were obtained for both steels for use in facility cost estimation. The carbon
steel cost is approximately 40 cents per pound and the alloy steel is approximately 70 cents per
pound. Figure 6-2 shows the resulting cost for basic 15 foot long sections of 8 inch inside diameter
tube as a function of operating pressure. The pressure limit shown for each steel type is determined
when the denominator of the design equation equals zero. The carbon steel is cost effective only at
pressures of 200 atmospheres and below.

One factor that must be considered in the operation of a high pressure tube made of steel is
the possible loss of ductility at low temperature. The phenomenon of nil-ductility transition tem-
perature in steels is discussed in detail in Reference 27. For carbon steels the nil-ductility
transition temperature is quite high, possibly as high as 50°F. Therefore, a facility constructed
of carbon steel should not be operated at low ambient temperatures. Alloy steel, however, exhibits
considerably better characteristics in this regard. Reference 27 states that quenched and tempered
4140 steel is recommended for operation at temperatures down to -50°F.

6.1.3 Costing of Baseline Case

The system element breakdown and tube sizing considerations described above were used to esti-
mate the cost of a "baseline" recovery tube system. The parameters for the baseline case included
5 compartments, a nominal 8,000 g deceleration rate, 8-inch inside diameter, and helium charge gas.
The results of shock/dynamics calculations were used to determine the appropriate tube length of 800
feet by using the shock extension criterion previously described. The shock/dynamics calculations
also provide the pressure information necessary for tube sizing. This facet will be discussed in
more detail later in this section. For the baseline case the bulk of the tube is designed for a 700
atm operating pressure with a short high pressure section designed to operate at 1200 atm. The high
pressures are caused by shock interactions that occur near the front of the last compartment.

Cost estimates for each of the elements in the baseline case are summarized in Table 6-2. Alloy
steel is the appropriate choice for the relatively high operating pressures of the baseline case. The
pipe will be constructed of basic 15 foot sections with standard slip-on flanges welded on at each end.
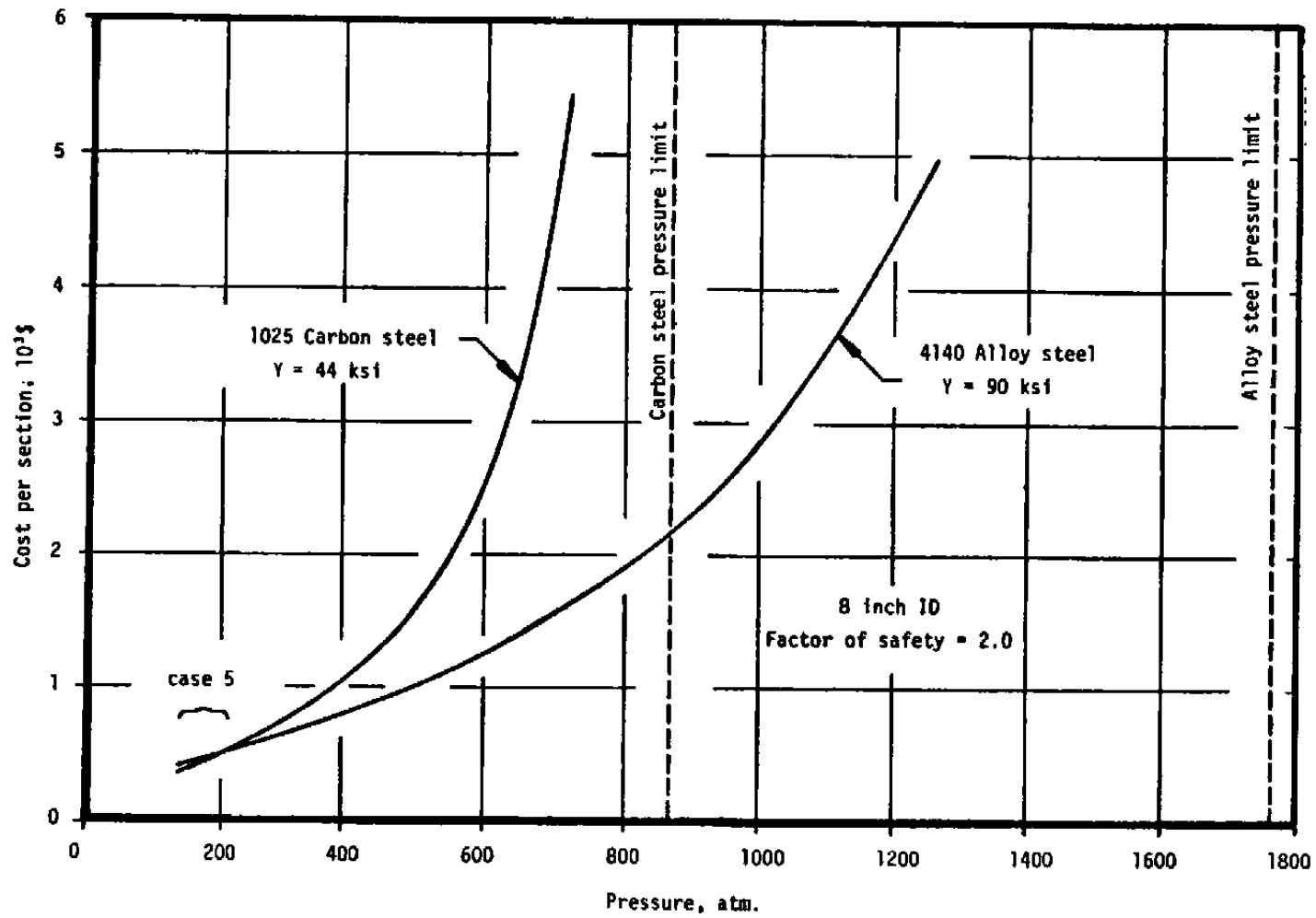
Figure 6-2. Steel tube cost.

TABLE 6-2. BASELINE CASE ELEMENT COSTS

Element	Cost
● Standard 15-foot tube section (700 atm)*	
— Material	
Seamless tubing, 4140 alloy steel, normalized to 90 ksi, raw stock 10 IPS (10.75" OD) x 1.5" wall @ $105/ft	$ 1580
Flanges 2 @ $200 each	400
— Labor	
Weld flange, face, bore, hone (ID 8.000 ± 0.002)	1100
Chrome plate	1000
Inspect	100
— Shipping (assume 1000 miles)	170
TOTAL	$ 4350
● Tube entry section 2x standard section	8700
● Tube friction section 3x standard section	13050
● Spacer	150
● Quick operating valve	3000
● Tube support Two per tube section	400 ea
● Vacuum system 70 cfm	2000
● Gas charging system Two shot He quantity plus plumbing	3000
● Control system $10000 minicomputer plus $1000 per valve station	15000
● Muffler and Barricade	500
● Asphalt runway 15 feet wide	18000

*Based on vendor estimates, weight = 2060 lb/section

Vendor estimates were obtained for the fabrication of these pipe sections. Two quite expensive pro-
cesses are involved: boring and honing at nearly $1,000 per section and chrome plating of the bore
at $1,000 per section. The plating is included to prevent potential problems with oxide on the inner
surface. Total estimated cost is $4,350 per baseline section each of which weighs slightly more than
1 ton.

An entry section was assumed to cost twice as much as a standard section since only a few will
be built and one entry section may include a tapered bore. Although no consideration was given to
the design details of the fiction section, it was assumed that each could be built at three times the
cost of a standard section.

All tube joints were assumed to contain either a spacer or a quick operating valve. The
spacer is designed to be interchangeable with a valve, giving complete freedom of valve setup loca-
tions. Valves are assumed to be scaled up versions of the type that have been developed at AEDC.
Pipe stand type tube supports set in concrete are assumed at two locations per tube section. The use
of two locations permits the removal of single tube section without loss of support for remaining
sections.

A single stage mechanical vacuum pump capable of pumping the entire recovery tube down to a
pressure of 0.1 torr in 1 hour has been included. The gas charging system consists of sufficient
helium to conduct two tests plus the associated plumbing for filling the compartments and valve
cylinders.

The control system is assumed to consist of a simple minicomputer plus the transducers asso-
ciated with each valve station. An asphalt runway 15 feet wide and running the entire length of the
recovery tube has been included so that a fork lift can be used in handling tube sections.

The resultant elemental cost breakdown for the baseline case is given in Table 6-3. Both the
entry section and friction section are assumed to consist of two sections (30 feet long) with 100
percent spares. Spare deceleration tube sections, valves, and spacers are included at 10 percent.
Final figures for the baseline case are approximately $478,000 for materials and $350,000 for labor,
making a total estimated cost of $828,000. This cost does not represent a firm estimate but is more
of a baseline from which variations can be considered as described in the next section.

6.2 PARAMETRIC COST EVALUATION RESULTS

The cost evaluation technique described for the baseline case above is applied, with appropri-
ate scaling factors, to a matrix of system parameters. As shown in Table 6-4, three cases each were

TABLE 6-3. BASELINE CASE RESULTS

Item	Cost
MATERIAL	
*Tube entry section, 4 each @ $8700	$ 34800
*Tube deceleration section — standard (700 atm), 52 each @ $4350	226200
high pressure (1200 atm), 7 each @ $7780	54460
*Tube friction section, 4 each @ $13050	52200
*Spacers, 54 each @ $150	8100
*Valves, 6 each @ $3000	18000
Tube supports, 114 each @ $400	45600
Vacuum system, 1 each @ $2000	2000
Gas charging system, 1 each @ $3000	3000
Control system, 1 each @ $15000	15000
Muffler and barricade, 1 each @ $500	500
Asphalt runway, 1 each @ $18000	18000
Total Materials	$477860
*Includes spares	
LABOR	
Detailed design	$160000
Site preparation	40000
System installation	100000
Checkout and debug	50000
Total Labor	$350000
TOTAL COST	$827860

TABLE 6-4.   COST EVALUATION MATRIX

Case Number	Number of Compartments	Nominal Deceleration Rate (10^3g's)	Tube Inside Diameter (inches)	Comments
1 (Baseline)	5	8	8	Effect of number of compartments
2	10	8	8	
3	3	8	8	
4	5	4	8	Effect of deceleration rate
5	5	2	8	
6	5	8	4	Effect of tube diameter
7	5	8	14	

Note: Helium charge gas in all cases

examined to study the effect of varying the number of compartments, the deceleration rate, and the tube inside diameter. The charge gas was assumed to be helium in the seven different cases examined.

The scaling factors applied in estimating the cost for each parametric case are as follows:

- Pressure: from shock/dynamics analysis ($\sim D a_R$)

- Length: from shock/dynamics analysis ($\sim 1/a_R$)

- Tube raw material cost $\sim$ tube weight

- Flanges, spacers $\sim D^2$

- Tube labor constant

- Shipping $\sim$ tube weight

- Tube supports, asphalt runway, site preparation, system installation $\sim$ length

- Vacuum system capacity adjusted to maintain constant pump-down time

- Gas charging system maintained at a 2-shot quantity

- Control system $10,000 + $1,000 x number valve stations

- Spares @ 100 percent on entry and friction sections, 10 percent on deceleration sections, spacers, valves.

The shock/dynamics analysis results are used to determine the appropriate tube design pressures. In general, the peak tube pressure considerably exceeds the pressure exerted on the projectile due both to the basic nature of the recovery tube concept and to shock interactions occurring ahead of the projectile. The calculated pressure envelope as a function of distance is shown in Figure 6-3 for an example case. Shock interactions are most pronounced in the vicinity of the valve at the entrance to the last compartment. A tube design envelope with a maximum of two pressure levels was determined for each case.

When this pressure enveloping process was applied to the first three cases in Table 6-4, the results shown in Figure 6-4 were obtained. The three compartment tube with helium does not exhibit severe shock interaction even at the third valve location. The five,and ten compartment cases do, however, exhibit severe pressures near the valve leading into the last compartment. Extremely high pressures such as the 2200 atm portion of Case 2 exceed the capability of the 90 ksi alloy steel. Special treatment was assumed for these tube sections (e.g., heat treatment to 140 ksi, or auto-frettage) and extra cost was added to cover such treatment, as discussed previously in Subsection 4.1.2.
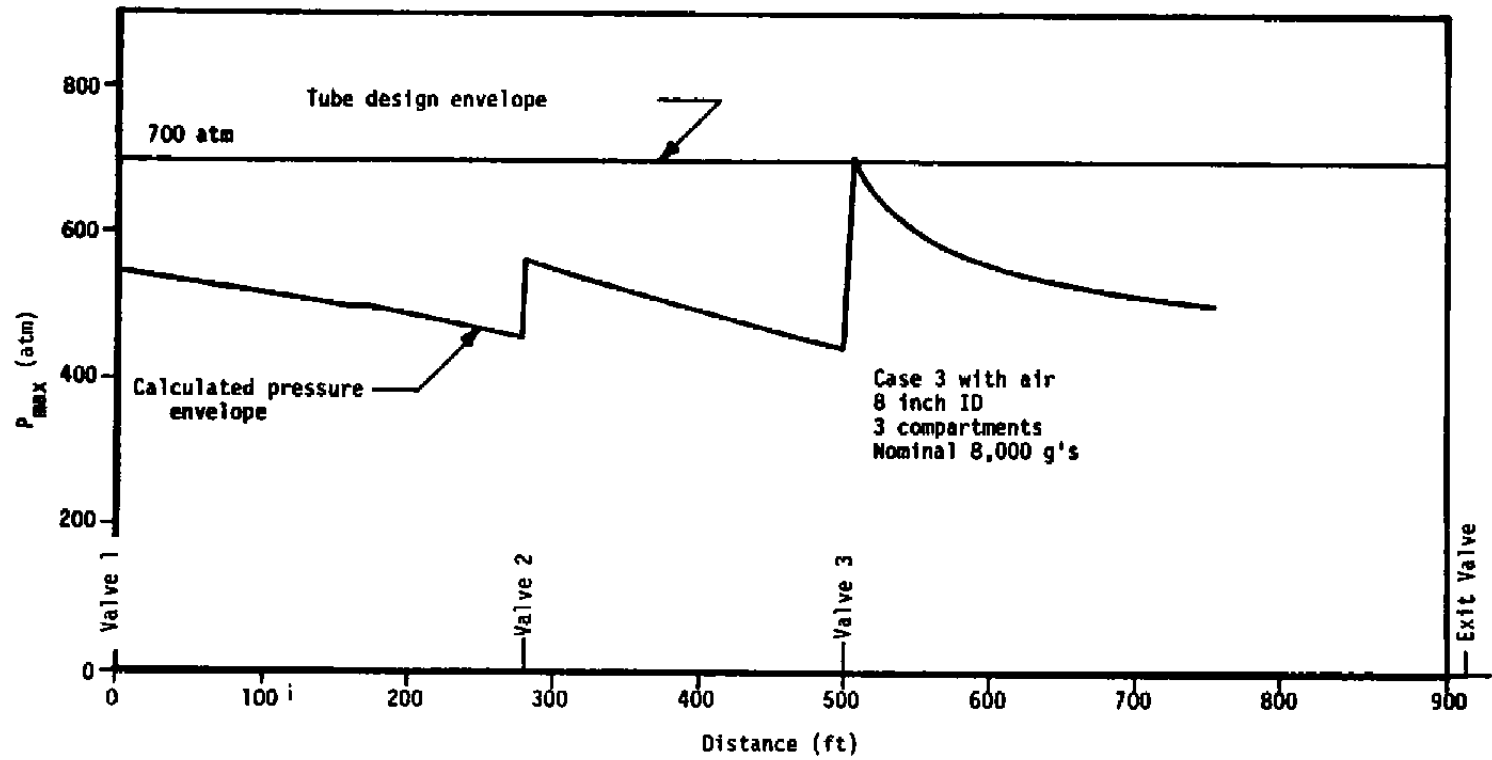
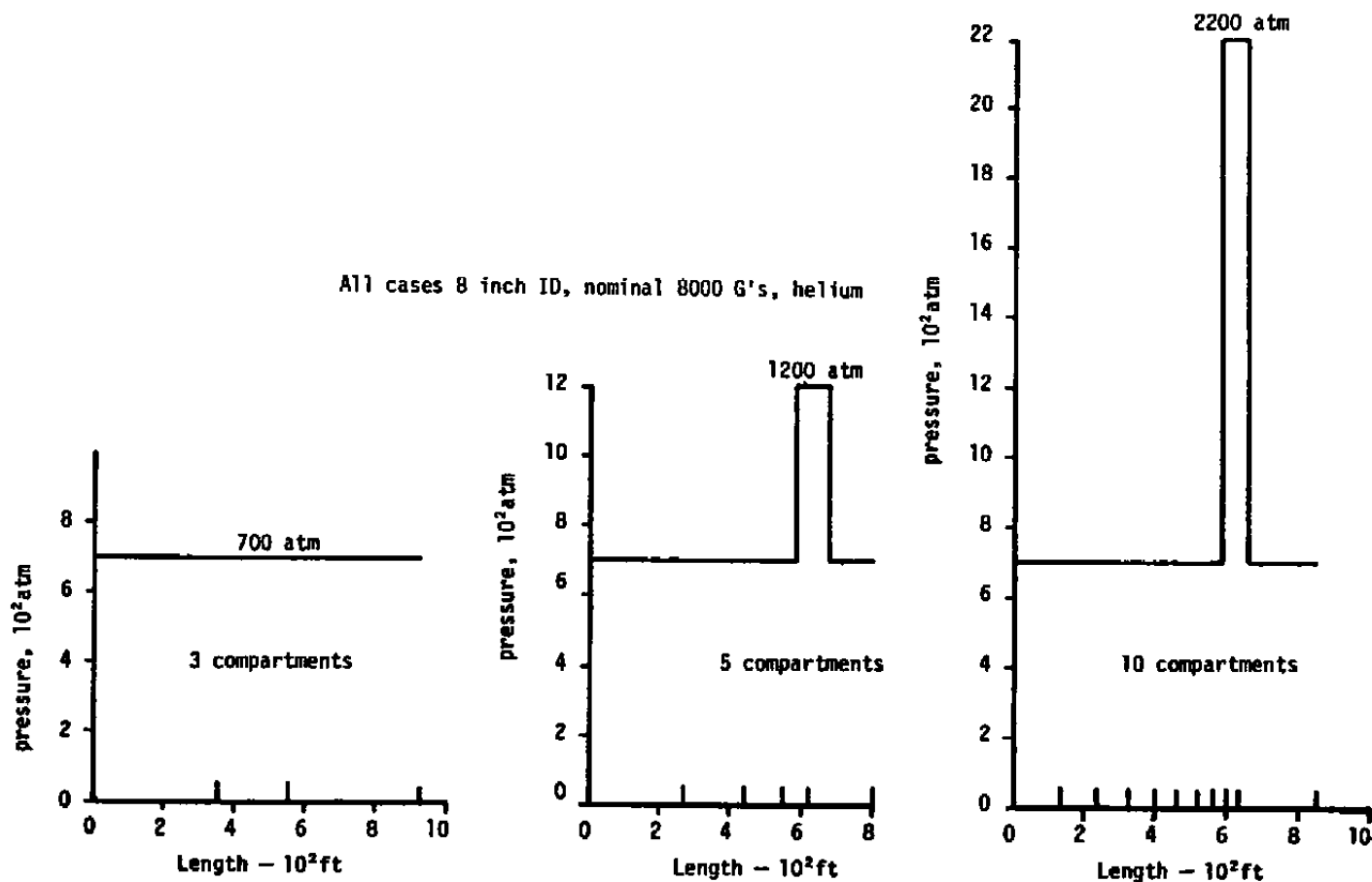Figure 6-3. Tube design pressure envelope (example).

Figure 6-4. Effect of number of compartments on pressure envelope.

The curve shown in Figure 6-5 shows the effect of the number of compartments on system cost. Cost is nearly constant for 3, 5, and 10 compartment cases with all other factors remaining equal. It is concluded that three compartments are adequate, while considerably reducing both the operating pressure and complexity.

Nominal deceleration rates of 2000, 4000, and 8000 g's were considered in the parametric study. The calculated deceleration rates differ somewhat from these nominal values for the particular valve locations and compartment pressures assumed. Figure 6-6 exhibits the strong dependence of system cost on deceleration rate. Calculated rather than nominal rates have been plotted. The strong function of cost on deceleration rate is primarily a result of the dependence of system length on deceleration rate, which is also plotted on Figure 6-6. The lowest deceleration rate examined, for example, requires a tube nearly a mile long. Although cost is still decreasing at the nominal 8000g deceleration level, this level is clearly beyond the knee of the cost vs. deceleration rate curve.

The effect of tube inside diameter variations on cost is shown in Figure 6-7. Costs were estimated for inside diameters of 4, 8, and 14 inches. The cost is fairly constant in the 4 to 8 inch range, but increases markedly at large diameters. Not only are the operating pressures greater for larger diameters ($P \sim Da_R$), but the stresses are also greater in a larger diameter tube. A diameter choice must include consideration of the ballistic coefficient that can be achieved at the various diameters. A plot of ballistic coefficient as determined in Section 2 is also shown in Figure 6-7. An 8-inch diameter is required for a ballistic coefficient of nominally 1000 lb/ft². Lower values are not sufficient to maintain flight simulation velocities in a large scale track-guided range.

A complete summary of the parametric cost study results is given in Table 6-5. Calculated deceleration rate, system length, model location when 1000 ft/sec is achieved, and total system cost are tabulated for each of the seven cases. Only Case 5 exhibited sufficiently low pressures to permit the economic use of carbon steel tubing (see Figure 6-2). The high pressure regions of both Cases 2 and 7 exceed the capability of the 90 ksi alloy steel, requiring special treatment to obtain greater strength.

6.3   OPTIMUM RECOVERY TUBE SYSTEM

A set of parameters for an optimum recovery tube system were selected from the results of the parametric cost evaluation above. These optimum system parameters are as follows:

- Nominal 8000 g deceleration

- Eight-inch bore

- Three compartments.
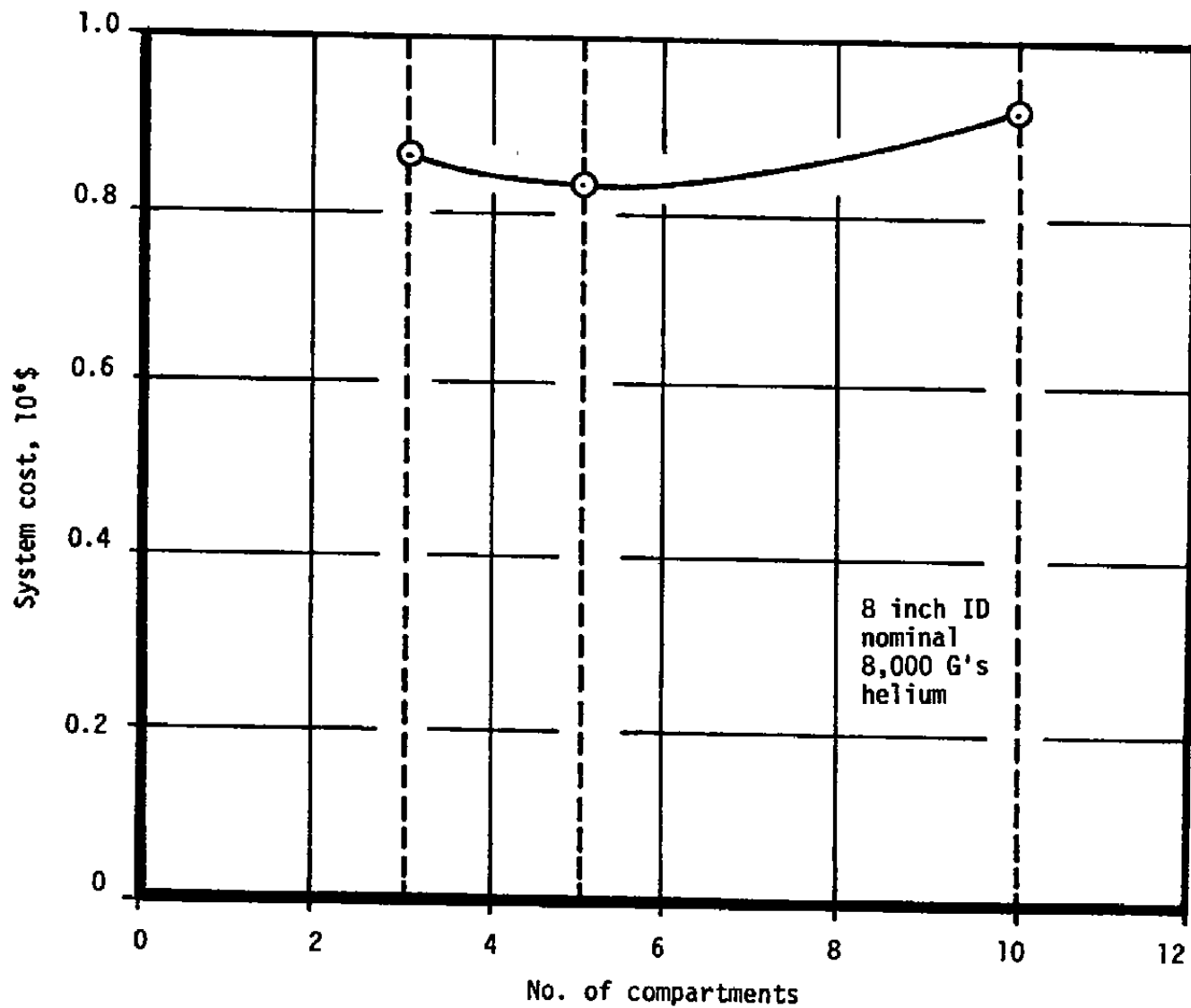
Figure 6-5.   Effect of number of compartments on system cost.
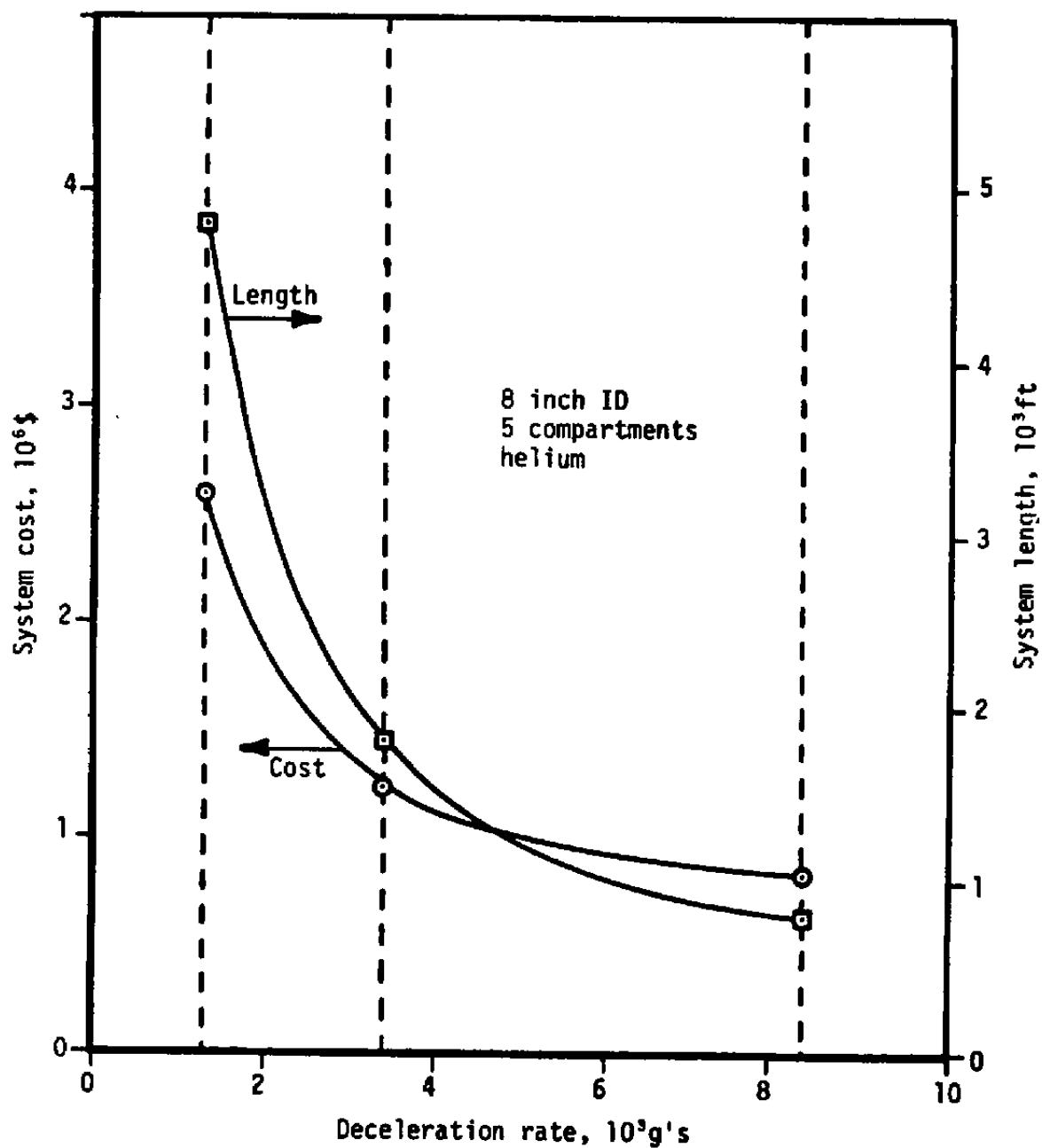
Figure 6-6. Effect of deceleration rate on system cost.
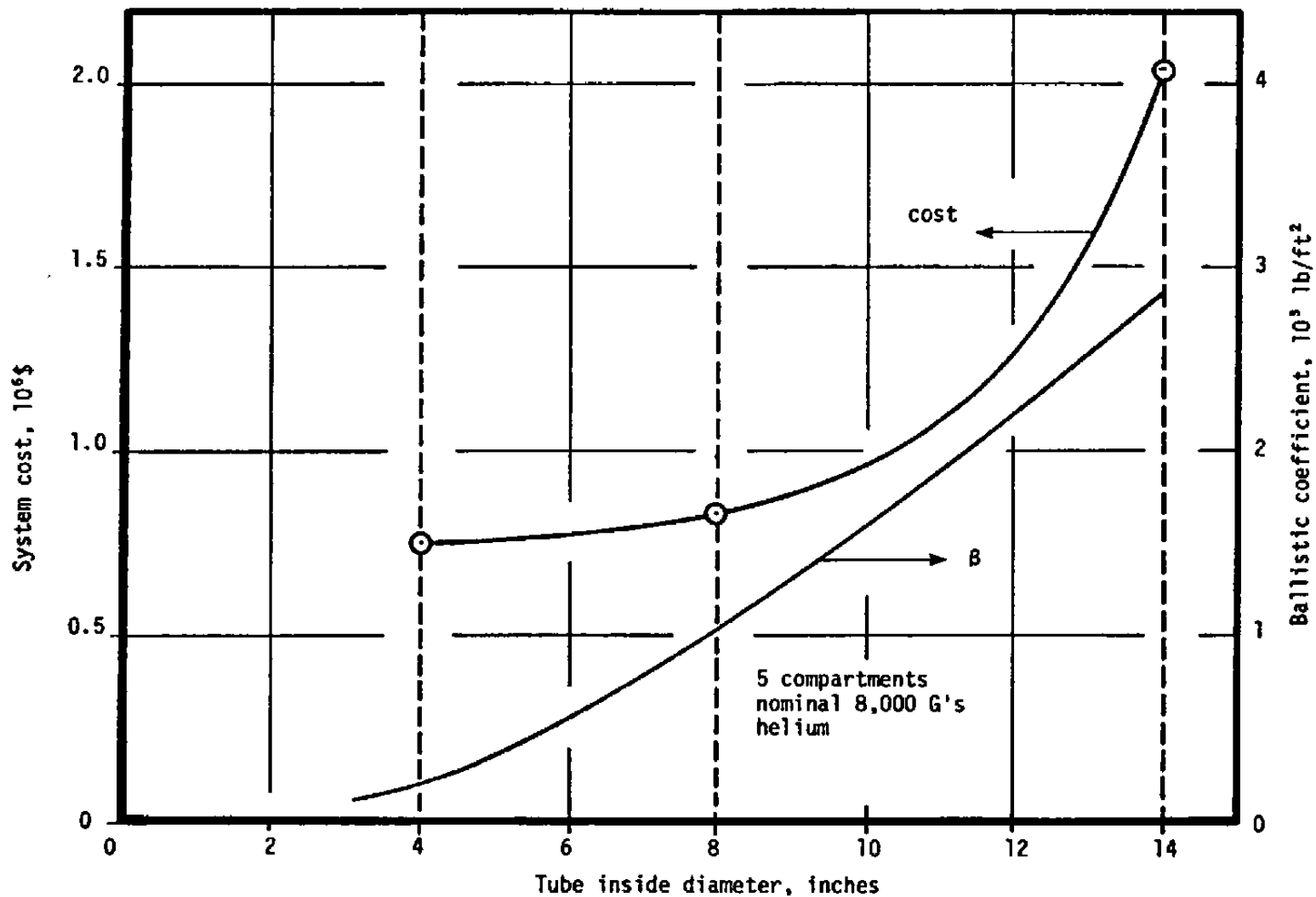
Figure 6-7. Effect of tube diameter on system cost.

TABLE 6-5. SUMMARY OF PARAMETRIC COST STUDY

Case Number	No. of Compartments	Calculated Average Deceleration Rate $(10^3 g's)$	Tube ID (inches)	Length[a] (ft)	Model Station @ 1000 fps[b] (ft)	Total Cost $(10^6 \$)$
1	5	8.30	8	800	600	0.83
2	10	7.19	8	850	650	0.92[c]
3	3	6.54	8	920	680	0.86
4	5	3.40	8	1800	1300	1.24
5	5	1.29	8	4800	3400	2.59[d]
6	5	6.91	4	1000	660	0.75
7	5	8.30 (est)[e]	14	~800 (est)[e]	~600 (est)[e]	2.04[c]

[a]Not including entry section (30 ft) and friction section (30 ft)

[b]Station 0 is at end of entry section

[c]Special treatment required for high pressure region (heat treatment, autofrettage, etc.)

[d]Carbon steel used in Case 5. Alloy steel used in all other cases

[e]No shock/dynamics calculations performed for Case 7

These parameters correspond to Case 3 of Table 6-5, which is a 920 foot long facility. The nominal 8000 g deceleration rate is near minimum cost. The 8-inch bore allows the testing of projectiles of reasonable ballistic coefficient and is near a minimum cost. The use of three compartments provides reduced operational pressures and reduced complexity while still realizing near minimum cost. For flexibility, the opitmum system should be designed for operation with a range of gases from helium to argon.

6.3.1 Effect of Operating Gas

Shock/dynamics calculations were performed for operation of the optimum facility with both air and argon in addition to the helium calculations discussed previously. Table 6-6 summarizes various parameters involved in operating the optimum system with helium, air, and argon. Both the valve setup locations and compartment pressures are quite different for the three gases. Maximum flexibility of operation would be realized if valves were installed at the locations needed for all charge gases of interest. All valves except those necessary for the specific gas being used in a particular test would be left open. For three gases and three compartments, such a setup requires a total of six valves: one at the entrance, two* at the front of compartments 2 and 3, and one at the exit.

There is little difference in the maximum tube pressure for the three gases. A peak value of approximately 700 atm is calculated near the entrance to the last compartment in each instance. Therefore, a tube designed for an operating pressure of 700 atm can safely accomodate all three gases. As shown in Table 6-6, the calculated deceleration rates for the valve locations and charge pressures assumed for the optimum system are in the 6000 g range rather than the 8000 g nominal value. The amount of gas required to achieve a given deceleration rate is markedly greater for a light gas such as helium. As seen from Table 6-6, 5200 ft^3 (STP) of helium costing about \$440 are required per shot while an argon shot would consume only 800 ft^3 (STP) for an estimated \$50 cost.

6.3.2 Effect of Projectile Velocity Variation

Unexpected variations may occur in the velocity of the projectile entering the recovery tube in an operating track-guided range. A lower than expected velocity might jeapardize test objectives, but should not create a hazardous situation. A greater than expected velocity, however, could result in higher than expected recovery tube pressures and a reduced tube factor of safety.

---

*Only two are required since argon and helium have the same compartment locations.

TABLE 6-6. EFFECT OF OPERATING GAS

	Helium	Air	Argon
Valve 1 location (feet)	0	0	0
Valve 2 location (feet)	345	285	345
Valve 3 location (feet)	540	495	540
Exit valve location (feet)	915	915	915
Model location @ 1000 fps (feet)	680	740	700
Compartment 1 pressure (atm)	8.1	1.32	0.85
Compartment 2 pressure (atm)	14.2	2.35	1.50
Compartment 3 pressure (atm)	24.8	4.10	2.60
Maximum tube pressure (atm)	700	715	728
Calculated average deceleration rate (10^3g's)	6.54	5.39	6.20
Gas consumption per shot (ft³ @ STP)	5200	1300	800
Gas cost per shot ($)	440	20 (N_2)	50

Experience at AEDC with existing facilities has shown that a reasonable upper variation of projectile velocity in the range of interest (18400 ft/sec) is plus 1000 ft/sec. Shock/dynamics calculations were performed for the optimum system charged with helium with a 19400 ft/sec projectile velocity rather than 18400 ft/sec. Peak pressures increased from the design level of 700 atm to approximately 800 atm. Figure 6-8 shows that the tube factor of safety is reduced from the design value of 2.0 to a value of 1.75. Thus, the tube is still quite safe even at an anticipated upper limit of projectile velocity.

6.3.3 Preliminary Design of Optimum System

Preparatory to making a refined cost estimate for the optimum system, a short preliminary design effort was conducted. Figure 6-9 shows an overall view of the optimum recovery tube system. All critical stations such as valve locations have been rounded off to the nearest multiple of the basic 15 foot pipe section. Both the entry section and friction section consist of two 15 foot sections, or 30 feet each. Total system length with the entry and friction sections is 975 feet. A 15 foot wide asphalt runway extends for the entire length of the tube to facilitate operation with a fork lift. Although the system depicted in Figure 6-9 is shown set up for helium, it is recommended that valves be included in appropriate locations for all gases of interest.

A typical 15 foot tube section with a composite of all piping and wiring entries that occur on the various tube sections is shown in Figure 6-10. The tube centerline is located 4 feet above the asphalt surface, making a conventient working height. Two tube supports are utilized per section so that single sections can be removed without loss of support for adjacent sections.

The tube supports also support the piping for the vacuum system, the high pressure charge gas system, and shop air for service. A conduit carrying instrumentation and control wiring plus service power is also attached to the tube supports. The composite section in Figure 6-10 shows typical entries for purge of air, backfill with charge gas, a pressure transducer, and charge gas and wiring for a typical quick operating valve.

Details of a proposed tube joint design are shown in Figure 6-11. Either a valve or a spacer can be accomodated at any joint. The concept shown has been specifically configured to provide sufficient gap after unbolting to allow easy removal of the valve or spacer. Three standard pipe flanges are used at each joint of the concept: two slip-on type flanges welded to the outside diameter of the tubing and one blank flange machined so that it will slide along the tube OD after removal of a split ring. After removal of the spacer or valve at each end of a tube section, sufficient clearance is available for easy removal of a tube section with a fork lift.
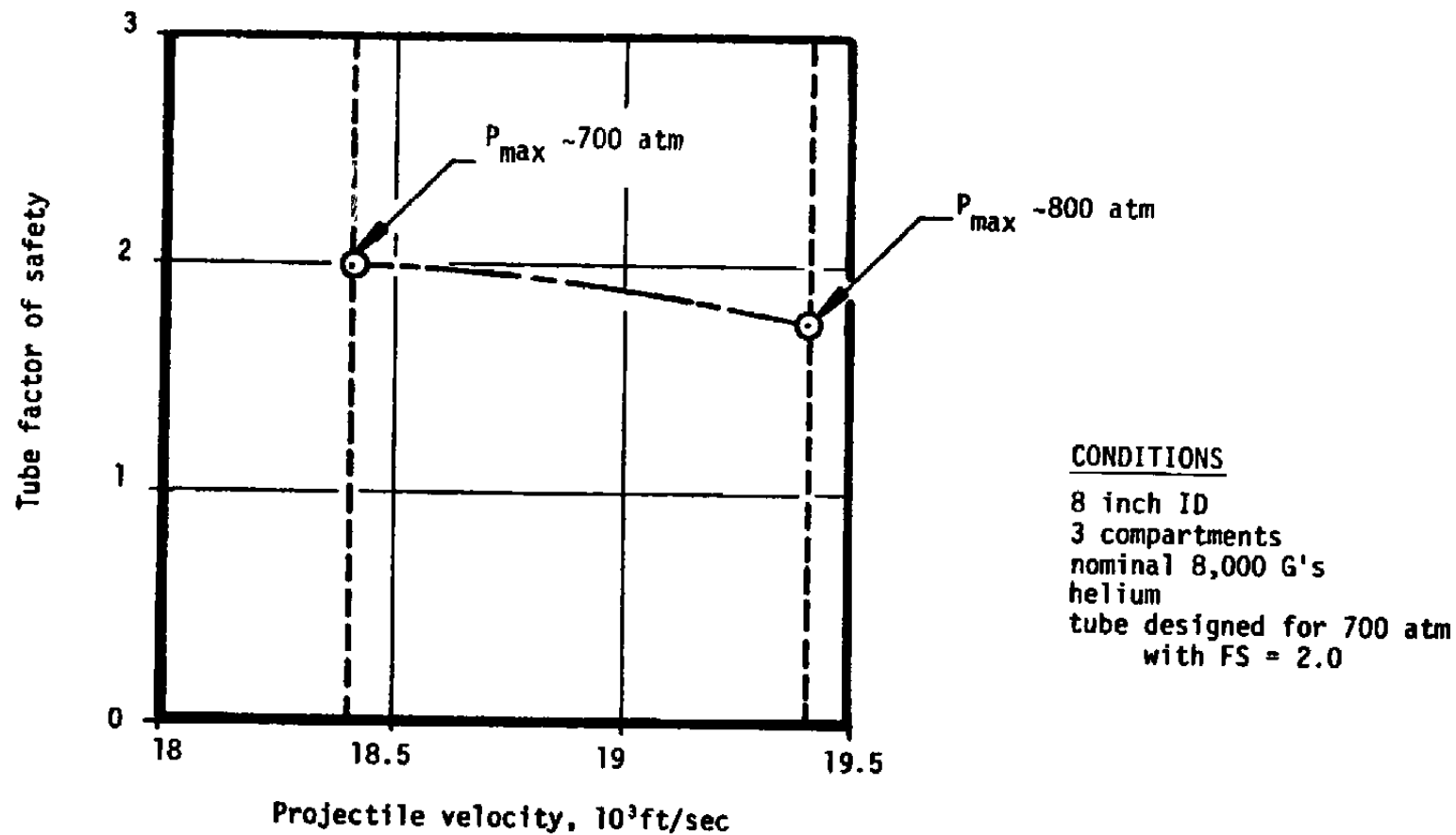
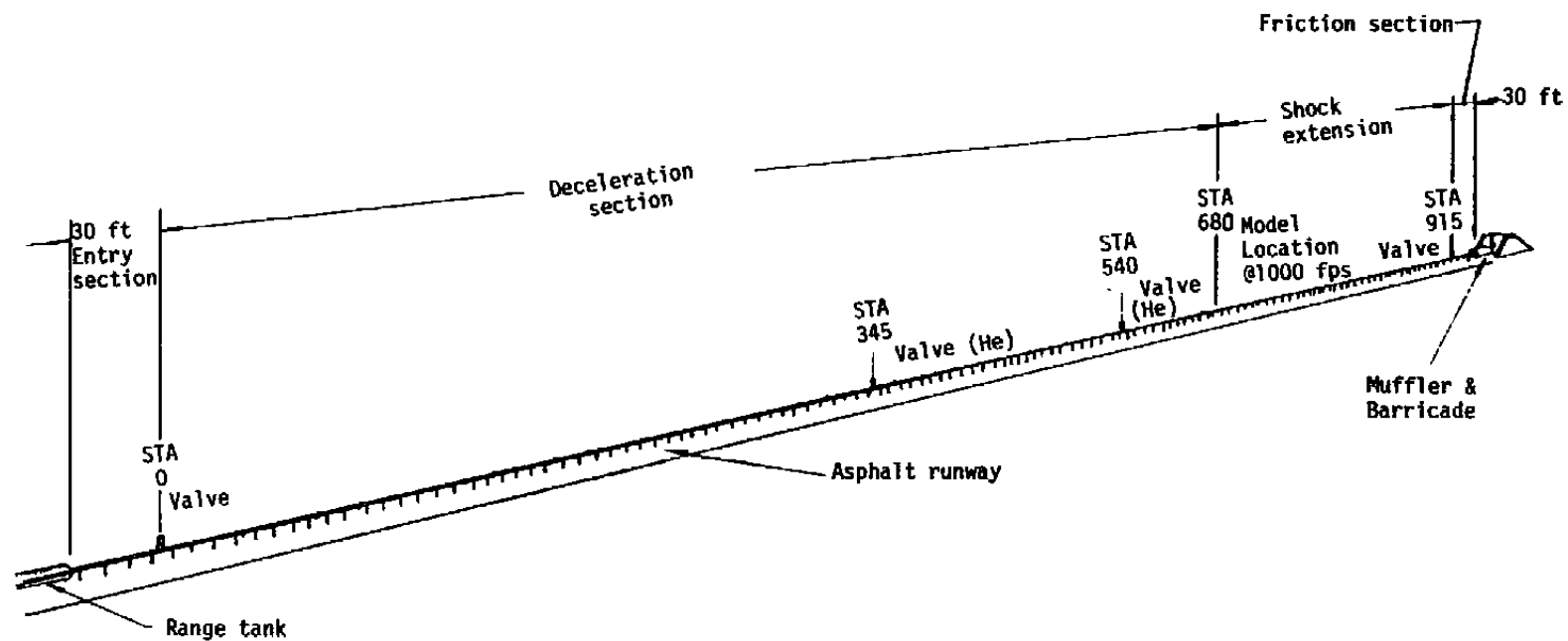Figure 6-8. Effect of projectile velocity variation.
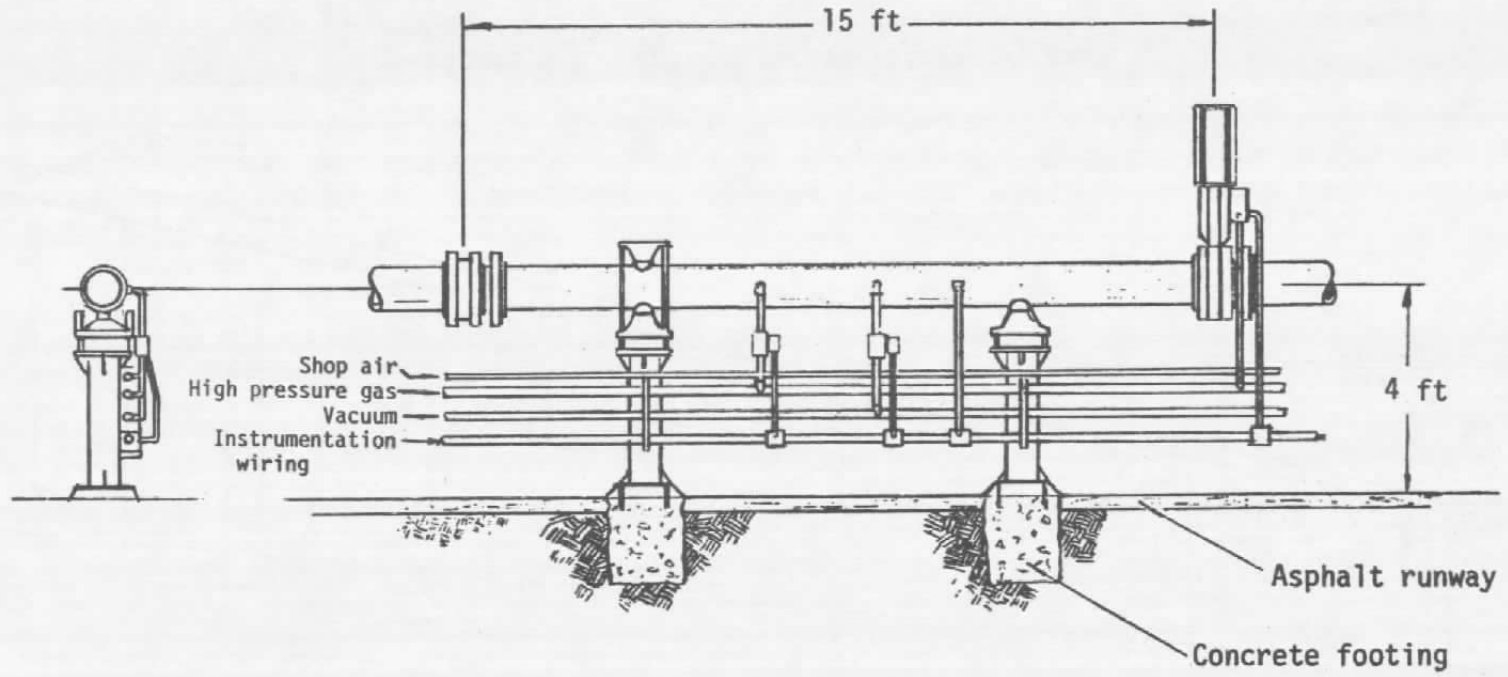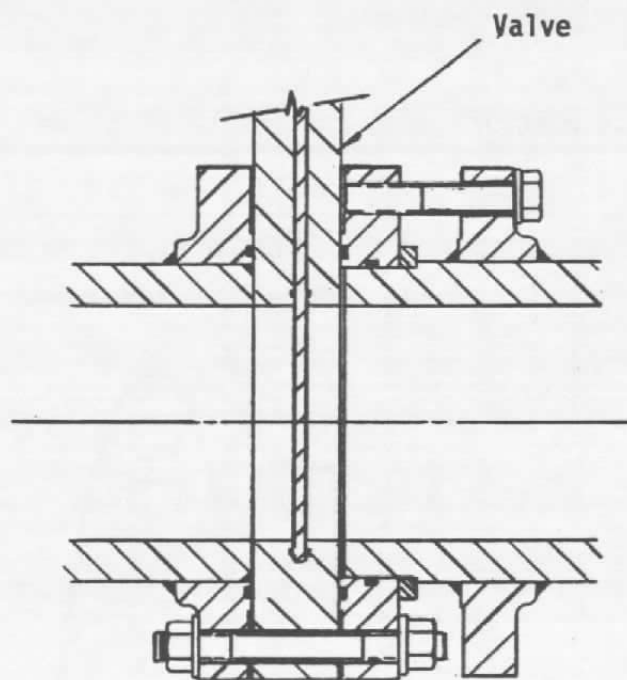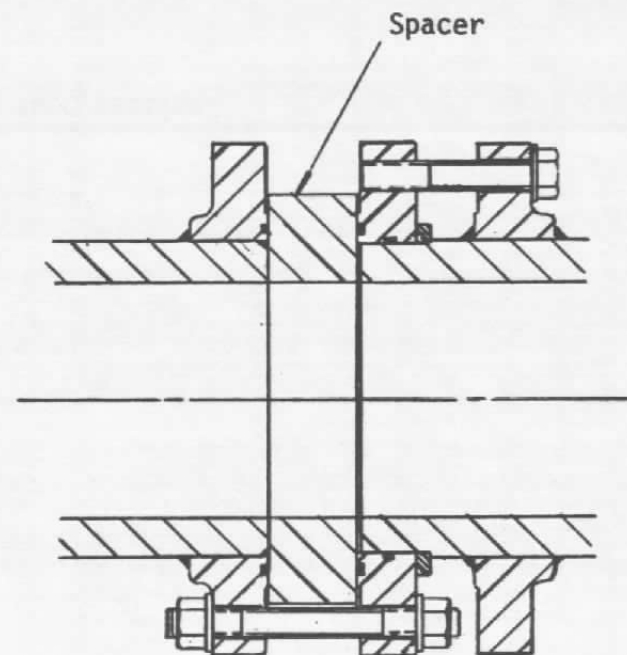
Figure 6-9. Optimum recovery tube system.

Figure 6-10. Composite tube section.

Figure 6-11. Tube joint details.

Figure 6-12 shows a proposed tube support concept. Standard pipe roll stands have been used to provide free axial motion for thermal expansion and contraction. It is assumed that every other tube support will also have a pipe roller installed above the tube to provide vertical constraint. The entire support is of welded and bolted construction and each is set in a concrete base.

A schematic of the purge and backfill system is shown in Figure 6-13. A single stage mechanical vacuum pump of 80 cfm capacity is required to purge the optimum system to 0.1 torr in 1 hour. Three vacuum ports are shown in the tube, one near the midpoint of each of the three compartments. The gas charge system also has a port near the middle of each compartment plus piping to charge each valve actuation cylinder with high pressure gas. All of these pipe entries require valving. A single shot with helium requires approximately 5200 ft^3 (at STP).

6.3.4 Refined Cost Estimate for Optimum System

Although the optimum system parameters are the same as Case 3 of the parametric study in Table 6-5, a refined cost estimate was made to reflect the preliminary design efforts above plus the extra valving to accomodate operation with helium, air, or argon. This estimate is summarized in Tables 6-7 and 6-8. Vendor estimates were obtained for the specific sizes and quantities appropriate for the optimum design. A standard 700 atm tube section is estimated to cost $4,450. This figure includes the use of three flanges per joint as shown in Figure 6-11. The tube support design depicted in Figure 6-12 is estimated to cost $330.

The facility total cost estimate includes the cost of ten valves, six in position to provide the flexibility of three operating gases, two for additional flexibility, and two spares. The costs of O-rings and miscellaneous hardware are also included. Both the vacuum system and the gas charging system include a cost estimate for plumbing as shown in Figures 6-10 and 6-13. The control system cost estimate has been increased to reflect the added valve locations and to account for the instrumentation and control wiring indicated in Figure 6-10.

The total estimated cost for the optimum recovery tube system, including both material and labor estimates, is $915,440. This compares to a figure of $860,000 estimated previously for Case 3 of the parametric study.

Upper constraint
as required
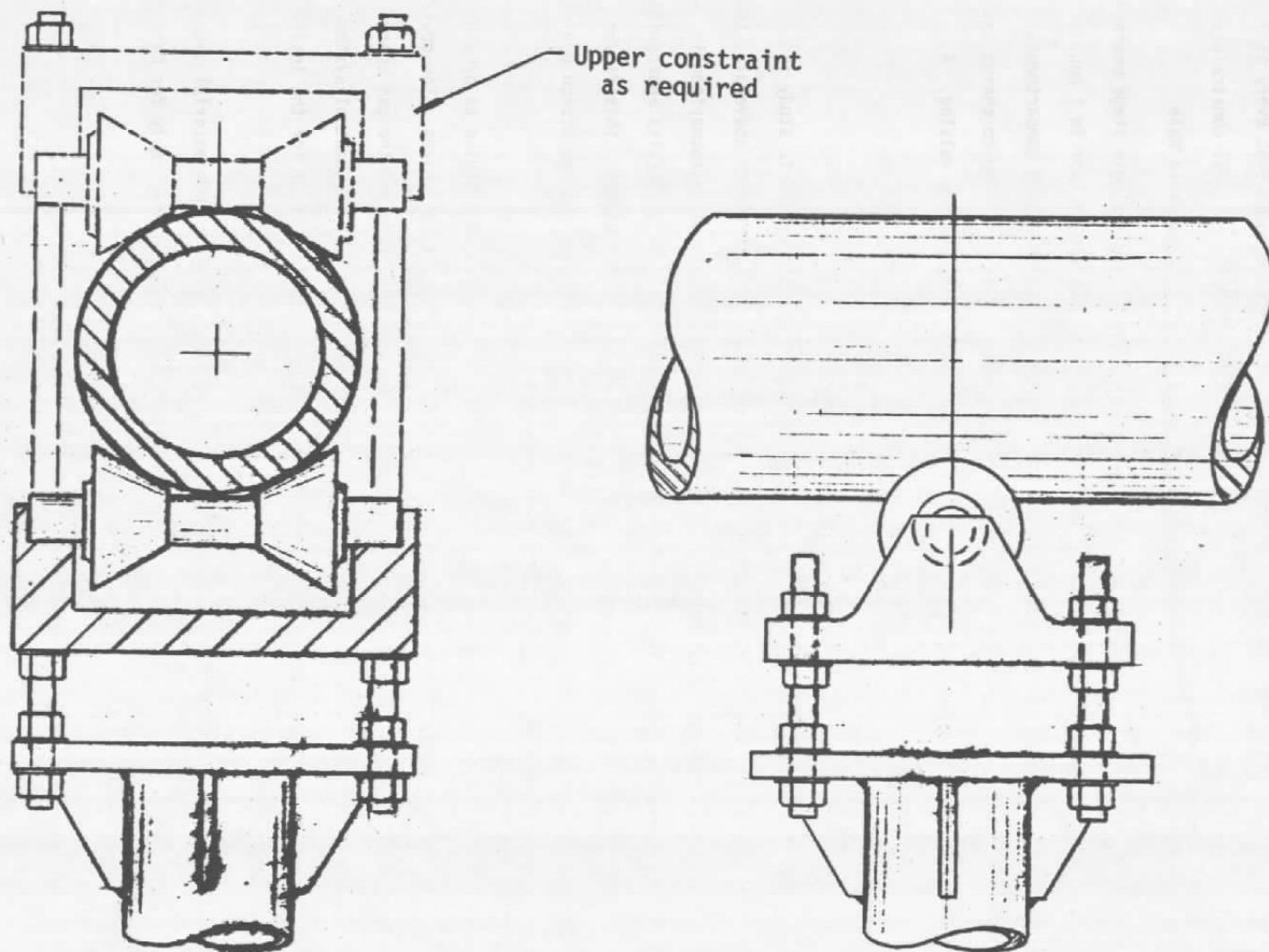
Figure 6-12. Typical tube support.
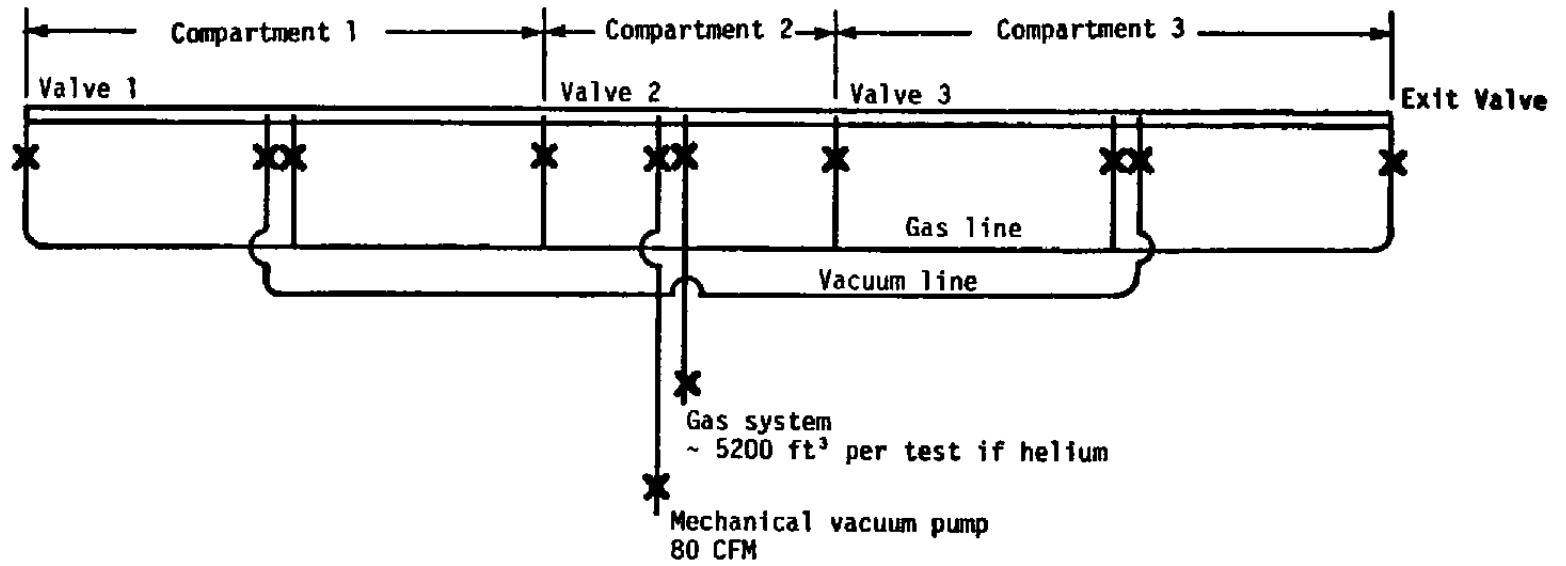
Figure 6-13. Schematic of purge and backfill system.

TABLE 6-7. TUBE SECTION AND TUBE SUPPORT COST ESTIMATE

STANDARD 15 FOOT TUBE SECTION (700 atm.)

Seamless tubing	15 ft @ $105/ft		$ 1,580
Slip-on flanges	2 @ 120/ea		240
Machining of 1 slip-on flange			10
Blank flange	1 @ 145/ea		145
Machining of blank flange			80
Split ring	1 @ 25/ea		25
Weld flanges, face tube ends, bore, and hone			1,100
Chrome plate			1,000
Inspect			100
Shipping			170
		Total	$ 4,450

TUBE SUPPORT

Pipe roll stand	$ 24
Pipe	18
Threaded rod and nuts	38
Fabrication	150
Drill holes and set in concrete	100
	$ 330

TABLE 6-8. COST ESTIMATE FOR OPTIMUM RECOVERY TUBE SYSTEM

MATERIAL

Tube entry section, 2 + 2 spares @ 2 x $4,450	$ 35,600
Tube deceleration section — standard (700 atm), 61 + 7 spares @ $4,450	302,600
Tube friction section, 2 + 2 spares @ 3 x $4,450	53,400
Spacers, 54 + 6 spares @ $150	9,000
Valves, 8 + 2 spares @ $3,000	30,000
O-rings, 189 + 30 spares @ $3	660
Misc. hardware — bolts, studs, nuts, washers; 2,464 ea @ $6	14,780
Tube supports, 130 ea @ $330	42,900
Vacuum system (including plumbing)	4,000
Gas charging system (including plumbing)	8,000
Control system (including wiring network)	21,000
Muffler and barricade, 1 ea @ $500	500
Asphalt runway, 1 ea @ $22,000	22,000
Total Materials	$544,440

LABOR

Detailed design	$160,000
Site preparation	46,000
System installation	115,000
Checkout and debug	50,000
Total Labor	$371,000
Total Estimated Cost	$915,440

.

SECTION 7

CONCLUSIONS

A recovery tube for recovering reentry vehicle models tested in a large scale guided track range was studied analytically. The major conclusions from this study are associated with the model damage during recovery, optimal recovery tube design parameters, and recovery tube system cost.

7.1   MODEL DAMAGE

Sophisticated analytical techniques were employed to predict the test model response during range flight, recovery, and cooldown. These calculations indicated that no significant model damage will occur during recovery and cooldown. Specifically:

- Maximum graphite nosetip model surface ablation for recovery in helium is less than 0.002 inches

- Structural loads during recovery are less than 30 percent of allowables (thermal structural problems during post-recovery "cooldown" can be designed around)

- In-depth temperatures quickly drop below graphitic material processing temperatures.

7.2   OPTIMUM RECOVERY TUBE DESIGN

Based on consideraitons of projected model size and ballistic coefficient objectives, model damage, and recovery tube system cost scalings, the design parameters for an optimum cost effective recovery tube are:

- Length   ≈ 1000 ft.

- Bore   = 8 inches

- Number of pressure compartments = 3

- Maximum design pressure   ≈ 700 atm

7.3   COST

Based on current (April, 1976) dollars, the estimated cost to fabricate and install the above "optimum" recovery tube system is $900,000.

REFERENCES

1. Teng, R. N. and Hickman, R. S., "Demonstration of a Technique for Guiding and Retrieving Hyper-velocity Projectiles in a Ballistic Range," McDonnel Douglas Astronautics Co., AEDC-TR-73-190, November 1973.

2. Teng, R. N., et al., "Demonstration of a Scaled-up Hypervelocity Projectile Guiding and Retrieving System," McDonnell Douglas Astronautics Co., AEDC-TR-74-123, June 1975.

3. Derbidge, T. C., and Powars, C. A., "Repeated Launch Guided Track Nosetip Shape Change Analysis," Aerotherm Report TR-74-131, December 1974.

4. Norfleet, G. D., et al., "Development of an Aeroballistic Range Capability for Testing Re-entry Materials," AIAA Paper No. 74-609, 1974.

5. Roark, R. J. "Formulas for Stress and Strain": McGraw-Hill Book Company, 1955.

6. Cohen, L. M., Short, J. N., and Oppenheim, A. K., "A Computational Technique for the Evaluation of Dynamic Effects of Exothermic Reactions," Combustion and Flame 24, 319-334, 1975.

7. Dahm, T. J., and Anderson, L. W., "Propellant Gas Convective Heat Transfer in Gun Barrels," Aerotherm Final Report No. 70-18, August 1970.

8. Mirels, H., "Boundary Layer Behind Shock or Thin Expansion Wave Moving Into Stationsry Fluid," NACA TN-3712, 1956.

9. MacCormack, R. W., and Baldwin, B. S., "A Numerical Method for Solving the Navier-Stokes Equations with application to Shock Boundary Layer Interactions," AIAA Paper 75-1, AIAA 13th Aerospace Sciences Meeting, Pasadena, California, January 1975.

10. Personal Communications with R. W. MacCormack, NASA Ames, July-December 1975.

11. Abbett, M. J., "Finite Difference Solution of the Subsonic/Supersonic Inviscid Flow Field About a Supersonic, Axisymetric Blunt Body at Zero Incidence," Analysis and User's Manual, Aerotherm UM-71-34, June 1971.

12. Moretti, G. and Abbett, M. J., "A Time Dependent Computational Method for Blunt Body Flows," AIAA Journal, Vol. 4, No. 12, 1966, pp. 2136-2144.

13. Edelman, R. B., et al., Same Aspects of Viscous Chemically Reacting Moderate Altitude Rocket Exhaust Plumes, Final Report, Contract NAS8-21264, General Applied Science Laboratories, Inc., Westbury, N.Y., March 1970.

14. McCuen, P.A., Schaefer, J. W., Lundberg, R. E., and Kendall, R. M., "A Study of Solid Propellant Rocket Nozzle Exposed Materials Behavior," Report No. AFRPL-TR-65-33, Vidya Report No. 149, February 1965.

15. Evans, R. M., "User's Manual, Boundary Layer Integral Matrix Procedure Including Gas Phase Kinetics," Aerotherm UM-75-62, March 1975.

16. Nicolet, W. E., Advanced Methods for Calculating Radiation Transport in Ablation Product Con-taminated Boundary Layers, NASA CR-1656, Aerotherm Corporation, Mountain View, California, September 1970.

17. Nicolet, W. E., User's Manual for the 1973 Version of the Radiation Transfer Code (RAD/EQUIL/1973), Acurex Report No. UM-73-10, Acurex Corporation, Mountain View, California 1973.

18. Rafinejad, D. and Derbidge, T., "Computer User's Manual: Aerotherm Nosetip Analysis Procedure (ANAP)," Aerotherm Report UM-74-58, October 1970.

19. Powars, C. A., and Kendall, R. M., Aerotherm Chemical Equilibrium (ACE) Computer Program, User's Manual," Aerotherm UM 69-7, May 1969.

20. Weiler, F. C., "DOASIS, Vol. III User Manuals," Weiler Research Inc., AFML-TR-75-37, July 1975.

21. Shapiro, A. H., "The Dynamics and Thermodynamics of Comoressible Fluid Flow," Vol. II, the Ronald Press Company, New York, 1954.

22. Tsai, S. W. and Wu, E. M., "A General Theory of Strength for Anisotropic Materials," J. Composite Materials, Vol. 5, January 1971.

23. Priddy, T. G., "A Fracture Theory for Brittle Anisotripic Materials," Sandia Laboratories, SC-DR-710764, November 1971.

24. Green, S. J. and Scheirloh, F. L., "Uniaxial Stress Behavior of S-200 Beryllium, Isotropic Pyrolytic Boron Nitride, and ATJ-S Graphite at Strain Rates to 10^3/sec. and 700°F," General Motors, MSL 68-11, March 1968.

25. Telephone Communications from M. D. Jackson to H. S. Starrett, March 1976.

26. "Research and Development of Materiel, Engineering Design Handbook, Gun Series, Gun Tubes," Headquarters, U.S. Army Materiel Command, AMCP 706-252, February 1964.

27. "Metals Handbook, Volume 1, Properties and Selection of Metals," American Society for Metals, 1961.

28. Galloway, T. R., and Sage, B. H., "Thermal and Material Transfer from Spheres — Prediction of Local Transport," Int. J. of Heat and Mass Transfer, Vol. II, pp 539-549, Pergamon Press 1968

29. Starrett, H. S. and Pears, C. D., "Probable and Average Properties of ATJ-S (WS) Graphite," Southern Research Institute, Technical Report No. AFML-TR-73-14, Vol. I, November 1972.

30. Liepmann, H. W. and Roshko, A, "Elements of Gasdynamics," John Wiley & Sons, Inc., 1957.

31. "Reentry Mat Handbook, Rev. 1," Aerospace Corporation, TOR-1001 (S2855-20)-3-Rev. 1, CFRD, June 1969.

LIST OF SYMBOLS

a_L launch acceleration

a_R recovery deceleration rate

A or A_b projectile cross sectional area, or constant in Equations 4-25 or 4-38

B   constant in Equation 4-38

C   constant in Equations 2-3 and 4-38

C_D drag coefficient

$\dfrac{C_f}{2}$ friction factor, see Reference 7

C_H Stanton number

C_L, C_0 artificial viscosity parameters in Equation 4-5

C_p specific heat

D, d   projectile diameter (equal to recovery tube inside diameter)

D   diameter, or constant in Equation 4-38

e   specific internal energy

F   force

Fs   Frössling number, Equation 4-39

FS   factor of safety

G   boundary layer shape factor, see Reference 7

h   enthalpy

H   heat transfer coefficient

$K_1(m)$ coefficient in Equation 4-28

$K_2(m)$ coefficient in Equation 4-29

K_3 coefficient in Equation 4-30

LIST OF SYMBOLS (Continued)

L	length of launcher
m	model mass; also integer in Equation 4-19; also exponent in Equation 4-28
M_p or m	projectile mass
n	number of compartments
p	pressure
P	$p + \pi$
P_L	launch pressure
Pr	Prandtl number
P_R	recovery tube pressure
r	location of model along x; or radial coordinate
R	tube radius
Re	Reynold's number
R_N	nose radius
S_s	maximum shear stress/factor of safety
t	time
T	temperature
u	longitudinal velocity
u_e	boundary layer edge velocity
v	specific volume
V_E	recovery tube entry velocity
V_L	launch velocity

<center>LIST OF SYMBOLS (Continued)</center>

W	ratio of outside diameter to inside diameter
W_s	shock speed
x	distance along the tube; or along model surface
x_{sf}	shock location at the time of model terminal velocity
Y	tensile yield stress
α	angle around sphere
α_t	apparent freestream turbulence level
β	ballistic coefficient
γ	ratio of specific heats
γ_{rz}	shear strain in r-z plane
δ	boundary layer thickness
ε_z	axial strain
θ	momentum thickness
θ_c	cone half-angle
μ	viscosity
ν	kinematic viscosity
π	artificial viscosity parameter
ρ	density
ρ_e	boundary layer edge density
σ_r	radial stress
σ_θ	hoop stress
σ_z	axial stress

LIST OF SYMBOLS (Concluded)

τ_{rz} shear stress in r-z plane

ϕ enthalpy thickness

Subscripts

e   boundary layer edge

i   initial; interface

o   at the time of flow establishment

m   model

p   projectile

R, r   recovery

s   at separation, or at the shock

t   tube

w   wall

1   ahead of shock

2   behind shock

∞ freestream

Superscripts

—   mass element properties; or average value

´   reference property; or turbulent property